④

AD-A208 598

THIRD QUARTERLY REPORT

FOR THE PROJECT

"COMPOSITE CERAMIC SUPERCONDUCTING
WIRES FOR ELECTRIC MOTOR APPLICATIONS"

PRIME CONTRACTOR

CERAMICS PROCESS SYSTEMS CORPORATION
155 FORTUNE BOULEVARD
MILFORD, MASSACHUSETTS 01757

28 APRIL 1989

DTIC
S ELECTE
JUN 0 1 1989
D

CERAMICS
PROCESS SYSTEMS

89 5 30 119

THIRD QUARTERLY REPORT

FOR THE PROJECT

"COMPOSITE CERAMIC SUPERCONDUCTING
WIRES FOR ELECTRIC MOTOR APPLICATIONS"

PRIME CONTRACTOR

CERAMICS PROCESS SYSTEMS CORPORATION
155 FORTUNE BOULEVARD
MILFORD, MASSACHUSETTS 01757

28 APRIL 1989

CPS 89-007

DARPA ORDER NO: 9525
CONTRACT NO: N00014-88-C-0512
CONTRACT EFFECTIVE DATE: 30 JUNE 1988
CONTRACT EXPIRATION DATE: 31 MARCH 1991
PRINCIPAL INVESTIGATOR: JOHN W. HALLORAN
                              (508) 634-3422

Prepared for
DEFENSE ADVANCED RESEARCH PROJECTS AGENCY
1400 Wilson Boulevard
Arlington, VA   22209

OFFICE OF NAVAL RESEARCH
800 North Quincy Street
Arlington, VA   22217-5000

APPROVED FOR PUBLIC RELEASE: DISTRIBUTION IS UNLIMITED

DTIC
ELECTE
JUN 0 1 1989
S D
D

Accesion For		
NTIS CRA&I		☑
DTIC TAB		☐
Unannounced		☐
Justification		
By		
Dist ibution /		
Availability Codes		
Dist	Avail and/or Special	
A-1		

REPORT DOCUMENTATION PAGE

1. AGENCY USE ONLY (Leave blank)	2. REPORT DATE	3. REPORT TYPE AND DATES COVERED
	April 28, 1989	Technical Report 1/1/89 - 3/31/89

4. TITLE AND SUBTITLE	5. FUNDING NUMBERS
Composite Ceramic Superconducting Wires for Electric Motor Applications	N00014-88-C-0512

6. AUTHOR(S)

J. W. Halloran

7. PERFORMING ORGANIZATION NAME(S) AND ADDRESS(ES)	8. PERFORMING ORGANIZATION REPORT NUMBER
Ceramics Process Systems Corporation
155 Fortune Boulevard
Milford, MA 01757	CPS 89-007

9. SPONSORING/MONITORING AGENCY NAME(S) AND ADDRESS(ES)	10. SPONSORING/MONITORING AGENCY REPORT NUMBER
Defense Advanced Research Projects Agency
1400 Wilson Boulevard, Arlington, VA 22209

Office of Naval Research
800 North Quincy Street, Arlington, VA   22217-500 | |

11. SUPPLEMENTARY NOTES

N/A

12a. DISTRIBUTION/AVAILABILITY STATEMENT	12b. DISTRIBUTION CODE
Unlimited	

13. ABSTRACT (Maximum 200 words) This report describes progress on developing Y-123 wire for an HTSC motor. The wire is produced by spinning and heat treating fiber to produce metallized superconducting filaments. Development continued on spinning Y-123 green fiber. The diameter of continuous Y-123 green fiber was reduced to 75 microns. A belt furnace is being reconfigured for continuous sintering of fibers and a prototype cladding module for multi-filament ribbon wire is being fabricated. There has been an improvement in 77°K (self-field) critical current density of Y-123 filaments, up to $2400A/cm^2$ for the best filament, with $1500 A/cm^2$ for a typical filament. Similar results are seen for silver clad filaments. Preliminary data suggests an important effect of specimen length on transport critical current of thin filaments of weak-linked specimens. At Emerson Electric the characteristics of DC homopolar, DC heteropolar, reluctance, and induction HTSC motors were determined theroretically. A DC homopolar and an induction motor with superconducting stator windings were selected as final candidates for the proof-of-principle motor. M. Hilal of the University of Wisonsin developed a model for AC losses in HTSC wire, including eddy current and hysteresis losses.

14. SUBJECT TERMS		15. NUMBER OF PAGES
Superconductor, ceramic, motor		131
		16. PRICE CODE

17. SECURITY CLASSIFICATION OF REPORT	18. SECURITY CLASSIFICATION OF THIS PAGE	19. SECURITY CLASSIFICATION OF ABSTRACT	20. LIMITATION OF ABSTRACT
Unclassified	Unclassified	Unclassified	

COMPOSITE CERAMIC SUPERCONDUCTING WIRES FOR ELECTRIC MOTOR APPLICATIONS

EXECUTIVE SUMMARY

This report describes progress on producing Y-123 wire for an HTSC motor. The wire development activity includes synthesis of Y-123 powder, spinning polymer-containing "green fiber", heat treating the fiber to produce metallized superconducting filaments, and characterizing the electrical properties of the filaments.

The Y-123 powder was upgraded to a jet milled grade with improved sinterability. The jet milled powder is produced at 8 kilograms/week with reproducible particle size distribution. We have produced spools of green fiber from the improved jet milled Y-123 powder. This fiber was used to prepare sintered Y-123 filaments with improved critical current density.

Melt spinning process development for green fiber continued. Several new carrier polymers were evaluated. The primary focus was preparing finer fibers. The minimum diameter of continuous Y-123 green fiber was reduced to 75 microns.

Development was begun for a simpler type of wire, consisting of a silver clad Y-123 monofilament. Short lengths of prototype monofilament wire have been produced. The processing steps for the new type of wire are similar to those of ribbon wire, but a separate cladding module is not needed.

A commercial belt furnace was received and is being reconfigured for continuous sintering of fibers. Attempts at continuous fiber sintering are underway. A prototype cladding module was designed and is being fabricated. Solder clad copper strips for cladding ribbon wire were received and bonded in a prototype reflow unit.

The major effort in characterization is determining resistive transition and self field critical current for sintered bare and Ag-clad fibers. We continue to develop methods for making reliable contacts. There has been an improvement in 77°K (self-field) critical current density of Y-123 filaments, up to 2400 A/cm^2 for the best filament, with 1500 A/cm^2 for a typical filament. Similar results are seen for silver clad filaments. This increase is attributed to improved Y-123 powder. Preliminary data suggests an important effect of specimen length on transport critical current of thin filaments of weak-linked specimens.

The characteristics of a homopolar, DC heteropolar, reluctance, and induction motor were determined theoretically to define their suitability for superconductor technology. A DC homopolar and an induction motor with superconducting stator windings were selected as final candidates for the proof-of-principle motor. M. Hilal of U. Wisconsin has developed a model for AC losses in HTSC wire, including eddy current and hysteresis losses.

TABLE OF CONTENTS

LIST OF FIGURES

LIST OF TABLES

COMPOSITE CERAMIC SUPERCONDUCTING WIRES FOR ELECTRIC MOTOR APPLICATIONS

JOHN W. HALLORAN
PRINCIPAL INVESTIGATOR
CERAMICS PROCESS SYSTEMS CORPORATION
MILFORD, MASSACHUSETTS

SECTION 1

GENERAL INTRODUCTION

This Third Quarterly Report covers activities during January through March 1989, on a program to develop high temperature superconducting wire by cladding $YBa_2Cu_3O_{7-x}$ (Y-123) ceramic fibers with metal, and to use this wire to build a superconducting motor. This program is being carried out by three subcontractors: an affiliate of Ceramics Process Systems, CPS Superconductor Corporation (CPSS) is charged with development of the wire; the fiber spinning technology is being developed with Albany International Research Corporation (AIResCo); and the Emerson Motor Division (EMD) of Emerson Electric is designing and will build the superconducting motor. Another contributing organization is the University of Wisconsin Applied Superconductivity Center, which is acting as a consultant to Emerson Electric on motor design and the properties of high temperature superconductors.

The status of the program is compared with individual tasks of the Statement of Work in Table 1.1. Figures 1.1 and 1.2 show timelines for the major fiber and wire development tasks, comparing actual progress with the original program schedule. Actual program activities have diverged somewhat from the original work statement, as we exploited new opportunities, pursued alternatives to electroplating for cladding, and worked through difficulties.

The changes mostly reflect the fact that the program involves development of a process with about fourteen major steps, most of which are novel, and which must be developed in parallel. This has delayed our progress in the last two steps, continuous sintering and cladding, which require spools of high quality sinterable green fiber as feedstock. Development of the fiber spinning process itself progressed faster than scheduled, using a substitute material as powder, but transferring this to Y-123 powder was slowed by the availability of high quality Y-123 in sufficient quantity. We have developed four different grades of Y-123 powder in kilogram quantities, and evaluated their behavior in the form of spun fibers. The present grade, which appears to be satisfactory, became available in quantity during this quarter.

The changes in the program activities also reflect new development activities arising from new and better ideas on how to make HTSC fiber and wire. The statement reflected the original plan to dry spin fibers, sinter and anneal in-line, and clad with copper by electroplating. This was aimed at a HTSC composite wire consisting of a copper clad Y-123 monofilamentary fiber. The primary task of the AIResCo subcontract was to scale up the dry spinning process and design a pilot plant for dry spinning at CPSS. Early in the program, however, we developed a melt spinning process, yielding a better green fiber which could be produced using existing facilities at AIResCo. The dry spinning pilot plant design activity became unnecessary.

The wire design concepts also evolved to consider a multifilamentary wire in the form of a flexible ribbon, produced by cladding a flat braid of Y-123 filaments. The preferred cladding method is to solder bond the braided filaments to a thin copper strip. The process plan is to melt spin Y-123 fibers, apply a thin silver coating (to make them wet solder),

braid the green fibers into a flat belt, sinter and anneal in-line, and clad by soldering to copper strip.

The development of a convenient process of applying a silver coating then led us to the concept of a simpler style of Y-123 wire in which the silver coating was complete metallization. This would allow us to produce useful lengths of continuous HTSC wire before the base metal cladding process was completed, offsetting the higher cost of a noble metal cladding. This process plan is to apply a thicker silver coating, sinter, then anneal as a separate step, to make silver clad wire. This wire will be first made as a silver clad monofilament, but could be made as a multifilament using a loose yarn or a braided belt of silvered green fiber.

The following sections describe in detail the progress on the wire manufacturing task and the motor design task. Section 2 covers all aspects of the wire manufactuing development, incuding the fiber spinning work conducted at Albany International Research Corporation in Mansfield, Massachusetts, and the Y-123 powder production, sintering, cladding, and characterization work conducted at CPS Superconductor in Cambridge, Massachusetts. Section 3 outlines the HTSC motor design activities at Emerson Motor Division in St. Louis, Missouri, and also has an analysis of AC losses in HTSC wire by Mohamed Hilal of the University of Wisconsin, Madison, Wisconsin.

TABLE 1.1

PROGRESS AGAINST STATEMENT OF WORK
THIRD REPORT PERIOD: FIRST QUARTER 1989

TASK I: COMPOSITE WIRE MANUFACTURING
SUBTASK IA) POWDER PRODUCTION
    1) Supply consistent powder for fiber spinning at CPS and AIResCo
    STATUS: THIS IS BEING DONE
    2) Continue study of effects of surface area, particle shape, particle
    size distribution on fiber spinning and sintering
    STATUS: CONTINUING AT REDUCED EFFORT

SUBTASK IB) GREEN FIBER DEVELOPMENT
    1) Supply continuous green fiber dry-spun at AIResCo to support
    sintering activities
    STATUS: SUPPLYING CONTINUOUS MELT SPUN FIBER
    2) Continue green texture studies on CPS and AIResCo green fiber, using
    both shear texturing and magnetic orientation
    STATUS: NO ACTIVITY
    3) Begin refining first generation dry spinning dope and/or developing
    second generation dry spinning dope for process improvement at AIResCo
    STATUS: NOT NECESSARY, SINCE MELT SPINNING HAS BE ADOPTED

SUBTASK IC) FIBER SINTERING AND MICROSTRUCTURE DEVELOPMENT
    1) Initiate detailed study of effect of microstructural and textural
    parameters on 77 K critical current
    STATUS: LESS EMPHASIS ON MICROSTRUCTURE EFFECTS
    2) Continue development and upgrade laboratory scale continuous
    sintering furnace
    STATUS: MAJOR ACTIVITY THIS QUARTER

SUBTASK ID) FILAMENT CLADDING DEVELOPMENT
    1) Incorporate sintered fiber in continuous cladding facility to prepare
    short lengths of complete wire
    STATUS: DELAYED
    2) Deliver short lengths of complete wire to EMD for preliminary
    evaluation
    STATUS: DELAYED
    3) Deliver short length samples of complete wire to DARPA
    STATUS: DELAYED

TASK II: **CHARACTERIZATION**
     1) Determine critical current of wire samples in presence of magnetic
field and relate to wire microstructure and processing
STATUS: MEASURING SELF FIELD CRITICAL CURRENT OF BARE AND CLAD SPECIMENS
     2) Define the effect of handling and mechanical loading on critical
current of wire to determine damage thresholds
STATUS: DELAYED UNTIL CLAD WIRE AVAILABLE

TASK III: MOTOR DESIGN AND CONSTRUCTION
     1) Continue literature research on superconductive motors and mechanical
systems that can operate at liquid nitrogen temperature
STATUS: ONGOING
     2) Continue Application Study of military and civilian applications for
HTSC motors, identify all motor applications and markets
STATUS: DELAYED UNTIL WIRE PERFORMANCE IN MAGNETIC FIELD DEFINED
     3) Determine maximum mechanical stresses of wires wound under various
manufacturing processes
STATUS: COMPLETED
     4) Update wire property targets for design database
     5) Continue study of physical properties, effect of environment, test
requirements and test methods for HTSC conductors

```
              1988          1989                    1990               1991
              J A S O N D J F M A M J J A S O N D J F M A M J J A S O N D J F M
                1  |  2  |  3  |  4  |  5  |  6  |  7  |  8  |  9  | 10  | 11  |


              CPSS
              lab scale
FIBER         dry spin
DELVP         [========]

original        AIRC dry spinning
schedule        development        process development
              [=================][======================]


                                    Dry spinning pilot line
                               .design  build        optimize
                               .[=====][===========][==========]

                1  |  2  |  3  |  4  |  5  |  6  |  7  |  8  |  9  | 10  | 11  |


              Rh-P dry
              spin fiber
              [======---]
                 CPSS dry spin fiber
FIBER            [=================------
DEVLP

              BaTiO₃ melt spinning
              [====================-------

actual
schedule        Y-123 melt spinning
              [==============================================]

                                  Green fiber weaving
                               [=======================]


                1  |  2  |  3  |  4  |  5  |  6  |  7  |  8  |  9  | 10  | 11  |
```

Figure 1.1   Above: Original Project Schedule for Fiber
               Below: Actual Project Activities for Fiber

```
                   1988          1989                        1990                    1991
                   J A S O N D J F M A M J J A S O N D J F M A M J J A S O N D J F M
                    1  |  2  |  3  |  4  |  5  |  6  |  7  |  8  |  9  | 10  | 11  |
                   Lab                  .
                   Sinter               .
                   [=======]            .
TASK IC&ID                              .
                          sinter        .
                          continuous    .
WIRE                      [========     .
                                        .    Lab scale continuous
original                                .        sinter and plate
schedule                                .    [======================]
                   Lab plate            .
                   [=======]            .
                          contin.       .
                          plate         .
                   [=========           .
                                        .
                                        .
                                        .       Wire pilot line
                                        .
[=================================================================
                    1  |  2  |  3  |  4  |  5  |  6  |  7  |  8  |  9  | 10  | 11  |
                   Lab sinter           .
                   [=====================--
                                        .
                          RTC furnace   .
                          [============  .
WIRE                                    .
                                        .           Ribbon wire
DEVLP                                   .     [=================================
                                        .
actual                    Cladding module
schedule                  Design and build
                          [===============/
                   Silver coat and co-fire
                   [==========================-------------------
                                        .
                          Silver monofil wire
                          [==============================================
                    1  |  2  |  3  |  4  |  5  |  6  |  7  |  8  |  9  | 10  | 11  |
```

Figure 1.2   Above: Original Project Schedule for Wire Tasks
                  Below: Actual Project Schedule for Wire Tasks

SECTION 2
WIRE FABRICATION

ZONGYI CHEN, JOHN HALLORAN, JAMES HODGE, LORI JO KLEMPTNER,
MATTHEW NEAL, MARK PARISH, VIREN PATHARE, AND RAYSHA PICERNO
CPS SUPERCONDUCTOR CORPORATION

GEORGE BAKIS, DANA EAGLES, WESLEY ISHIDA, AND STEPHEN TIERNAN
ALBANY INTERNATIONAL RESEARCH CORPORATION

2.1   Introduction and General Comments

This Quarter saw the introduction of an improved jet milled grade of Y-123 powder, substantial progress in the melt spinning of continuous green Y-123 fiber, and the beginnings of continuous sintering development. Cladding development progressed in two areas, including the completion of the design of the ribbon wire cladding module and adaptation of the silver coating process to produce silver alloy clad wire. The self field critical currents achieved by the bare and silver clad fibers were routinely between 1000 and 1500A/cm^2, with one filament reaching 2400 A/cm^2. We also have gained more insight into the statistics of critical current measurements for weak linked conductors.

The detailed progress reports for each of the four wire process steps are presented in Sections 2.2 through 2.5.

2.2   **Fiber Preparation**

2.2.1 Introduction

During this Quarter continuous spools of melt spun green fiber were routinely produced. Dry spinning was used only to prepare small samples of fibers for evaluation of nine lots of experimental Y-123 powders. More than 15 successful melt spinning runs (and a number of less successful

experiments) were conducted to evaluate new polymer blends, investigate process variables, reduce fiber diameter, and develop procedures for working with the high surface area jet milled Y-123. These involved barium titanate, ball-milled Y-123, and six different lots of the new jet milled Y-123.

The ultimate objective of the fiber development is a manufacturing process for an easily handled green fiber, suitable for sintering, with a diameter fine enough to yield a flexible Y-123 filament. The filament will be flexible if it is small enough that the _elastic_ strains due to flexing will be too small to damage the superconducting ceramic. If the filament is exactly at the mechanical neutral axis of a wire, the maximum elastic tensile strain is related to the diameter, D, and the bending radius, R, by:

$$R = D/(2e)$$

If we set the maximum allowable strain at only e=0.0005, a filament with a diameter of 10 microns will withstand a bending radius of 1 cm, which we have taken as our goal for flexibility. Thus, ultimately we want to produce green fiber with diameters of about 10-15 microns, or about a half mil. This establishes our target diameter for green fiber. The larger diameter fiber we have produced to date will give us less flexible wire. The fiber spinning development is set up to search for methods to reduce diameter, while still providing early samples of larger fiber to serve a feedstock for the development of less flexible prototype wire.

2.2.2 Evaluation of Alternate Polymers

Substantial effort in this quarter was devoted to evaluating different carrier polymers for green ceramic fibers. As before, these

evaluations were performed using a $BaTiO_3$ powder[1] as a surrogate for Y-123. This quarter several different grades of polymethylmethacrylate (PMMA) and polypropylene (PP) and three grades of poly(alkylene)carbonate were evaluated.

Previous attempts to melt spin fibers with PMMA were unsuccessful. However, these grades of PMMA had relatively high melt indices. Our experience with HDPE and EVA, which were successfully spun into green fiber, suggested that a low melt index enhances spinnability. Consequently we attempted to spin fibers with a new lower melt index grade of PMMA. Attempts to compound with this new grade were unsuccessful because the polymer would not melt in the sigma blade mixer. Blends containing a variety of mixtures of high and low melt index PMMA, with and without lubricant, were prepared for evaluation. Unfortunately, all these compositions were either paste-like or powder-like after compounding, and were not suitable for melt spinning. We have dropped PMMA as a candidate carrier polymer because of its poor spinnability evaluation and because of the unfavorable binder burnout behavior previously reported.

Green fibers with polypropylene as the carrier have shown very good draw, allowing finer diameters to be produced. This work continued with a new grade of PP with a lower melt index polypropylene carrier. After adjusting the polymer/lubricant ratio to improve melt strength, a blend was prepared which could be extruded from a 343 micron die into fiber with a diameter as small as 25 microns. The 25 micron $BaTiO_3$ fiber was the thinnest diameter 50 vol% ceramic loaded fiber produced to date. This achievement

---

[1]. TICON-HPB, a barium titanate powder with specific surface of 3.5 m^2/g and median particle size of 1.2 microns (by our analysis). TAM Ceramics, Inc., Niagara Falls, NY

qualified this grade of PP for further evaluation with Y-123 powder.

The QPAC series of poly(alkylene)carbonates from Air Products are attractive as carriers because of their lower binder burnout temperatures and lack of reactivity with Y-123, as determined in the previously reported binder reactions studies. Several lots of QPAC-40M, a polypropylene carbonate resin, were evaluated. Simple mixtures of the polymer and powder did not compound well since the QPAC did not melt in the sigma blade mixer. Addition of lubricant resulted in a soft compound which was extrudable, but the melt strength was insufficient to take up the fiber. Several blends were made at a variety of polymer/lubricant ratios, but only poor quality fibers with little drawability were obtained. The poor melt strength of the blends was attributed to three possible causes: residual solvent in the polymer feed stock, which could be removed by vacuum drying; too low a molecular weight, requiring the use of a different grade of QPAC polymer; or plasticization of the QPAC polymer by propylene carbonate, a decomposition product.

A new lot of QPAC-40M was received and compounded into a 50 vol% $BaTiO_3$ blend, but was similar to the previous QPAC-40M blends. Further evaluation of QPAC-40M was discontinued when it became apparent that the polymer degrades during compounding, producing polypropylene carbonate which plasticized the blend excessively. A sample of a higher molecular weight grade of the polypropylene carbonate, designated 40H, was evaluated because it offered a higher melt strength which could offset the plasticizing effect of the degradation products. Unfortunately, this grade could not be successfully compounded on the sigma blade mixer, so the evaluation of QPAC-40H was terminated. Although QPAC-40H could not be compounded in the sigma blade mixer, it may be a viable candidate for evaluation in a higher shearing

Brabender prep mixer. This type mixer will be available in the next quarter. QPAC-10040, a high molecular weight terpolymer, was evaluated as the final candidate from the QPAC series. A blend was mixed, but not extruded because it had the same paste-like appearance as the previous unsuccessful blends of QPAC-40M.

To date it appears that PP and HDPE are the best polymer choices for melt spun processing. Celcon may become a candidate once greater volumes of YBCO raw material is available for use on a twin screw extruder or a higher shear mixer, such as the Brabender.

2.2.3 Green Fiber Diameter Reduction

One method of achieving thinner diameter green fiber is to post-spin draw the fibers. Previously it was observed that upon heating the post-spin drawn fiber samples would shrink back to their original dimensions, resulting in linear shrinkage of 50 % or greater. This was believed due to the "memory" effect of oriented thermoplastic polymers. It was thought that thermal relaxation of stresses resulting from post-spin drawing operations could minimize the linear shrinkage observed upon heating.

In order to define the effect of increased polymer orientation on fiber shrinkage during sintering a feed stock blend of 50 vol% $BaTiO_3$ with polypropylene was spun into fibers with diameters of 318, 165 and 50 microns. The 165 and 318 micron fibers were subsequently drawn at a variety of conditions to achieve thinner fibers. The post-spin drawing was done at temperatures around 150°C, since it was hoped that hot drawing might cause less polymer orientation than cold drawing. The fibers were fired to 900°C, which completes binder burnout without causing sintering for barium titanate.

The as-spun fibers experienced little shrinkage, consistent with the fact that as-spun fibers subject the thermoplastic polymer to the least amount of elongational strain. All the post-spin drawn fibers suffered axial shrinkages around 50-70%, with expansion of the diameter up to 90%. (Diametral expansion accompanies axial shrinkage to maintain approximately constant volume.) It is clear that hot drawing at 150°C does not relax polymer orientation induced by drawing.

Note that dry spun fibers show almost no linear shrinkage during heating. This can be attributed to the lack of molecular orientation during solvent drying and the three-dimensional polymer network resulting from the cross linking of the PMMA polymer used in dry spun fiber fabrication.

Table 2.2.1 presents some of the mechanical test data for selected samples from the BaTiO$_3$ fiber drawing experiments to show how diameter reduction during drawing affects fiber strength. Recall that increased strength after cold drawing reflects the increased degree of orientation of the polymer segments. If hot drawing at 150°C in fact was hot enough to relax away orientation induced during drawing, we expect relatively little strength increase. Note, however, that strength and modulus are substantially increased, reflecting polymer orientation induced by drawing. As noted above, this will result in pronounced shrinkage upon heating during sintering. The fiber hot drawn at 157°C has a lower strength and modulus for the same draw ratio, indicating that some relaxation can be obtained at slightly higher temperatures.

TABLE 2.2.1

INFLUENCE OF WARM DRAWING ON THE TENSILE PROPERTIES
OF BARIUM TITANATE/POLYPROPYLENE GREEN FIBERS

DRAW RATIO	DRAW TEMPERATURE °C	DIAMETER microns	STRENGTH psi	MODULUS psi	ELONGATION %
as spun	- - -	318	- -	- -	- -
2	150	233	2270	64,300	8
6	150	140	6650	102,000	14
8	150	117	8260	133,000	11
6	157	142	2660	93,900	26

2.2.4 Processing of Jet Milled Y-123 Powder

The jet milled Y-123 powder is significantly different than the previous ball milled powders used for melt spinning. At 1.6 microns, the particle size is much finer, and the 2.7 m^2/gm surface area is correspondingly larger than other Y-123 powders used for melt spinning. The powder is also prepared without an organic processing aid, and so has a distinctly different surface character than the previous stearic acid or polyethylene glycol treated powders. One or both of these makes the spinnability of the new powder quite different.

The jet milled YBCO powder was evaluated with both HDPE and PP. The focus of this work was to test different ceramic, polymer, and lubricant compositions to achieve fabrication of the thinest possible green fiber for a particular polymer resin.

The first blend in this series had a composition of 33 vol% HDPE, 17 vol% lubricant, and 50 vol% YBCO/5 wt% CuO. Upon extrusion, the melt appeared too stiff to draw satisfactorily. The thinest achievable diameter was 330 microns from a 343 micron die, much thicker fiber than the 114 micron diameter fibers achieved using roller-milled YBCO. To collect thinner fibers, a 178 micron multi-filament die was used to fabricate continuous fibers of 178 micron diameter.

A PP blend analogous to this HDPE series was made from YBCO/5 wt% CuO powder and spun into fiber as thin as 75 microns from a 343 micron die. This PP blend had much lower viscosity and better drawability than its HDPE counterpart. This sample of 75 mocron fibers represents the thinnest 50 vol% YBCO/PP fibers fabricated to date in this program.

In order to further reduce the YBCO green fiber diameter, a 50 vol% YBCO/5 wt% CuO PP blend with less lubricant was compounded. The thinnest fiber diameter obtained for this was 3 mil, the same as the previous blend. However, the reduced lubricant blend had a low enough viscosity to allow an experiment to determine the effect of screen pack filtration on fiber processing. For this experiment. a 325 mesh (38 micron) screen pack was placed between the die insert holder and the tapered section in the die assembly of the extruder. Extrusion with the screen pack caused no greater pressure drop across the die assembly than without the screen pack. The minimum fiber diameter achievable for this blend was the same with and without the screen pack in place. These results suggest that this blend did not contain agglomerates large enough to clog the 325 mesh screen and that the current minimum fiber diameter of 75 microns is not limited by the presence of agglomerates.

A new HDPE/Y-123 composition with a lower melt strength was compounded in an attempt to achieve fiber diameters less than 178 microns with this blend. This blend had a higher lubricant concentration, which improved the drawing ability of the melt. The thinnest fiber diameter achieved was 190 microns from a 343 micron die.

To date we have not been able to prepare HDPE-based fibers with as fine diameter with the new powder, although the PP-based compositions have finer diameters even with the jet milled powder. In order to further reduce fiber diameter using an HDPE/jet milled YBCO composition, it may be necessary to choose a different grade of HDPE that would be less viscous. An HDPE grade with higher melt index will be evaluated in the next quarter

To lower the viscosity of the HDPE containing blend and improve

the processing characteristics of this resin we tried a mixture of equal amounts of the HDPE composition and a PP composition. In processing characteristics this blend is similar to an HDPE-only blend, so the stiffer HDPE polymer characteristics dominated. The minimum continuous fiber diameter achieved with this blend was 190 microns from a 343 micron die. This result emphasizes the need for evaluating a higher melt index grade of HDPE resin.

In order to achieve further fiber diameter reduction using PP resin a blend with reduced lubricant was prepared. This blend exhibited a low viscosity, similar to the two other PP/YBCO-5% CuO blends, but had better drawability, resulting in fiber as thin as 50 microns in diameter from a 343 micron die. This 50 micron fiber sample is the thinest 50 vol% YBCO/PP green fiber to date in this program. The low viscosity and minimal pressure drop during processing of this blend suggest that it would be suitable for processing through a smaller diameter die than the 343 micron die. Assuming equal draw ability and reasonable extrusion processing pressures with a smaller diameter die, the extrusion of a blend of this composition from a 75 micron die should give a 12.5 micron green fiber, the target green fiber diameter.

Unfortunately, it was discovered upon sintering that the Y-123 powder was not homogeneously mixed with the 5 wt.% CuO sintering aid. Consequently, these fibers could not be used for further processing. This mixing problem has now been corrected.

Subsequent melt spinning work was done with phase pure jet milled Y-123 powders. A PP blend using this powder was prepared. It did not compound well, so only small samples of 100 micron non-continuous fiber was obtained from a 343 micron die. Thicker fiber was not obtainable due to the

low viscosity of this blend. This phase pure jet milled YBCO powder processed differently than its CuO containing analog. The reason for this is not yet clear. During sintering fibers from this PP had relatively poor shape retention, often forming a flat spot where they contact the substrate.

In order to make both 125 and 250 micron green fiber to supply sintering needs using phase pure jet milled powder, the HDPE blend had to be prepared with twice the normal lubricant content. This blend was also compounded for twice the regular length of time to assure good homogeneity of the mixture. Extrusion of this blend yielded 125 micron discontinuous fiber lengths and 165 micron continuous fiber from a 343 micron die. These fiber samples are currently being used for sintering and cladding work.

Activities in the coming quarter will involve improving the melt spinning process for the HDPE and PP systems. While effort will continue to prepare finer diameter fiber, a "standard" 100-125 micron green fiber will be produced to supply the sintering and cladding development activities. Particular attention will paid to attributes of the fiber which impact the move to continuous sintering.

2.3   Heat Treatment of Fibers

2.3.1 Introduction

In contrast to the previous quarters, most of the effort in this three month period was aimed at establishing procedures for continuous sintering of fibers. The major events were the evaluation of the new jet milled Y-123 powder, in the form of pellets and fibers, and the installation and modification of the RTC belt furnace. More attention was paid to co-firing of silver-alloy coated Y-123 fibers. A significant amount of effort

was expended to prepare specimens especially for development of procedures for electrical measurement.

2.3.2 Evaluation of Jet Milled Y-123 Powder

Jet milling was identified as a preferred comminution method for the Y-123 powder during the second quarter. In January we installed a jet mill and shifted our powder production exclusively to this grade of powder. Considerable effort was expended in qualifying this process and optimizing process parameters. This involved extensive powder analysis, sintering studies, and electrical measurements on sintered filaments made from the new powder. Table 2.3.1 lists the particle size[2] and surface area[3] of eight of the more recent production lots of Y-123 powder, showing that the median particle size is reproducible at about 1.6 microns, with constant surface area around 2.5 m^2/gm. This demonstrates substantial lot-to-lot uniformity with the finest particle size Y-123 powder we have produced to date in kilogram quantities.

The sintering behavior of the jet milled Y-123 powder was characterized in the form of dry pressed pellets, dry spun fibers, and melt spun fibers. Simple dry pressed pellets, prepared at about 50% green density, were exposed to conventional two hour furnace sintering treatments at various temperatures in air. Table 2.3.2 shows that densities on the order of 95% can be achieved at 960°C or above.

---

[2]. By Horiba centrifugal sedimentation method.

[3] By multipoint BET

TABLE 2.3.1

CHARACTERISTICS OF JET MILLED Y-123 POWDERS

POWDER LOT	MEDIAN DIAMETER (micron)	SUBMICRON FRACTION (wt.%)	SURFACE AREA (m^2/gm)
02394	1.6	29	2.7
03033	1.7	23	2.7
03025	1.7	24	2.5
03029	1.5	26	2.7
03030	1.6	25	2.5
03006	1.7	27	2.3
03018	1.8	23	2.3
02326	1.7	25	2.8

TABLE 2.3.2

SINTERED DENSITIES OF DRY PRESSED JET MILLED Y-123 POWDER

TEMPERATURE	TIME	DENSITY	%THEORETICAL
920°C	2 hr	5.78 g/cm^3	92.3
960	2 hr	5.98	95.6
970	2 hr	5.93	94.6
980	2 hr	5.98	95.7
990	2 hr	6.08	97.3

2.3.3. Microstructure Development of Fibers from the Jet Milled Powder

Microstructure development work for melt spun fibers made from the jet milled Y-123 in the tube furnace to date have involved only examining the previously determined optimum temperatures for stoichiometric Y-123 (990°C) and CuO-doped Y-123 (935°C). Some results for the stoichiometric composition are briefly presented in Figure 2.3.1 and 2.3.2. Figure 2.3.1 shows fracture surfaces of a 135 micron diameter fiber sintered for 6 passes in the tube furnace with a 990°C peak temperature. A point count indicates a density of about 94%. Increasing the number of passes to 10, equivalent to 30 rather than 18 minutes, improves the density to 96%, as indicated in Figure 2.3.2. The 10 pass fiber also has a noticeably larger grain size, although it is not possible to accurately determine grain size for these transgranular fracture surfaces.

An extensive series of sintering experiments on fibers melt spun from CuO-doped Y-123 were discarded after considerable effort was expended examining what seemed to be anomalous sintering behavior. The problem was eventually related to inhomogeneous distribution of the copper oxide additive, which had been dry blended into the separately jet milled stoichiometric Y-123. The fibers produced from this inhomogeneous blend were discarded. Results from new, presumably uniform, CuO-doped fibers are not yet available.

2.3.4 Microstructure Development in the RTC

Efforts were begun to translate experience in zone sintering fibers in the old tube furnace to the new RTC belt furnace. This is not as direct as it might seem. As explained in the previous report, our multiple zone sintering method involves repeatedly moving the specimen through the hot

zone of a tube furnace. The fiber actually spends very little time at constant temperature, since it is usually being heated or cooled. Its thermal history is dominated by details of the heat transfer to the fine fiber. We characterize the thermal history with the temperature-time record of a thermocouple traveling with the fiber, but since heat transfer to the thermocouple is not the same as heat transfer to the fine fiber, the thermocouple record (and peak temperature) is not an exact indication of the thermal history of the specimen.

Microstructure development experiments in the RTC were conducted with a technique similar to the tube furnace experiments. Green fibers supported on alumina substrates, were first given our usual binder burnout treatment consisting of heating in a nitrogen rich atmosphere to 500°C at 5-10°C/minute, followed by cooling in air. The substrates with the fibers, were placed directly on the metal mesh belt of the RTC so that the fibers were sintered in contact with the alumina substrates. For sufficiently low temperatures and short times, we see no evidence of reaction between the Y-123 and the alumina. As a practical matter, it is the sticking of the Y-123 fiber to the substrate, caused by incipient reaction, which limits the temperature and time of sintering.

The operating principle of the RTC is quite different from the tube furnace. In the tube furnace, the control circuitry maintains the relatively massive alumina tube at the set point temperature. Moving the sled through the hot zone does not upset the thermal balance, since the dominant thermal mass is the hot tube. The fibers enter an isothermal radiant cavity, and experience heat transfer primarily by radiation from a constant temperature source. With the tube furnace, we could conveniently change fiber

speed without significantly changing peak temperature.

In contrast, the RTC controls the power to quartz lamps based on the output of a control thermocouple. Deviations in the thermocouple output change the effective radiator temperature, which modifies the T^4 heat transfer rate to restore the control thermocouple to its set point temperature. This control thermocouple controls temperature one inch above the belt. The control circuitry is very effective to maintain the balance in the radiative cavity to keep the control temperature quite constant at the set point. However, a traveling thermocouple experiments show that the peak temperature recorded by the thermocouple on the belt changes with belt speed. We presume that the temperature achieved by the belt, and the temperature experienced by the fiber also differ from one another and are different from the set point temperature.

This can be understood if we realize that for the case of light thermal loads of ware, the moving belt is the major thermal load being introduced into the radiative cavity. The temperature achieved by the belt will be whatever effective steady state temperature required to maintain the set point temperature at the control thermocouple above the belt. This thermal balance is upset when the thermal load changes due to a belt speed change, so the belt temperature will move to a new value which re-establishes the thermal balance. This means that with the RTC furnace, we cannot change belt speed independently of peak temperature.

For example, a series of traveling thermocouple experiments were conducted with the three zones of the RTC furnace set at 885, 996, and 885°C. Belt speeds of 8, 4, and 1.5 inches/minute produced peak readings in the traveling thermocouple of 980, 1014, and 1025°C, respectively. Figure 2.3.3

compares two of the time-temperature profiles. During these tests, the control thermocouple stayed accurately fixed on the 996°C set point. Note that the actual belt temperature could undershoot or overshoot the set point furnace, depending upon the belt speed. Thermal balance is established closer to the set points when the set point is the same in the three control zones and the belt is run relatively slow. One experiment, with all three RTC zones set to 996°C and belt speed at 2.5 inches/minute, recorded a peak temperature of 1000°C, essentially the same as the set point.

Typical temperature-time records for the tube furnace and the RTC belt furnace are compared in Figure 2.3.4. Both furnaces are set at 996°C. The profile for the tube furnace is for our usual sled speed of two inches/minute, which leads to an initial heating rate around 100°C/minute. Notice that the initial heating rate is much more rapid in the RTC furnace. Most RTC sintering experiments to date have been done at 8 inches/minute, with a heating rate starting at 250°C/minute, which increases to more than 900°C/minute above 200°C.

Figure 2.3.5 shows the fracture surface of a melt spun fiber prepared from jet milled powder after sintering for 6 passes in the RTC at a belt speed of 8 inches/minute and a nominal set point temperature of 996°C (actual peak temperature was 980°C). These six passes correspond to a total of 12 minutes above 900°C. This fiber from the RTC furnace, at 75-80% dense, is still quite porous.

To illustrate how sintering conditions differ in the tube furnace at the same nominal peak temperature, examine Figure 2.3.6, a fracture surface for a similar fiber after sintering at an actual temperature of 996°C for six passes (which corresponds to 18 minutes total sintering time). This specimen

is essentially fully dense, and is beginning to suffer grain growth. Clearly, the RTC and the tube furnace sintering conditions for the same nominal temperature and number of passes, are not comparable, since the actual temperature-time profiles are quite different.

It is possible to achieve high density in the RTC furnace by simply increasing the number of zone passes. Figure 2.3.7 shows a fiber after 16 passes in the RTC at 996°C set point, using the same 8"/minute belt speed (so actual peak temperature was 980°C). This corresponds to a total time of 32 minutes above 900°C. The fracture surface indicates a substantially denser microstructure, around 90% dense by point count. This particular fiber was dry spun, which is why it does not have a round cross section.
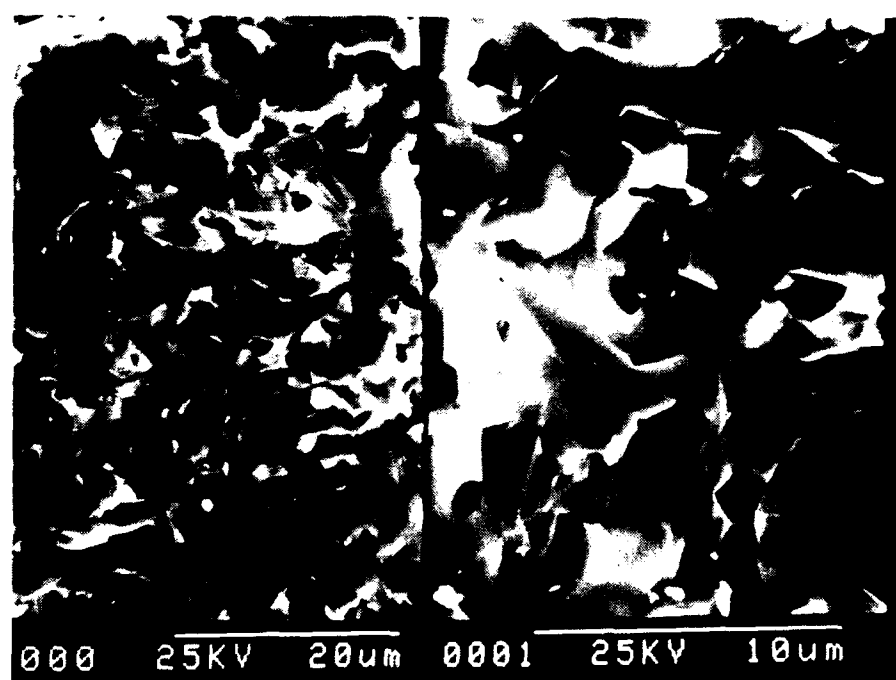
Figure 2.3.1   Fracture Surface of Fiber Sintered for 6 Passes in the Tube Furnace with 990°C Peak Temperature
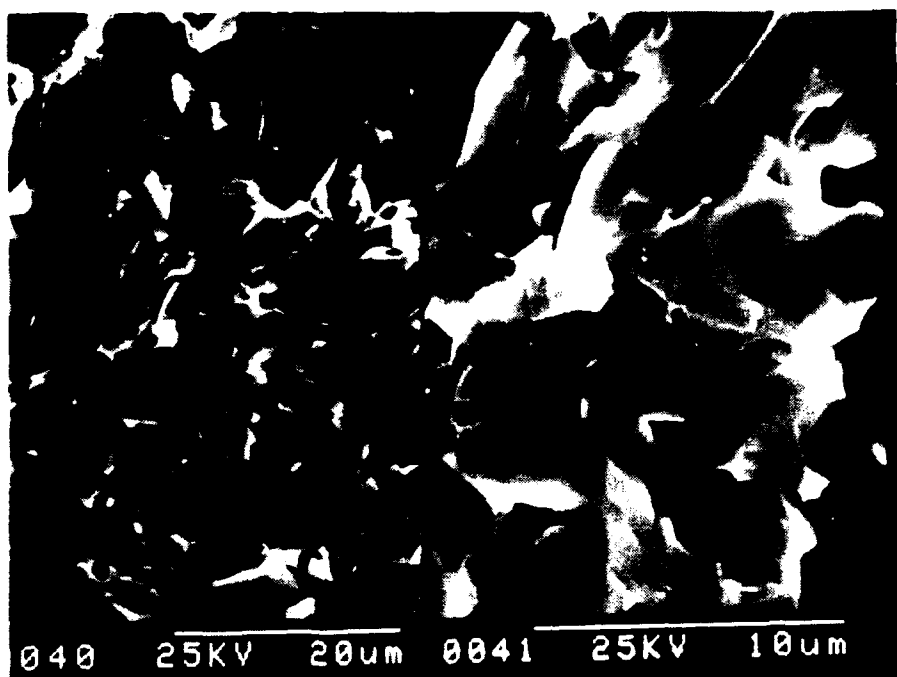
Figure 2.3.2   Fracture Surface of Fiber Sintered for 10 Passes in the

Tube Furnace with 990°C Peak Temperature
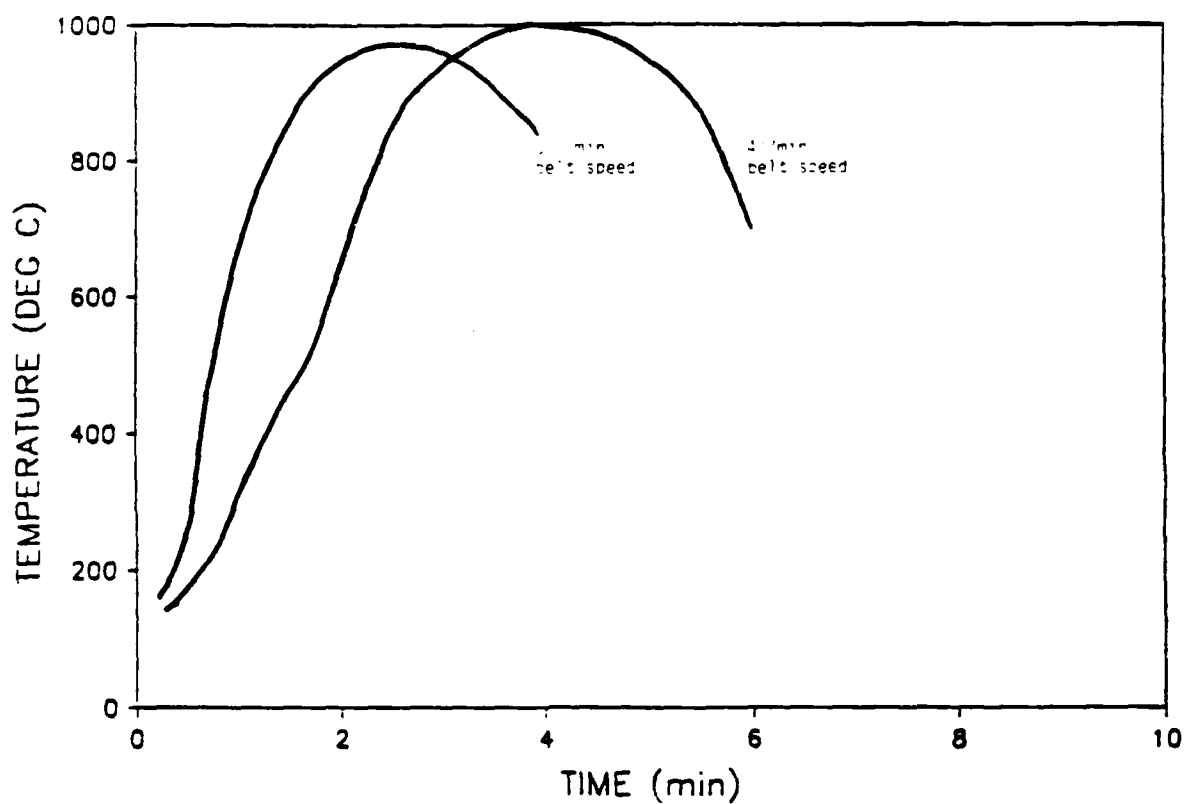
Figure 2.3.3   Time-Temperature Profiles for the RTC Furnace with the
Central Zone set at 996°C, at Belt Speeds of 4
inches/minute and 8 inches/minute
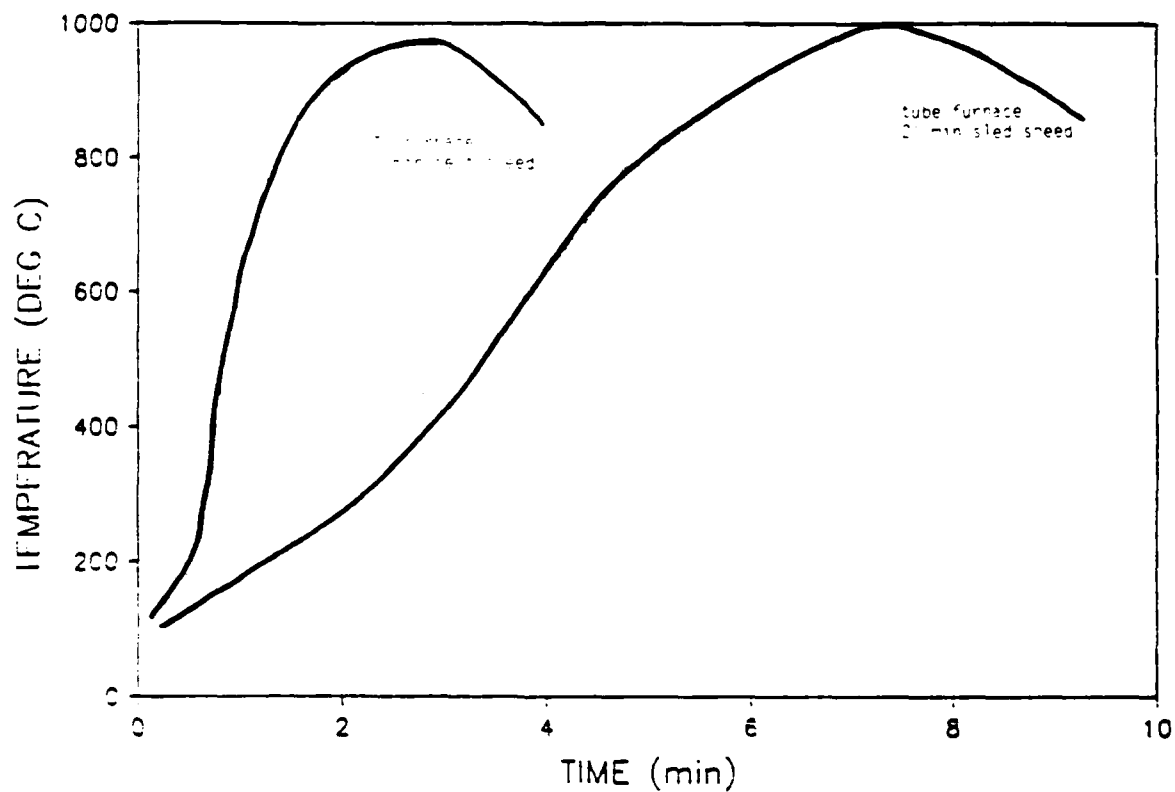
Figure 2.3.4   Time-Temperature Profiles of the Tube Furnace and the RTC furnace. Both furnaces are set at 996°C
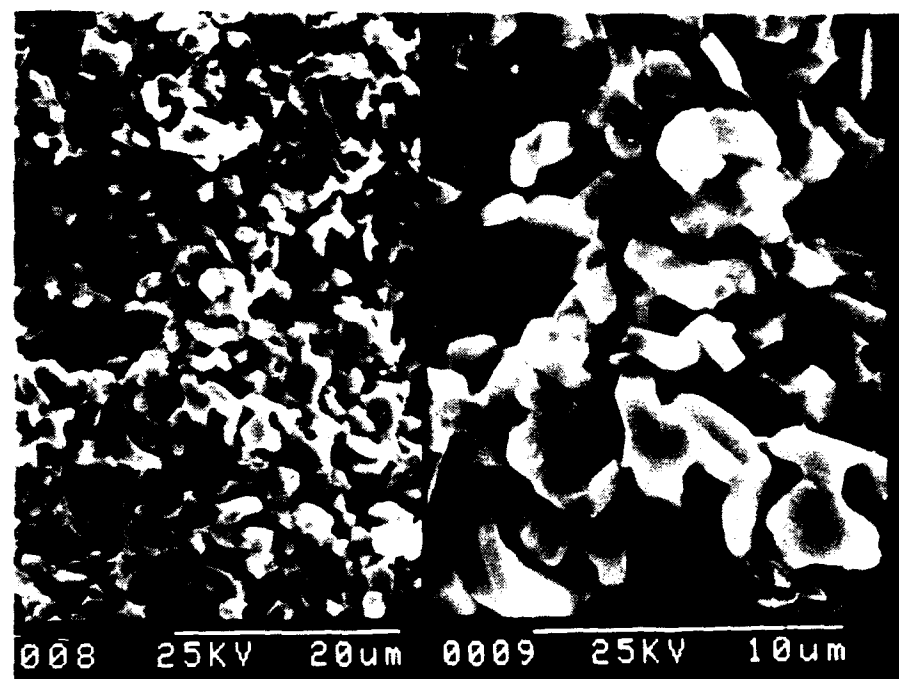
Figure 2.3.5   Fracture Surface of a Fiber from Jet Milled Powder after

Sintering for 6 passes in the RTC at 8 inches/minute with

a Set Point 996°C, Actual Peak Temperature 980°C
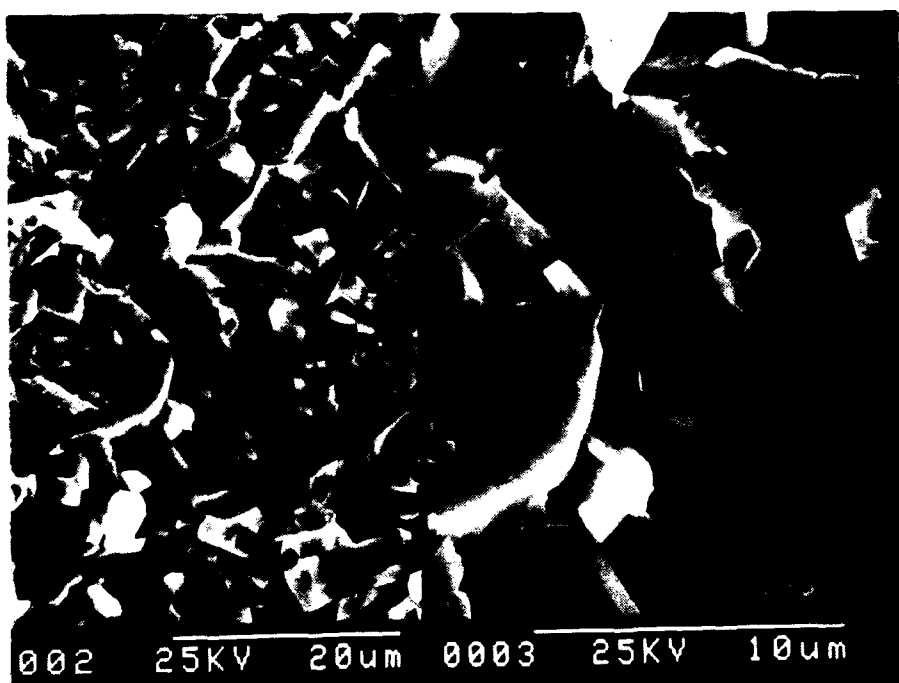
Figure 2.3.6   Fracture Surface for a Similar Fiber sintered in the Tube

Furnace at Peak Temperature of 996°C for Six Passes
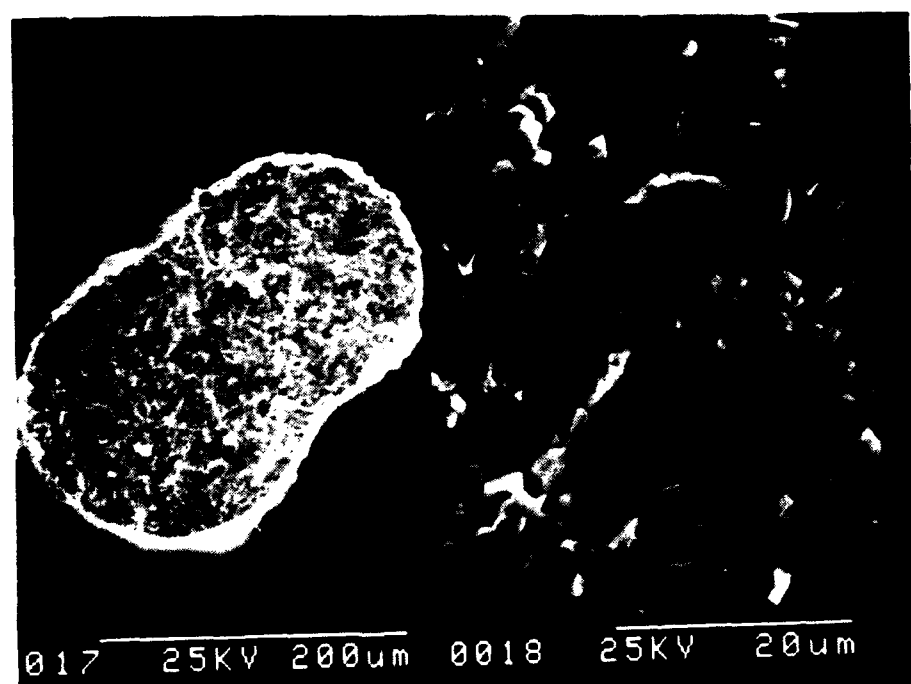
Figure 2.3. 7   Microstructure of a Fiber after 16 Passes in the RTC at

8 inches/minute, 996°C Set Point, Actual Peak 980°C

2.3.5 Adaptation of the RTC for Continuous Fiber Sintering

The RTC belt furnace arrived early in this quarter. Unfortunately, we were not able to immediately use it effectively, due to bugs in the unit and the need to make certain adaptations. Much of January and February was spent tracking down and fixing a number of electronic bugs in the furnace control system. This occupied much time and effort. These electronic problems are now all resolved. About an equal amount of effort was spent on several modifications to convert this commercial belt furnace into a unique fiber sintering apparatus.

The RTC belt furnace was obtained to serve both as an experimental furnace for fiber sintering, and as the prototype for the laboratory scale continuous sintering furnace. For the former purpose as an experimental furnace, we have installed a belt reversing mechanism, so that we can conveniently do multipass experiments by moving a short (about one meter) fiber back and forth through the hot zones. Obviously, in the continuous sintering mode, the belt is not reversed. If multiple zones are desired for continuous sintering, the RTC will be suitably modified.

A second modification is to replace the metal mesh belt with a ceramic fiber belt, so the Y-123 fibers are not fired in contact with the alloy belt. We are currently evaluating suitable woven ceramic fabrics. Preliminary work has been with a plain weave tape of Nextel 440. This appears to be satisfactorily compatible with Y-123. Our early results, however, show that the Nextel tape was being damaged by the metal mesh belt drive mechanism. This mechanism is being modified.

Early trials in which green fiber was directly introduced into the

RTC furnace revealed some problems with binder combustion. This occurs on occasion when the fibers are very rapidly heated in air. In relatively static air, the ignition tends to be confined to a narrow zone, so the green fiber burns like a fuse. In a draft of heated air, the green fiber can burn much more vigorously. A similar problem was observed with short fibers in the tube furnace, when an occasional green fiber would be ruined. The situation is intolerable in the case of continuous sintering, since even a rare occasional combustion event serves to disrupt the continuity of the fiber. The very rapid heating rate at the entry zone, 500°C/min, exacerbates the problem. In any case, the ignition can be suppressed by restricting the oxygen partial pressure in the entry zone. An attempt to do this by simply introducing nitrogen at the entry baffle was partly effective. Enough air apparently leaks in at the entrance to cause problems with the more difficult larger diameter fibers. A shroud is being prepared to allow the entry area to be purged with nitrogen.

The independent problem of fiber shrinkage upon initial heating due to polymer relaxation has become important as we transition to continuous sintering. As explained in Section 2.2.3, relaxation of post-drawn fibers can cause significant axial shrinkage. It happens that the fibers used in the continuous sintering trials, which were early melt spun from jet milled powder, suffered some shrinkage and similar distortions. This lead to breakage of the fiber in the RTC. This problem is being addressed in fiber formulations.

The net result of all these problems was that the early continuous sintering attempts were unsuccessful. Continuous green fiber was hand-payed out onto the Nextel tape, but discontinuous 5-25 cm fragments emerged on the

exit end. This was disappointing, but we can hardly expect success in our first attempt. Each problem is being addressed. We have confidence that we will, one by one, eliminate the problems which frustrate our continuous sintering attempts.

2.4　　Filament Cladding and Wire Fabrication

2.4.1　Introduction

The main thrust of the cladding effort this quarter was directed toward assembling the Flexible Ribbon Conductor, as described in previous reports. Briefly, the ribbon is to be fabricated by sandwiching an array of sintered filaments between two solder-overlaid copper foil strips, and bonding these by a reflow operation. This operation is to be conducted in a cladding module, which will be installed at the exit of the sintering furnace. The design of the cladding module was the principal task during this quarter.

The Y-123 filaments cannot be directly solder bonded, since the oxide is poorly wetted by the solder. To effect this bonding, the Y-123 must be silvered with a thin coating of a silver alloy. This coating is applied onto the green fiber using fine powders of silver alloys. The metal coating and the ceramic fiber are sintered simultaneously -- or co-fired-- so that both coating and substrate have optimal microstructures. The application of the silver coating and development of the co-firing process were the other main tasks during this quarter.

During this quarter we also began development of a derivative of this process in which the entire cladding consists of the silver alloy coating. The process is essentially the same as is being developed to silver the filament surfaces for the ribbon wire, except that the amount of silver

alloy is increased to the level desired for the metal/superconductor ratio of the wire. The result is a monofil wire, consisting essentially of a silver alloy wire with a Y-123 core. The thicker coating is expected to require a longer oxygen intercalation anneal, so we anticipate collecting spools of sintered silver clad tetragonal Y-123, which would be subsequently oxygenated by a suitable long anneal.

2.4.2 Monofilamentary silver clad wire

For flexibility, the HTSC core of the wire should be as thin as possible. From a practical standpoint, this is limited only by handling - ability of the fiber. The Ag alloy thickness is limited by two factors: oxygen annealing and dilution of the metal/superconductor ratio. Both depend upon the square of the metal thickness. For mechanical properties, the more silver the better; but too much silver leads to high metal/superconductor ratios.

For a simple wire with a HTSC core of diameter d_{sc} and the outer wire diameter d_{Ag}, the metal/superconductor ratio, M, is given by:

1) $M = (d_{Ag}/d_{sc})^2 - 1 = A_{Ag}/A_{sc}$

The tensile properties of the wire can be modeled by determining the relationship between a tensile load applied to the composite wire, P, and the actual tensile strain suffered by the HTSC core, ϵ_{sc}. If we accept some value, ϵ_{max}, as the maximum tensile strain which the ceramic can safely bear (say 0.0005), then the maximum tolerable tensile load P_{max} can be calculated.

The elastic strain in the HTSC core is the combination of the applied elastic strain and the elastic strain resulting from residual stresses in the silver cladding. This can be expressed in terms of the fraction of the

applied load born by the HTSC core, P_{sc}, and the residual stress in the silver cladding, σ_r, as:

$$2) \quad \epsilon_{sc} = \epsilon_{sc.appl} + \epsilon_{sc,r} = P_{sc}/[A_{sc}E_{sc}] + \sigma_r M/E_{sc}$$

where E_{sc} is the elastic modulus of the superconductor. The load in the superconductor is related to the total load, P, the metal/superconductor ratio, M, and the relative elastic modulus of the cladding and the superconductor, $G=E_{Ag}/E_{sc}$ by:

$$3) \quad P = P_{sc}(1+MG)$$

Combining (2) and (3) gives an expression for the maximum tensile load that the composite wire can withstand:

$$4) \quad P_{max} = [\epsilon_{max} - \sigma_r M/E_{sc}]A_{sc}E_{sc}[1+MG]$$

This expression shows how the load tolerance increases with the metal/-superconductor ratio and the relative modulus. Notice that load tolerance of the wire directly depends upon the amount of residual stress. This residual stress arises primarily from the thermal expansion difference between the silver and the HTSC, and will be compressive on the ceramic and tensile on the metal, in the case of cooling. (A compressive stress means that σ_r is negative in Equation 4). To be able to estimate the strength of the composite wire, one must understand the magnitude of the thermomechanical residual stress.

Cooling the composite wire from the sintering temperature will create $\delta\alpha\delta T$ thermal stresses, placing the ceramic core in compression. This can be modeled elastically by equating the axial strain in the core and the alloy clad. This strain involves both thermal strain ($\alpha_i\delta T$) and elastic strain:

$$5) \quad \alpha_{sc}\delta T + (\sigma_{sc}/E_{sc}) = \alpha_{Ag}\delta T + (\sigma_{Ag}/E_{Ag})$$

Now the stresses in the two materials are related, since each bears equal but opposite loads, i.e., the alloy bears a tensile load, P, while the core carries a compressive load (-P):

$$6) \quad \alpha_{sc}\delta T - (P/A_{sc}E_{sc}) = \alpha_{Ag}\delta T + (P/A_{Ag}E_{Ag})$$

One can solve for the load and express the tensile stress in the alloy as:

$$7) \quad \sigma_{Ag} = P/A_{Ag} = \frac{E_{Ag}(\alpha_{sc} - \alpha_{Ag})\delta T}{[(A_{Ag}/A_{sc})(1/E_{sc}) + (1/E_{Ag})]}$$

This can be written more neatly in terms of the metal/superconductor ratio, M, and relative elastic moduli, G:

$$8A) \quad \sigma_{Ag} = \{E_{Ag}(\alpha_{sc} - \alpha_{Ag})\delta T\}\{MG+1\}^{-1}$$

Similarly, the compressive stress in the HTSC core is given by:

$$8B) \quad \sigma_{sc} = - \{E_{sc}(\alpha_{sc} - \alpha_{Ag})\delta T\}\{1 + G/M\}^{-1}$$

Notice that 8A and 8B are simply the thermal mismatch $E\delta\alpha\delta T$ term modified to consider geometry and relative moduli.

These equations, 8A and 8B, are elastic, so cannot take into account plasticity effects. Plasticity certainly comes into play during cooling, since the strains exceed the elastic limit. For example, examine the magnitude of the thermal mismatch stress term for the silver:

$$E_{Ag}(\alpha_{sc} - \alpha_{Ag}) \approx 0.6 \text{ MPa/°C}$$

Cooling from 900°C to room temperature without yielding would induce more than 70,000 psi stress in the alloy. This is greatly in excess of the plastic yield stress, so obviously the silver flows during cooling. Furthermore, one should expect the cladding to creep during cooling and during the long 500°C oxygen anneal, reaching a zero stress condition. One must consider the kinetics of stress relaxation to estimate the retained residual stress. Also, upon cooling to liquid nitrogen, thermal mismatch strains will probably cause

yielding in the alloy. This may be a problem. Cycling between room temperature and 77°K might cause mechanical hysteresis, eventually placing the ceramic core in tension. The mechanical metallurgy of the cladding needs attention.

Now consider relaxation of thermal mismatch stresses in silver clad wire. Much of the stress is developed at temperatures where the metal can rapidly creep, which will relax away a portion of the stress. (Here we are just considering the silver cladding, which is bonded to the ceramic at the sintering temperature. Creep relaxation will also play a role in the ribbon wire, since the solder will readily creep at lower temperatures.) To estimate the level of residual stress, we have to know at what temperature stress relaxation is slow enough to "freeze in" the thermomechanical stresses.

Stress relaxation is also important during oxygen intercalation of silver clad Y-123 filaments to accommodate the volume __decrease__ associated with the tetragonal-orthorhombic transformation. If the silver cannot creep, the clad will act as a rigid tube, making the ceramic fiber suffer radial tension so it is likely to degrade by microcracking.

Fortunately, creep in silver is well documented so data is available to calculate approximate relaxation rates. We can start with some creep rate data of Ghosh and Mitra[4] which we can fit to a creep law of the form:

9) $\qquad d\epsilon/dt = B(\sigma/G)^n$

$\qquad$ where: $d\epsilon/dt$ = plastic strain rate

$\qquad\qquad\qquad \sigma$ = applied elastic stress

---

[4] R. N. Ghosh and S.K. Mitra, Metal Sci. 17, Dec. 1983,p.590

G = shear modulus = 15 GPa for Ag

n = stress exponent = 4.7 for Ag in this range

B = kinetic constant

= $1.9*10^{19}$/sec $*$ exp(-28.3kcal/RT), as

derived from Ghosh and Mitra's data

Using this creep law, one can express the time dependent stress, σ, in terms of the initial stress, σ_i, with:

$$10) \quad \sigma^{i-n} = \sigma_i^{i-n} + (4B(n-1)G^{1-n})t$$

Notice that this expression is for steady state creep rates, so ignores transient creep. It is therefore a conservative predictor of residual stresses, and an underestimator of plastic creep strains.

It turns out that stress relaxation is very rapid in silver at the oxygen intercalation temperature range around 500°C. Table 2.4.1 shows the stress as a function of time for a "fixed grips" type of constant strain condition, such as the case of rapidly quenched in thermal mismatch stress. The initial stress level is chosen at 10 MPa, which is near the yield stress[5] at 500°C.

Most of the stress relaxes away in about a minute at 500°C, so any thermal mismatch stress in the silver is removed during the oxygen intercalation anneal. This also means that the silver creeps easily at this temperature, so the volume contraction of the Y-123 core caused by oxygen intercalation and tetragonal-orthorhombic transformation should be easily accommodated.

---

[5] T. Maruno, et al.,J. Japanese Institute of Metals,47,(9),pp.768-775,(1983)

The very rapid relaxation at 700°C suggests that the thermal mismatch stresses during cooling from sintering temperature should be dynamically relaxed. Relaxation at 300°C is slow enough to preserve thermomechanical stresses during a rapid cool from intercalation temperature to room temperature.

It is now possible to estimate the room temperature residual stress. Starting from zero stress after intercalation, thermomechanical stress builds up from around 300°C or so, depending upon cooling rate. If unrelieved, this stress builds up at a rate around 0.6 MPa/°C, which is more than enough to cause plastic yielding. So the upper limit of residual stress in the silver is approximately the same as the room temperature yield stress, which is about 30 MPa for pure Ag or 50 MPa for 20% Pd.

TABLE 2.4.1

STRESS RELAXATION KINETICS IN SILVER
INITIAL STRESS — 10 MPa

TIME	300°C	500°C	700°C
0 sec	10 MPa	10 MPa	10 MPa
0.01 sec	10 MPa	9.8 MPa	7.5 MPa
1.0 sec	10 MPa	6.3 MPa	2.4 MPa
100 sec	8.6 MPa	1.9 MPa	0.7 MPa
10^4 sec	3.1 MPa	0.6 MPa	0.37 MPa

2.4.3 Co-firing of Silver Alloy Coated Green Fibers

The composition of the silver palladium alloys are chosen by their liquidus temperature which, for constant particle size, largely determines the sintering temperature. The primary concern is avoiding melting during cofiring. The apparent temperature[6] at which melting becomes a problem is significantly lower than the liquidus. For example, pure silver coatings melt away at peak temperatures above 930°C, although the melting point is 960°C. At least some of this discrepancy is due to reaction of the silver with oxygen, leading to eutectic melting of $Ag-Ag_2O$. The Ag-15Pd alloy, with a 1030°C liquidus, is useful up to 1000°C and the Ag-18Pd composition, 1060°C liquidus, is useful up to 1030°C. We find that silver powders with finer particle size melt at lower temperatures, presumably because of more rapid formation of the Ag-O eutectic.

The process for applying the silver alloy coating on Y-123 green fiber was improved through a series of process modifications. Improvements in fiber handling, primarily to reduce frictional loads, have allowed us to significantly increase the length of green fiber which can be continuously coated, and to coat thinner fibers. Much improved fiber handling apparatus has been designed and will be incorporated in the coating unit when the components are received. Considerable activity was also devoted to improving the formulation of the silver alloy materials, principally aimed at improving the control and uniformity of coating thickness. By the end of the next quarter we expect to have a facility for coating entire spools of green fiber

---

[6] Recall that the actual temperature experienced by the fibers during zone sintering is not crisply defined, see Section 2.3.4.

on a reel-to-reel basis.

A series of experiments were conducted on co-firing of stoichiometric Y-123 green fiber coated with silver-palladium alloys. Unfortunately, the only continuous Y-123 green fiber strong enough to be handled in our coating apparatus at that time was made from a lot of relatively coarse (3.7 micron) powder. The substrate Y-123 fiber was therefore not sinterable under co-fire conditions, so these experiments only served to define the sintering behavior of the Ag/Pd alloy.

Pure silver claddings were found to be well sintered after 10 standard passes in the tube furnace at a peak temperature of 929°C, producing an adherent coating with silver grains 10-15 microns in diameter. Coatings of the Ag-15 wt% Pd alloy sintered well after 8 passes at a peak temperature of 939°C. Both coatings could also be sintered with a 10 minute isothermal anneal at 929°C.

2.4.4 Development of the Cladding Module

The design of the cladding module is complete, and all parts are either being fabricated or presently in hand. The cladding module is a stand-alone unit which accepts two spools of solder overlaid C10200 copper foil strips. The foil strips are pulled into an alignment unit which places them over and under the sintered fibers, pulls the assembly into a reflow unit, past a cooling zone, and onto a 61 cm diameter spooler. The speed control of the cladding module can be synchronized with the sintering furnace. The reflow unit consists of stainless steel blocks heated to 350°C with 200 watt cartridge heaters. This unit has been tested successfully. The solder overlaid copper strips can be continuously reflow bonded when pulled through

the heated blocks at 5-8 cm/minute. A design feature of the reflow unit is an arrangement to contain the molten solder between the copper strips. This eliminates the need to form one of the strips into a shallow channel, simplifying the process, and allowing a symmetrical ribbon wire to be directly produced.

2.4.5 Properties of Silver Clad Filaments

The physical properties of the silver clad filaments are quite different from bare Y-123 sintered fibers. They look and behave much like silver wire. They are much stronger than bare filaments and much easier to handle. We have not yet measured their mechanical properties. This work is planned for later this year when continuous wire is available. The clad filament bends as if it were ductile, although the substrate Y-123 core inside is certainly damaged by bending. They can be directly electroded with solder.

The critical current of the Ag clad filaments is the key question. In spite of its obvious importance, we have not yet entirely determined if the electrical properties are affected by the silver alloy coating. A large body of literature indicates that silver has either a beneficial or a benign effect on the properties of Y-123. We must determine the effect of Pd, which appears unreactive, but may have some undesirable effects. The silver alloy coating may also have an indirect effect on properties, if it alters oxygen inter-calation kinetics.

We have not been able to establish this yet, since we have primarily worked with short fibers. Uniform coatings cannot be applied to short fibers, and our ability to continuously coat green fiber lags some weeks behind our ability to spin green fiber. There are several reasons for this

lag. First, we typically characterize the behavior of the new spools of bare fiber to examine its polymer relaxation shrinkage, burnout behavior, sintering behavior, and sometimes electrical properties before adopting the fiber for further work. Second, changes in the polymer system of the green fiber sometimes require some coating system adjustments. For example, the adjustments in the polymer blend adopted to spin the jet milled powder affected the adhesion of the coating system, requiring considerable adjustment of the coating procedure. Finally, our early continuous coating apparatus places excessive tractions on the fragile fibers, so the green fibers must be particularly strong to continuously coat. Moreover, the newest and most promising specimens are first identified as dry spun fibers from experimental powder runs. To execute these as melt spun continuous ag coated fibers can take 4-6 weeks. For this reason, the substrate green fibers for the continuous coated case tend to be older and sometimes obsolete.

We have examined the electrical properties of two types of silver alloy clad specimens, which can be designated as co-fired or re-fired. Co-- fired are those which are silver coated in the green state, and fired once to develop the microstructure of both the alloy and the Y-123. These are more relevant for the processing, but are less developed and so tend to have relatively poor Y-123 microstructure at present. The properties reflect the poor substrate quality. Re-fired specimens are prepared by silver coating previous sintered Y-123 filaments, which are then given a second sintering treatment optimized for the metal phase.

Much of the critical current data have been obtained on re-fired specimens. This data will be presented in more detail in Section 2.5. For the present is suffices to note that a silver coated re-fired filament,

annealed 2 hours at 500°C in oxygen, exhibited a critical current of 1300 A/cm^2, while a second re-fired filament annealed in air for 64 hours had a critical current of 1700 A/cm^2.

These are similar to the performance of bare Y-123 filaments.

2.5   Electric and Magnetic Characteristics

2.5.1 Measurement Techniques

The instrumentation and measurement technique for determining the resistivity versus temperature is essentially the same as reported previously. Briefly, this involves scanning temperature between 140 and 77°K in a liquid nitrogen cryostat controlled by a Lake Shore 805 temperature controller. Temperature is measured with a silicon diode thermometer. The sample filament is electroded in a four-point geometry using either silver epoxy over sputteredd silver pads or fired-on silver contacts. Sample excitation is with 1.12 Hz 1.0mA square waves with 440ms plateaus. The algorithm for data acquisition is similar to what was described in the previous report, with some improvements. For typical filaments, our "zero" resistivity is lower than 10^{-7} Ω-cm.

Figure 2.5.1 shows the resistive transition for a particularly good bare Y-123 filament (027042C) made from jet milled powder in the form of a dry spun fiber sintered at 996°C in the tube furnace, and annealed two hours at 500°C in oxygen. This filament appears to be high quality Y-123, since it has quite low normal state resistivity for bulk Y-123, around 60 $\mu\Omega$-cm at 100°K and 154 $\mu\Omega$-cm at 258°K. The temperature dependence in the metallic region is essentially linear at 0.53 $\mu\Omega$-cm/°K, which is similar to high

quality single crystal Y-123[7]. The transition is sharp with an onset at 92.7 and zero resistance at 90.2°K.

The critical current measurements are done in a liquid nitrogen bath in self field. Filaments are mounted on a sample holder in a four point configuration. A computer controlled data acquistion system, operating on an algorithm described previously, increases the DC current in a step wise fashion to record voltage response as a function of current. This is converted to electric field vs. current density, with the critical current defined by an electric field criterion[8] of 1 μV/cm. The data is taken well out into the normal regime to establish the "n-value" for the voltage-current relationship:

$$V/V_o = [I/I_o]^n$$

An example of the electric field-current density data for one of the more extensively studied filaments (3306C3) is displayed in Figure 2.5.2. The one microvolt/cm criterion is satisfied at about 720A/cm$_2$, which cannot clearly distingushed on the scale of this plot. Data in the range of the criterion is more clearly displayed in a semilog version of the same data, Figure 2.5.3, which indicates the precision with which J_c is defined and the noise level of the voltage gradient below the critical current density.

2.5.2 Electrical Properties of Filaments with Deposited Base Metals

---

[7]. J. Greybeal, M.I.T. personal communication

[8]. Note that in the Second Quarterly Report we used a different criterion for the critical current. When the old data were reanalyzed using the electric field criterion, the values of J_c were not significantly different.

We have conducted further characterization of the filaments which had been clad with various metals by outside collaborators. In the previous report, we described non-aqueous electrodeposition work done at the National Institute for Standards and Technology by David Lashmore and Gery Stafford. Using 200 micron diameter Y-123 filaments prepared from dry spun fiber from Rhone-Poulenc powder, Lashmore and Stafford successfully deposited an aluminum alloy coating from a $MnCl_2$ doped $2AlCl_3$:NaCl molten salt electrolyte. The claddings were dense 4.7 micron thick adherent deposits of an amorphous alloy of approximate composition 70 wt% Al-30 wt% Mn. No evidence of microstructural damage could be found by SEM examination.

The substrate filaments were still superconducting after molten salt deposition of the Al-Mn, as indicated by our simple float test. More quantitative data was provided by Lydon Swartzendruber of NIST, who measured the magnetization of bare and clad filaments at 77°K. Swartzendruber's data are presented in Figure 2.5.4. The magnetization of the Al-Mn clad filament suggested a Meissner fraction of 38% at 0.05kOe and 28% at 0.30kOe. This was actually higher than bare filaments from the same batch, which showed Meissner fractions of 42% at 0.05kOe and 10% at 0.30kOe. The bare filament, however, had been exposed to laboratory air for more than five months before measurement.

In spite of the superconducting Y-123 substrate, the clad fiber displayed no resistive transition. Figure 2.5.5 is the resistivity trace for the Al-Mn clad filament, indicating normal metallic behavior with no hint of any change around the critical temperature. The room temperature resistivity of 25 $\mu\Omega$-cm was calculated assuming that all of the current was carried in the 5 micron thick coating. Apparently a highly resistive or insulating barrier

has formed between the base metal alloy and the Y-123 which prevents current transfer to the superconducting core.

Similar behavior was found with Y-123 filaments clad with aqueous electrochemical methods. As previously reported, Professor Stanley Bruckenstein of SUNY-Buffalo deposited copper directly onto the Y-123 by electroless plating. When these were found to be no longer superconducting, he developed a procedure to deposit silver onto the Y-123, followed by copper on the silver. We recieved for analysis two types of specimens of clad 230 micron Y-123 filaments. One set was clad with a thin 2-3 micron coating of silver with a globular morphology, while the second had a thick 7-8 micron silver coating with a 2-3 micron copper overlay. The microstructure of the thicker coating suggested it was a strongly adherent brittle metal deposit. Both types of clad filament were superconducting by the float test. Figure 2.5.6 shows the resistivity data for these samples, which have no indication of a resistive transition, demonstrating that current is not being transfered from the cladding to the substrate Y-123 filament apparently due to a high resistance barrier at the metal/ceramic interface. These are apparent resistivities using the total filament cross section. The lower value for the the specimen with the silver plus copper cladding probably reflects the thicker cladding. Specimens with the thinner silver cladding were measured as recieved and after annealing at 500°C in an attempt to remove the suspected insulating barrier. The anneal did not remove the insulating barrier, but did decrease the normal resistivity, probably by consolidating the globular silver layer.

With the help of several collaborators, we have now had preliminary evaluations of CVD aluminum, electrodeposited aluminum,

electrodeposited copper and electrodeposited silver. All have developed resistive barriers. It is clear that base metals cannot be directly deposited on Y-123. For future work, we will supply our collaborators with Y-123 filaments with co-fired silver coatings to act as diffusion barriers between the superconductor and the deposited metal.

2.5.3 Development of Low Resistance Contacts

Contact resistance at the electrodes of our filaments has been a persistant problem and a source of irreproducibility in critical current measurements. In the previous report we described a protocol for silver epoxy contacts on sputtered silver pads, which, after a two hour oxygen anneal at 450°C, had been giving reasonably reproducible contact resistance around 10^{-4} ohm-cm^2. Unfortunately, further work showed this to be an unreliable method.

Fired-on silver contacts were developed for more reproducible contact resistance. These are made by painting sintered filaments with a suspension of silver powder, and re-firing the filaments to sinter the silver and bond it to the Y-123. Refire anneals were done at 925°C for six passes in the tube furnace, followed by an oxygen anneal at 500°C for two hours. This technique had the advantage of producing tenacious silver contacts with more reproducible resistances. It also produces a contact which simulates the co-fired silver metallization. One disadvantage of the fired-on contacts is that the processing "information" of the original sintering and annealing of the filaments are essentially erased by the second firing and annealing. This complicates the analysis of properties vs. processing.

2.5.4 Critical Current Data for Single Pairs of Contacts

Refired filaments made from jet milled powder have displayed the largest critical current densities yet seen in this program. Specimen 2760C was made from a 140 micron diameter dry spun fiber prepared with the jet milled powder. The filament was sintered in the tube furnace for the typical six passes at 996°C, and annealed for two hours at 500°C. After painting on a striped pattern of silver electrodes, the specimen was refired at 925°C for six passes, and given a second oxygen anneal. This specimen has an unusually sharp resistive transition and carried a critical current of 0.379 A, corresponding to a critical current density of 2450A/cm^2. The electric field-current density data for this filament is shown in Figure 2.5.7. A number of similarly processed filaments had critical current densities between 1500 and 2000A/cm^2.

We are tempted to attribute the increase in J_c to the use of the new jet milled powder. A number of experiments have been attempted to determine if the the increase is indeed attributed to the powder, or if it is related to processing changes, such as the double firing step. Results to date are inconclusive, since the scatter in J_c measurements have frustrated several series of experiments. We have determined that the higher J_c is not simply due to lower contact resistance. Contact resistance and critical current density data do nto display statistically significant corrolation. Moreover, filaments with good critical current density all have "good" resistive transitions, i.e., T_c is 87- 90°K. Poor current density filaments tend to have poor resistive transitions, with T_c below 86°K.

Refired contacts were typically applied as stripes, with the major part of the Y-123 filament left bare. This eliminated interference from a continuous metallic path, which complicates analysis of the resistive

transition. The bare filament surfaces were also thought to assist oxygen intercalation. Several experiments were conducted with continuous silver coatings, however, which showed that complete oxygen intercalation can take place through a continuous silver coating. Figure 2.5.8 shows the electric field vs. current density data for a filament which was completely coated with silver, refired, and oxygen annealed as before. The two traces show the apparent current density, using the total cross section, and the actual current density in the Y-123 after correcting for the metal/superconductor ratio of 1.1. The filament had a critical current density around 1300 A/cm^2, which is similar to bare filaments.

2.5.5 Multiple Contact Experiments

A series of experiments have begun multiple measurements on single filaments provided with six contacts, so that up to five different segments can be characterized by permuting the voltage tap leads. We were surprised by the variation in J_c between different segments of the same filament. To date we have examined five filaments with multiple contacts. In the most uniform specimen, the critical current densities varied only 7% between the segments. The least uniform specimen had up to 60% variations in critical current density.

These experiments are conducted by painting six striped electrode contacts on a sintered filament and re-firing the filament as described above. The contacts were about 1mm wide spaced 21mm apart in the central segment, and 3mm apart for the right and left segments. Contacts 1 and 6, at the ends of the filaments, were typically used for current leads. One pair of the remaining contacts (numbers 2,3,4, and 5) were chosen to determine the

critical current density by the usual technique. A complete analysis involved measuring all the unique pairs, providing J_c data for contact pairs 2-3, 3-4, 4-5, 2-4, 2-5, and 3-5. Repeated J_c over the same voltage taps showed good reproducibility, even if the current leads were changed.

Figures 2.4.9 to 2.4.11 show the results of the multiple contact experiments for three filaments made from melt spun fiber containing jet milled powder. These all had a first firing for six passes at 990°C, followed by a 2 hour oxygen anneal at 500°C. The re-fire conditions were six passes at 925°C, followed by another oxygen anneal. The first filament, 34008A, shown in Figure 2.4.9 has a critical current density of about 800A/cm^2 in the middle and left segments, while the right segment (segment 2-3) has a critical current density of 750A/cm^2. The critical current measured across the whole specimen, between contacts 2 and 5, is about 760 A/cm^2, reflecting the fact that it intersects the low J_c segment 2-3.[9]. Figure 2.4.10 shows that the right segment of filament 34008, with a J_c of 640A/cm^2, determines the critical current of the whole filament, even though the center segment carries 720A/cm^2.

Filament 3306C3 has a similar history, but has a much larger range of J_c values. Figure 2.4.11 shows that the center and left segments have values of 710 and 770A/cm^2, but the right segment 2-3 has a much larger

---

[9]. The values for the large spans, such as 2-5, should be slightly larger than the minumum J_c for the intervening short spans. The descrepancy arises from the "electric field criterion", which assumes a uniform voltage ditribution in the filament. This is not the case for an inhomogenous filament, since all of the voltage is dropped across the resistive segments. The 3mm short span 2-3 reaches the 1 microvolt/cm criterion with a voltage drop of 0.3f microvolt. The 28 mm long span 2-5 does not reach the apparent electric field criterion until the voltage drop exceeds 2.8 microvolts. Thus there is bias in the criterion which makes the J_c values slightly larger for larger spans.

critical current density of 1710A/cm^2. The J$_c$ of the whole filament, 2-5, is close to the worst segment.

Filament 3306C3 also exhibits differences in critical temperature from one location to another. Figure 2.5.12 shows the resistive transitions measured on over three segments of the filament. The T$_c$ is only 85°K over the center segment (measured between contact 3 and 4) and the left segment (contact 4 and 5), while there is a sharper transition at 88°K in the right segment of the filament (between contacts 2 and 3). As described above, the critical current density differs by a factor of 2.4 between the best and worst segment. The normal state resistivity is high for all segments, and is about 40% higher in the center and right segments. We are attempting to identify the reason for the difference in these properties.

We are continuing multiple contact experiments for several reasons. First, we hope to use them to pinpoint the poorer regions of the filaments, which can then undergo detailed microstructural examination in an effort to relate microstructure to properties. Secondly, it is an economical way to gather data on the statistical variation of J$_c$ with segment length. This data is particularly important. We must use short length specimens to characterize continuous wire, so the theoretical basis for such extrapolation must be established. It may be that "weak linked" superconductor filaments, with the critical current for the entire filament governed by its worst segment, would have J$_c$ values distributed according to extreme value statistics. This could lead to a Weibull distribution function governing the J$_c$ statistics. This has serious implications for producing long lengths of weak link wire able to carry even the modest critical currents seen in short filaments. If the J$_c$ data are in fact Weibull distributed, then one would

express the probability that a filament of normalized length, L, would possess a critical current greater than a current, I, is defined as $P_L(I \leq I_c)$, by an expression of the form:

$$P_L(I \leq I_c) = 1 - \exp[-L(I/I_o)^m]$$

where: I_o = the characteristic critical

current for a filament of length l_o

$L = l/l_o$ is the normalized length

m = distribution modulus

The implication of this expression is that the chances of producing a wire capable of carrying a given current becomes very small when the wire gets long enough for the argument of the expotential to approach unity.
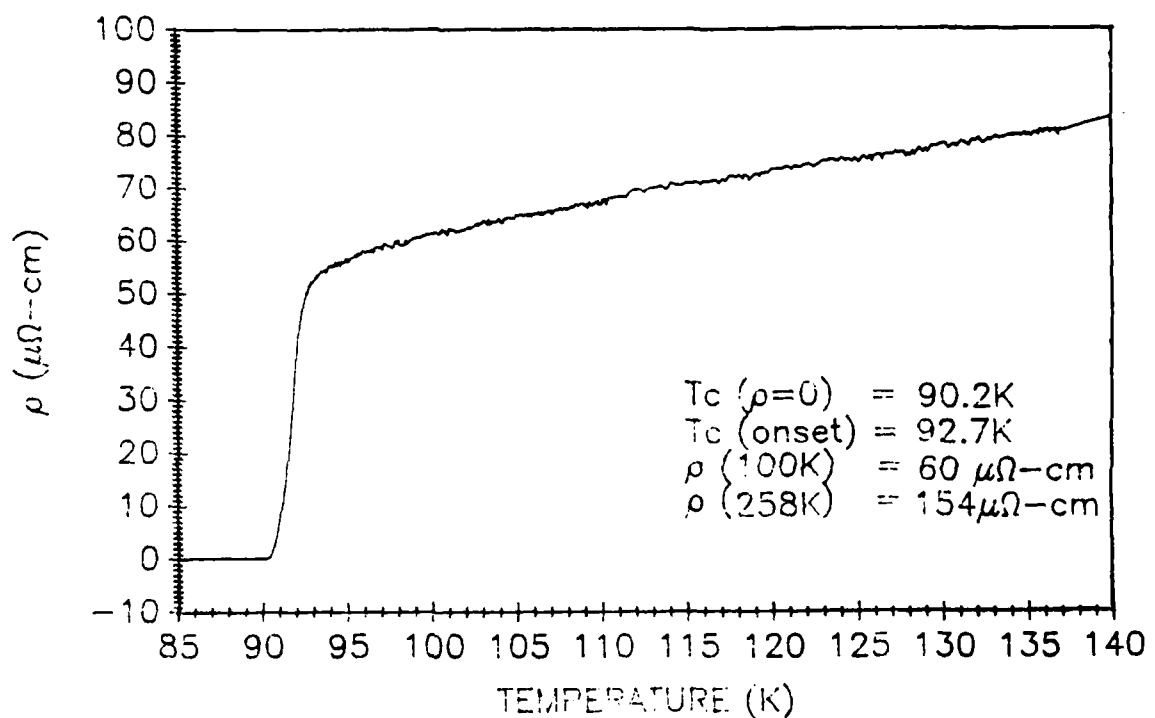
Figure 2.5.1   Resistive Transition for Bare Y-123 Filament Number
027042C Made from Jet Milled Powder as a Dry Spun
Fiber
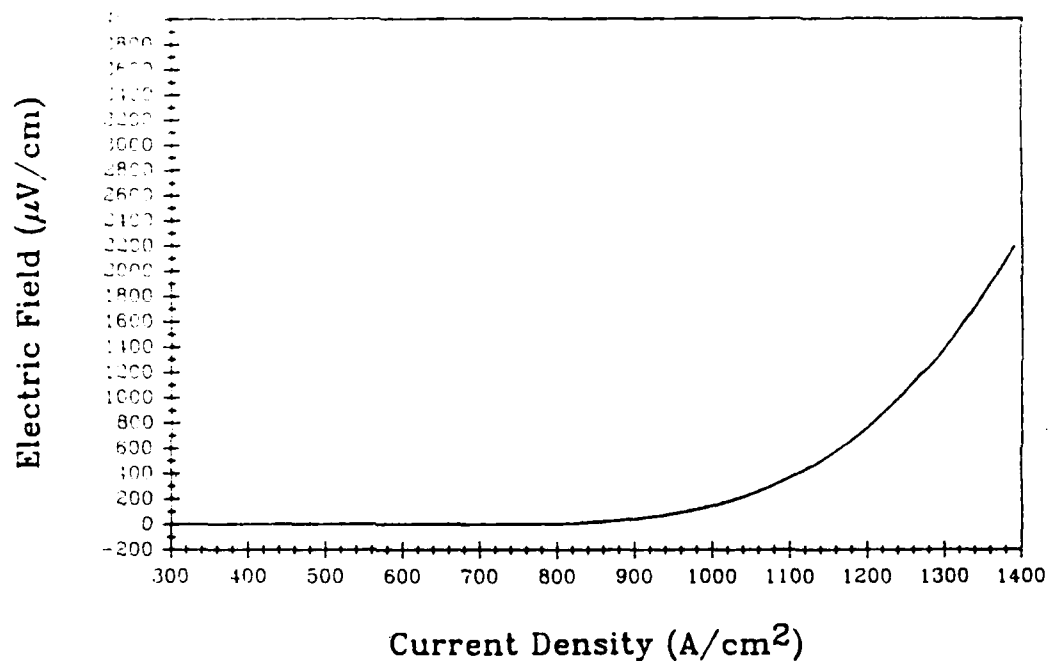
Figure 2.5.2   Electric Field versus Current Density for Filament

3306C3, A Melt Spun Fiber from Jet Milled Powder

Sintered for Six Passes At 996°C, with Re-fired Silver

Contacts
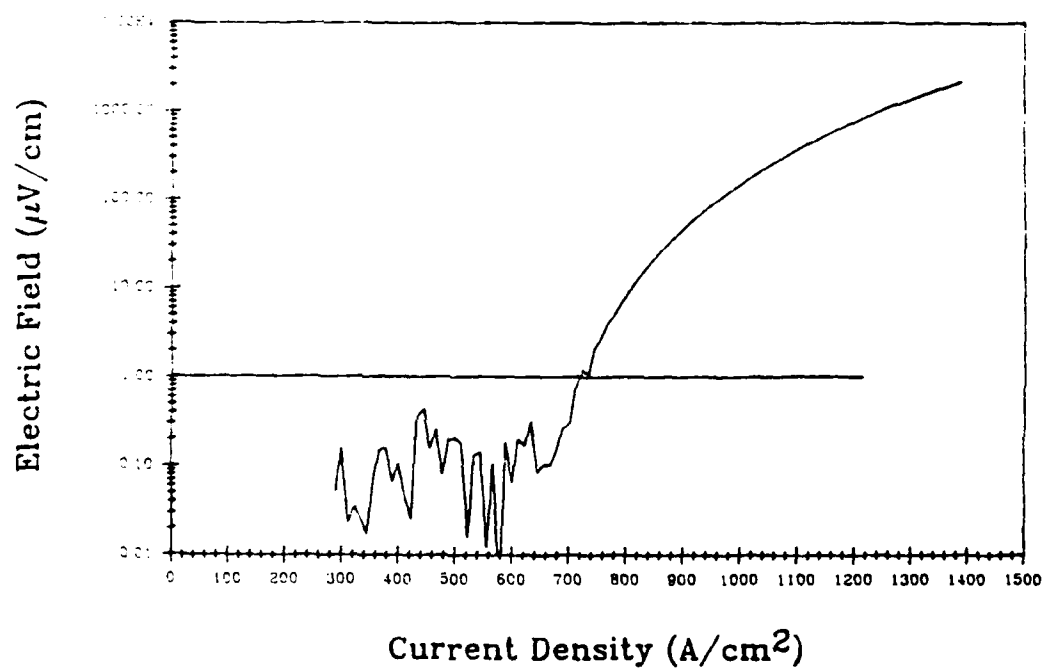
Figure 2.5.3   Semi-Logrithmic Plot of Electric Field versus Current

Density for Filament 3306C3
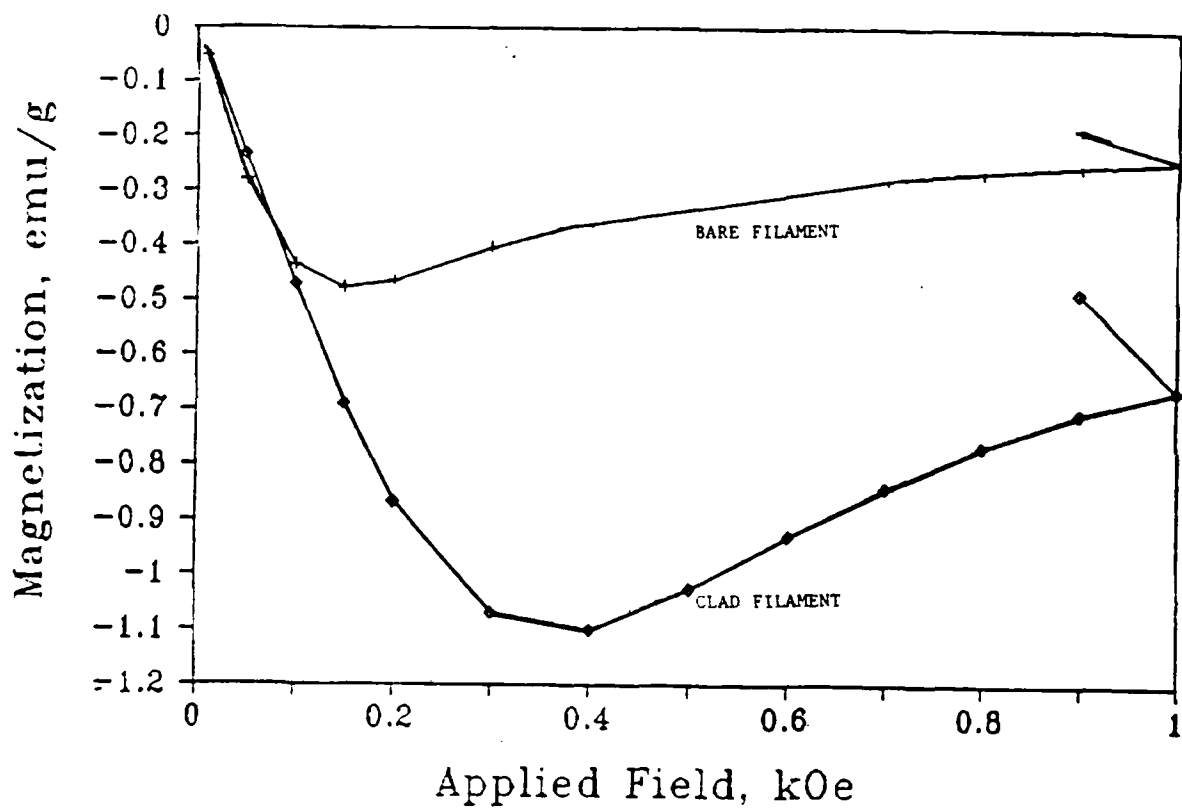
Figure 2.5.4   Magnetization at 77°K for Bare and Al-Mn Clad Filament
Produced at NIST by Stafford and Lashmore. Data
Provided by Schwartendruber

ρ (100K) $= 25.5\mu\Omega-$cm
ρ (298K) $= 39.9\mu\Omega-$cm
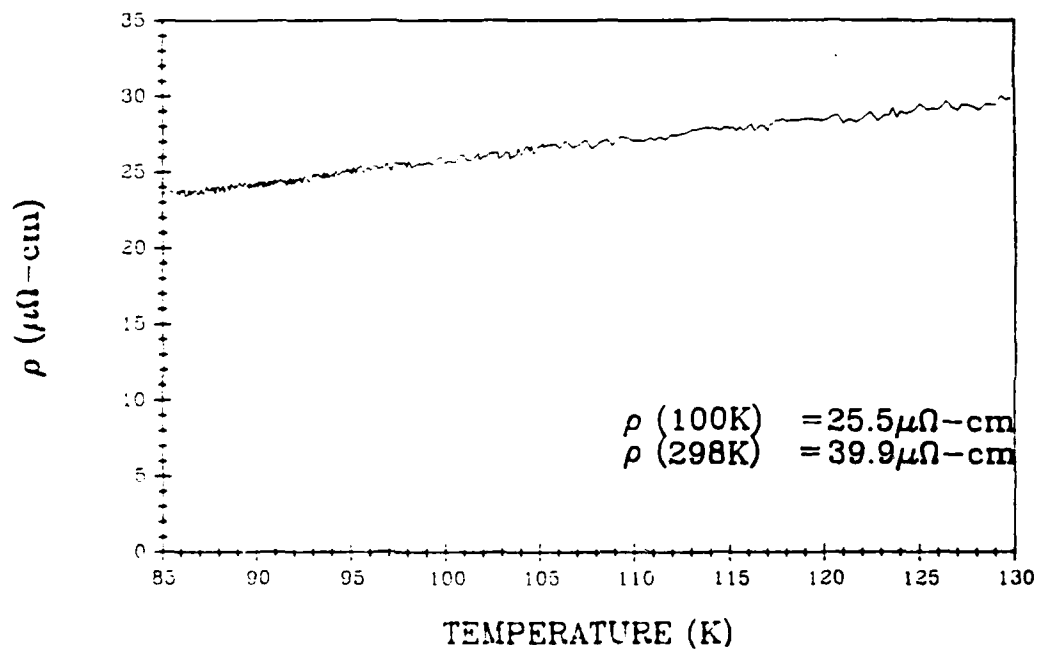
Figure 2.5.5   Resistivity versus Temperature for the Y-123 Filament

Clad with Electrodeposited Al-Mn at NIST
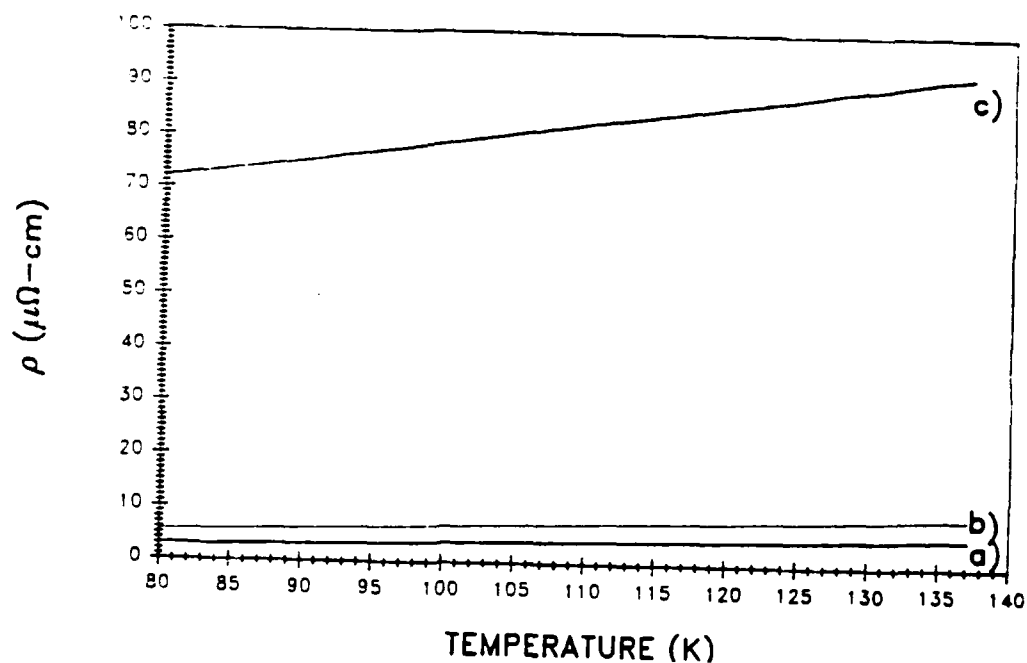
Figure 2.5.6   Resistivity versus Temperature for Y-123 Filaments with Plated Cladding for SUNY-Bufallo   a) Cu Deposited on Ag   b) Thin Ag Coating After Anneal   c) Thin Ag Coating As-Deposited
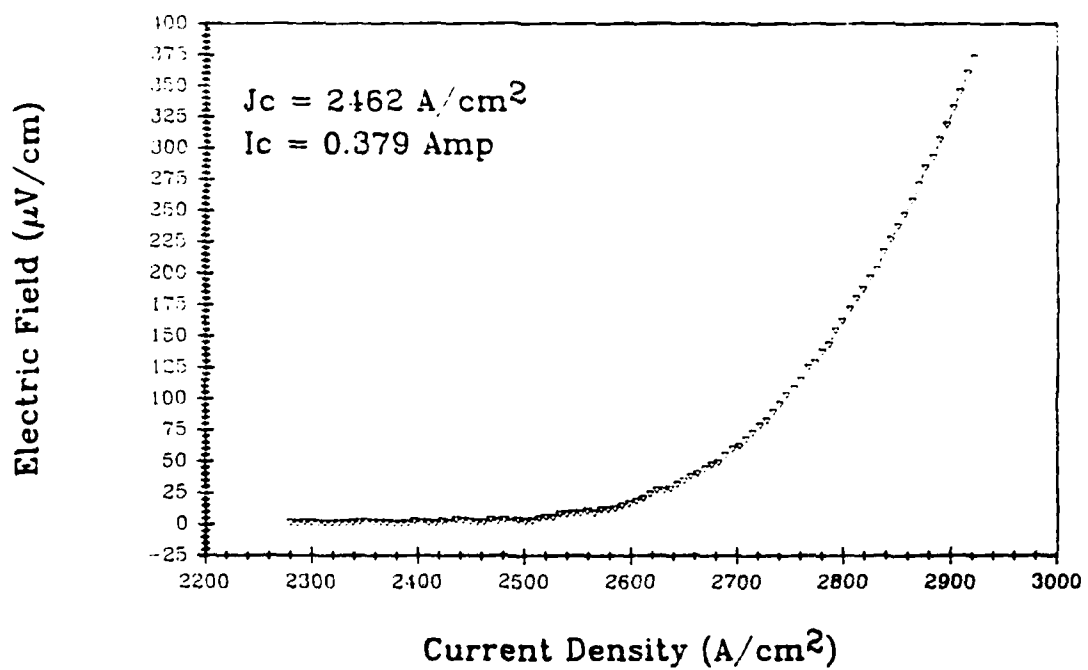
Figure 2.5.7   Electric Field versus Current Density for Filament 2760C
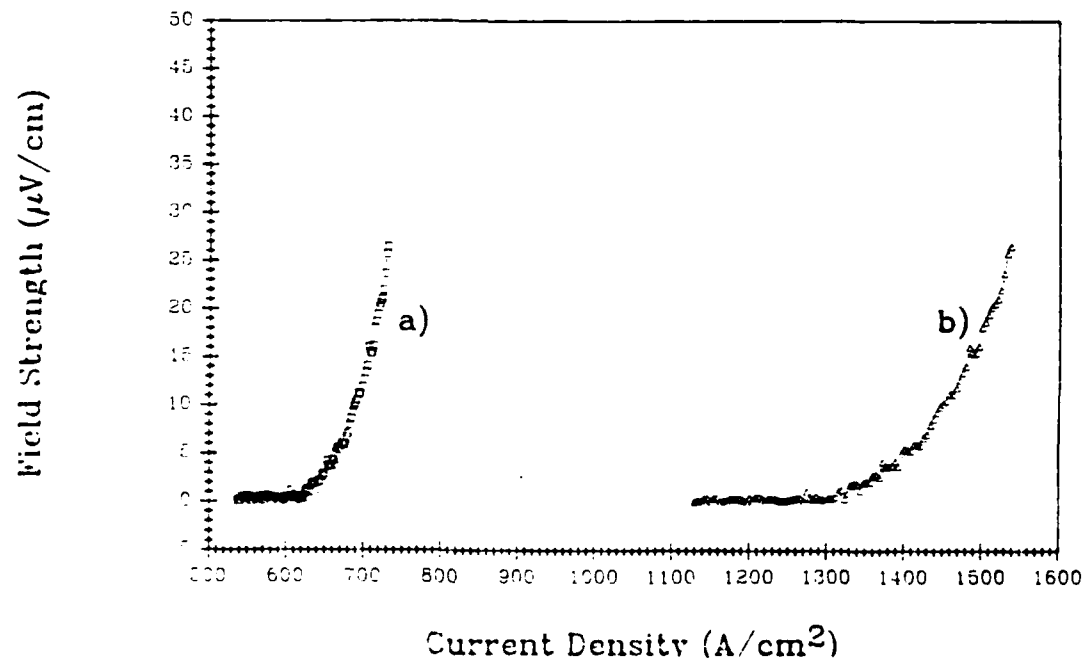
Figure 2.5.8 Electric Field versus Current Density data for Silver

Clad Filament 2793A a) Based on Total Cross Section

b) Based on Y-123 Core Cross Section
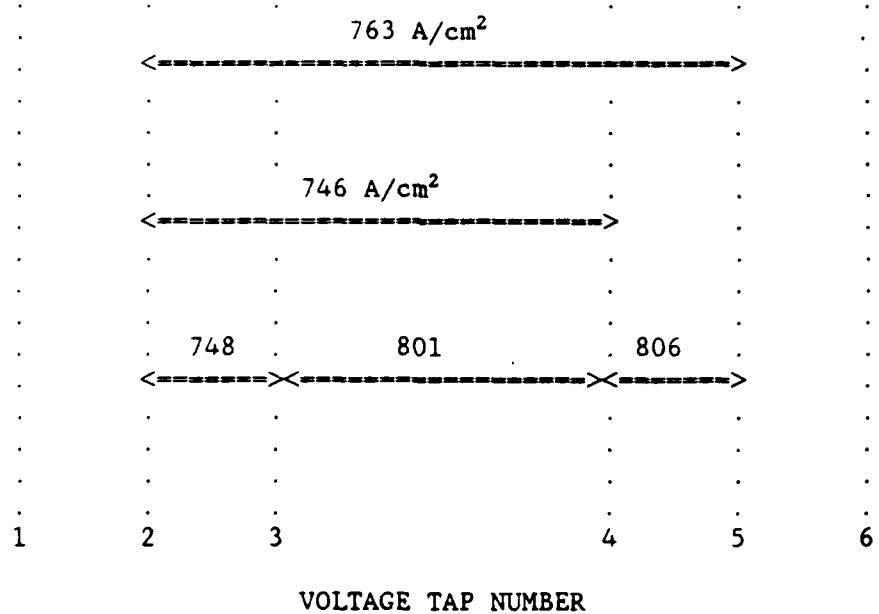
Figure 2.5.9   Critical Current Density Measured Between Multiple
                Pairs of Voltage Taps on Filament 34008A

VOLTAGE TAP NUMBER
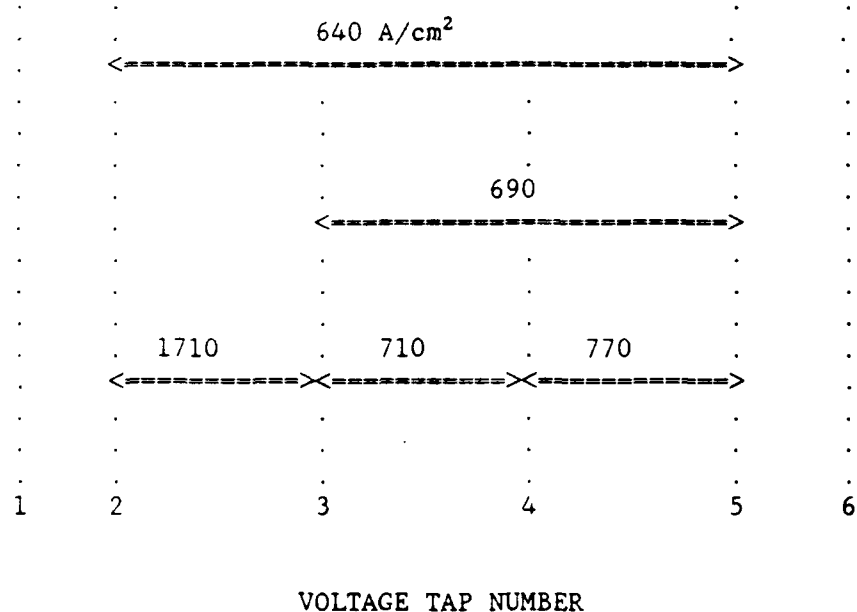
Figure 2.5.10   Critical Current Density Measured over Multiple Pairs
of Voltage Taps on Filament 34008
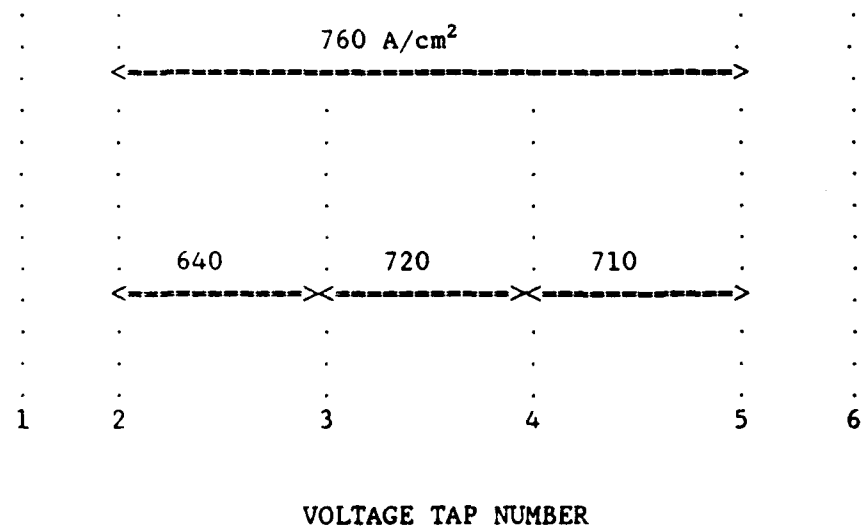
Figure 2.5.11   Critical Current Density Measured over Multiple Pairs
of Voltage Taps on Filament 3306C3
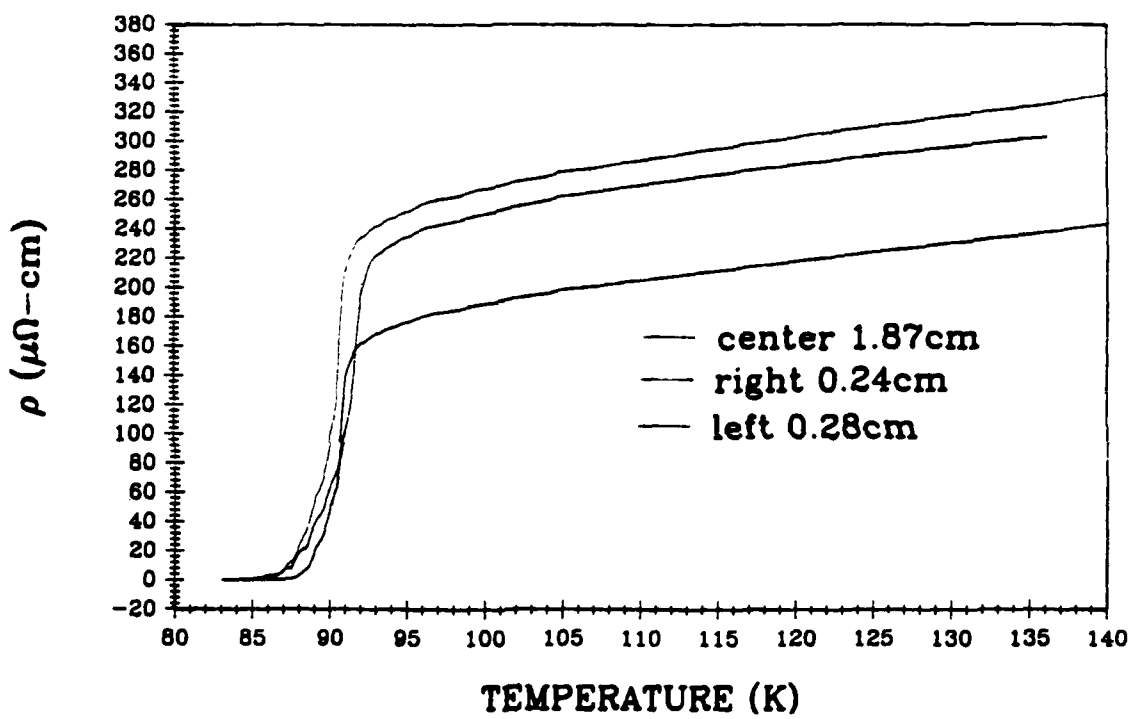
Figure 2.5.12   Resistive Transition Measured over Multiple Pairs of Voltage Taps on Filament 3306C3

2.5.6   Transmission electron microscopy of the metal/Y-123 interface

A collaborative research program between CPSS and Dr. T. E. Mitchell of Los Alamos National Laboratiory is being established to investigate metallized HTSC filaments. The thrust of the program is to examine the relationship between structure and properties of the interface. Initially the research is focussed on TEM characterization of metallized filaments already prepared by CPSS as part of the DARPA program. These include the co-fired silver clad filaments made at CPSS, and the clad filaments made by our collaborators, which we believe to have a resistive barrier at the metal/ceramic interface. Subsequent specimens will be fabricated by CPSS expressly to investigate issues raised by the results on the initial samples. We expect to eventually widen the scope to examine the mechanical and thermomechanical behavior of the clad Y-123 filaments as it relates to microstructure.

Mitchell's group at LANL will examine the CPSS specimens using analytical electron microscopy (AEM), conventional transmission electron microscopy (TEM), and if necessary high resolution electron microscopy (HREM). Emphasis is on the actual interface between the phases, to resolve features such as high resistivity or insulating phases in the metal, or degraded areas in the Y-123. LANL will determine the effect of the cladding on the micro-structure of the Y-123, including the grains, grain boundaries, twins, microcracks, and defects. With AEM, they will determine the chemical interac-tions between the metal and the cladding. They will also examine the structure of the metal, searching for defects and evidence of plastic deform-ation due to thermomechanical stresses. These microstructural results will be

related to the electrical and mechanical properties of the wire, and help define the solutions to practical problems at CPSS.

The structure of the collaborative program is a "no funds transfer" contract under the umbrella of the DOE Superconductor Pilot Center.

2.6   Summary

The Y-123 powder production has shifted entirely to a jet milled grade with improved sinterability. This powder is currently produced at a rate of about 8 kilograms/week with a reproducible particle size of 1.5-1.8 microns, with the specific surface area of 2.3-2.8 m^2/gm. This fiber was used to prepare sintered Y-123 filaments with improved critical current density.

Melt spinning process development continued, with primary emphasis on producing fine diameter green fibers with the jet milled Y-123 powder. Polypropylene and polyethylene remain the primary carrier polymers. Polymethylmethacrylate and several grades of poly(alkylene)carbonates were also evaluated. The primary focus was preparing fibers as fine as 10 microns. The finest continuous melt spun fibers produced to date have been 25-micron barium titanate fiber and 75-micron Y-123 fibers. It is preferable to achieve this diameter directly through spin draw, since cold draw techniques have caused unacceptable shrinkage during heating due to polymer relaxation.

Development was begun for a silver clad Y-123 monofilament wire produced directly by cofiring silver coated green fiber. Short pieces of prototype monofilament wire have been produced to demonstrate the feasibility. The processing steps for the new type of wire are very similar to the ribbon wire, but does not need the cladding module since the silver clad is the entire metallization.

The commercial RTC belt furnace was received and, after considerable de-bugging, brought into operation. Several modifications are underway to make it suitable for continuous sintering of Y-123 fiber, and continuous fiber sintering experiments are underway. These have identified the need for better control of polymer relaxation and binder burnout. Zone sintering experience from the tube furnace is being correlated with the belt furnace results. The prototype cladding module design was completed and components are now being fabricated. The solder clad copper strips were received and bonded in a prototype reflow unit.

The major efforts in characterization were to determine resistive transition and self field critical current for sintered bare and Ag-clad fibers. A refired silver contact method was developed for making reliable electrodes. There has been an improvement in 77°K (self-field) critical current density of Y-123 filaments, up to 2400 A/cm^2 for the best filament, with 1500 A/cm^2 for a typical filament. Similar results are seen for silver clad filaments. This increase is attributed to improved Y-123 powder. Preliminary data suggests an important effect of specimen length on transport critical current of thin filaments of weak-linked specimens. Measurements over different segments of the same filament show that T_c and J_c vary along the length of the filaments.

A collaborative research program has been started with Los Alamos National Laboratory, aimed at characterizing the interface between the Y-123 and the cladding. This will correlate the structure of the interface to the properties and processing of the metallized wire.

SECTION 3

HIGH TEMPERATURE SUPERCONDUCTOR

MOTOR DESIGN AND FABRICATION

ALAN CRAPO AND JERRY LLOYD

EMERSON MOTOR COMPANY

MOHAMED HILAL

UNIVERSITY OF WISCONSIN

3.1   MANPOWER

In the last quarterly report, we stated that our new motor design engineer, Alan Crapo, was scheduled to start on February 6, 1989. He started as scheduled, and has been spending 100 percent of his time on the superconductor motor program.

Instead of hiring a full time mechanical engineer for the program, we feel we can better utilize our available resources by contracting with consultants for some of the expertise in cryogenics and bearing systems and hire a competent technician to work in the lab. Alan Crapo will coordinate the work with consultants and technician support.

3.2   LITERATURE RESEARCH

The detailed literature search on superconducting motors and mechanical systems has been under way in three areas and will continue in the second and third areas.

1. A graduate student at the University of Wisconsin-Madison put together a list of papers and articles from the university library on superconducting related topics. We then selected from the abstracts, the 28 papers we felt would be helpful. We received copies of the 24 papers that were available at the University of Wisconsin.

2. A patent search identified 63 patents relevant to superconducting motors. We are continuing to review and study these patents.

3. Computer data base search work was started at Emerson. We will continue to search for relevant papers and articles and obtain copies from universities.

3.3   APPLICATION STUDY

Work continued in evaluating different motor configurations for their potential as candidates for using HTSC wire. A homopolar motor was designed and analyzed. The results are reported. A DC heteropolar motor with a superconducting field winding was investigated. The results are reported. We have also investigated using the Meissner effect with bulk superconducting material in an AC reluctance motor for improved performance. The results of this investigation are also reported. The fourth motor under investigation at this time is an induction motor that uses superconducting wire in the stator.

3.3.1   Homopolar Motor

In the previous quarterly report, the homopolar motor was discussed as the only electric motor without time varying magnetic fields. This "true DC" machine, first built by Michael Faraday in 1831, in its simplest disc form consists of a disc of electrically conducting material in a magnetic field parallel to the axis of rotation (figure 3.3.1.1). Torque is produced by
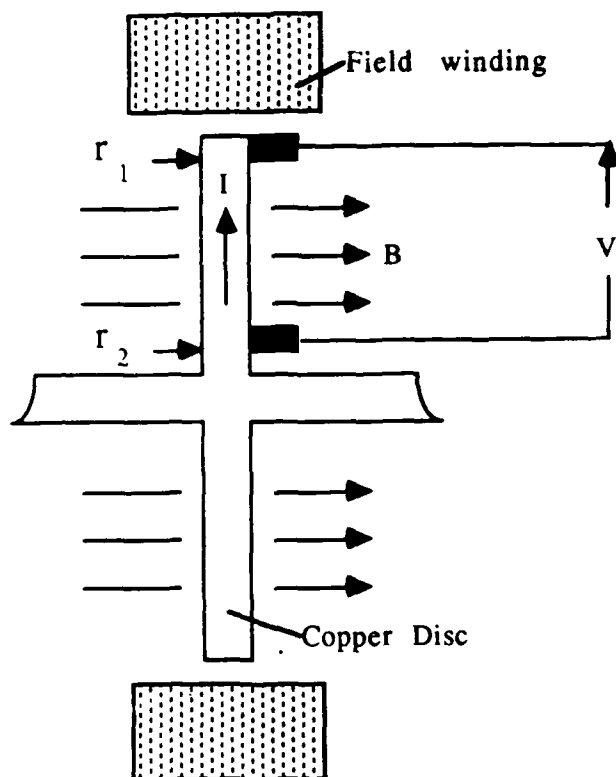
Figure 3.3.1.1   Side view of homopolar disc motor.
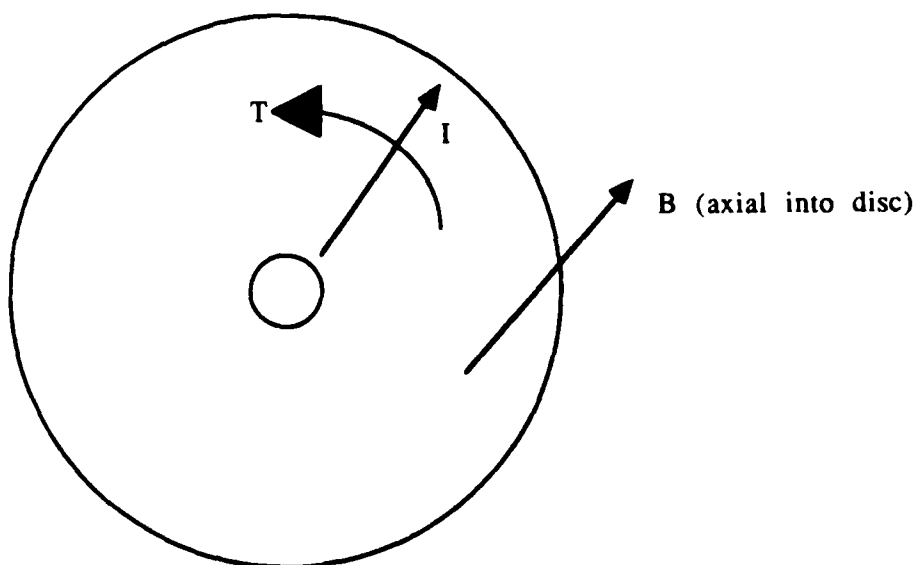
Figure 3.3.1.2   Axial view of disc.

current in the radial direction within the disc as shown in figure 3.3.1.2 and can be calculated per Fleming's rule.

$$T = B \times I \cdot (r_2 - r_1) \cdot (r_2 + r_1)/2 - \text{friction}$$

Where: T is the torque

B is the flux density

I is the current in the disc

r_1 is the radius of the inner current collector

r_2 is the radius of the outer current collector

(r_2-r_1) is the conductor length

$(r_2+r_1)/2$ is the effective mean disc radius

The back EMF is determined by the flux between current collectors and the speed.

$$V_{\text{Back EMF}} = N \, d\phi/dt$$

Where N = 1 turn for a single disc motor

$$V_{\text{Back EMF}} = \phi \cdot \text{RPM}/60$$

$$V_{\text{Back EMF}} = B \cdot \pi (r_2^2 - r_1^2) \cdot \text{RPM}/60$$

Motor terminal voltage = $V_{\text{Back EMF}}$ - IR drop

The design goal for this potential HTSC motor application is as follows:

B = 3 Tesla (DC Field)

$J_c = 10^5$ A/cm^2

Output = 10 Hp @ 1800 RPM

The three Tesla DC field is to be produced by a superconducting field coil wound by HTSC wire.

For the sake of simplicity on the first level of design, the following assumptions have been made:

a. no friction.

b. no copper loss and no voltage drops in the current collectors,

c. The inner current collector radius (r_1) is ten percent of the outer current collector radius (r_2).

The torque to produce ten horsepower at 1800 RPM is 39.6 N.m. from the torque equation, the required current is a function of the rotor radius.

$$39.6 \text{ N·m} = 3 \text{ Tesla} \times I·(r_2 - .1r_2) · (r_2 + .1r_2)/2$$

or $I = 26.667/r_2^2$

From the voltage, equation, the back EMF is a function of the rotor radius.

$$V = 3 \text{ Tesla} · \pi · (r_2^2 - (.1r_2)^2) · \text{RPM}/60$$

or $V = 279.9r_2^2$

The current and voltage are plotted versus rotor radius in figure 3.3.1.3 a and 3.3.1.3 b.

The homopolar motor tends to have very high current and low voltage. This is due to the armature being essentially one turn. The way to get higher voltage is with more flux. For a given flux density, this means a larger rotor.

Thus, a homopolar disc motor with a rotor diameter of one meter or 39 inches would have a voltage of 70 Volts and a current of 107 Amperes. A smaller rotor of 0.5 meter diameter or 19.7 inches would have a voltage of 17.5 Volts and a current of 427 Amperes.

Another way to increase voltage and reduce current is to have multiple discs connected in series as shown in figure 3.3.1.4.

For four discs in series, the torque equation then gives the relationship between the current and the rotor radius as

1 DISC HOMOPOLAR MOTOR
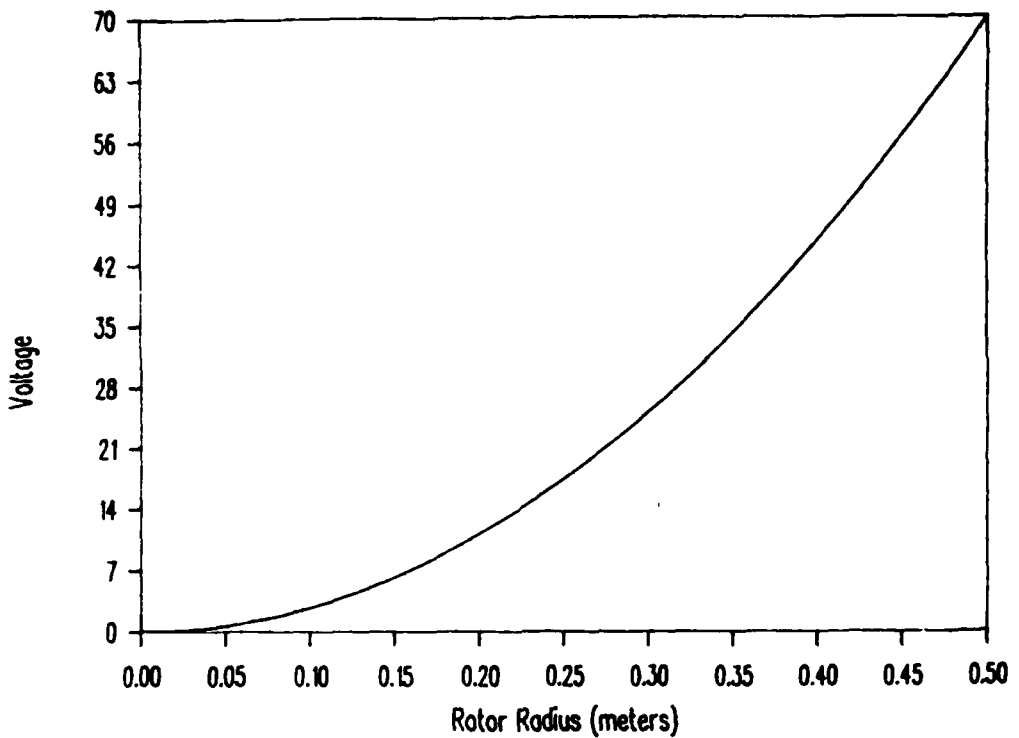

Figure 3.3.1.3a Volts vs Rotor Radius
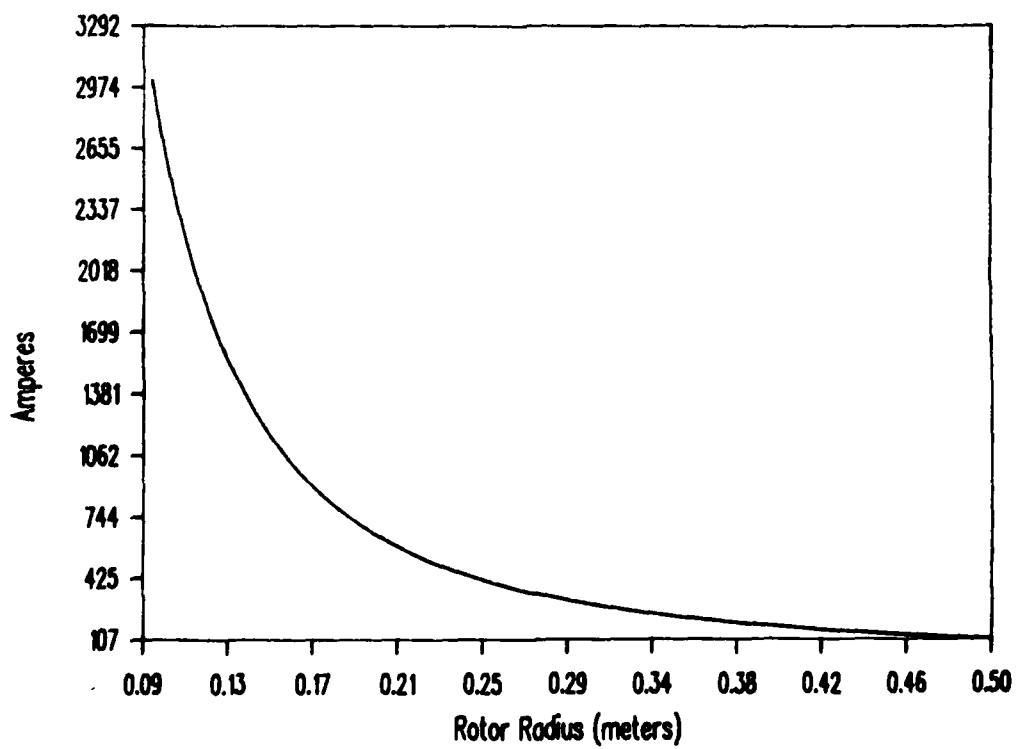

Figure 3.3.1.3b Amps vs. Rotor Radius
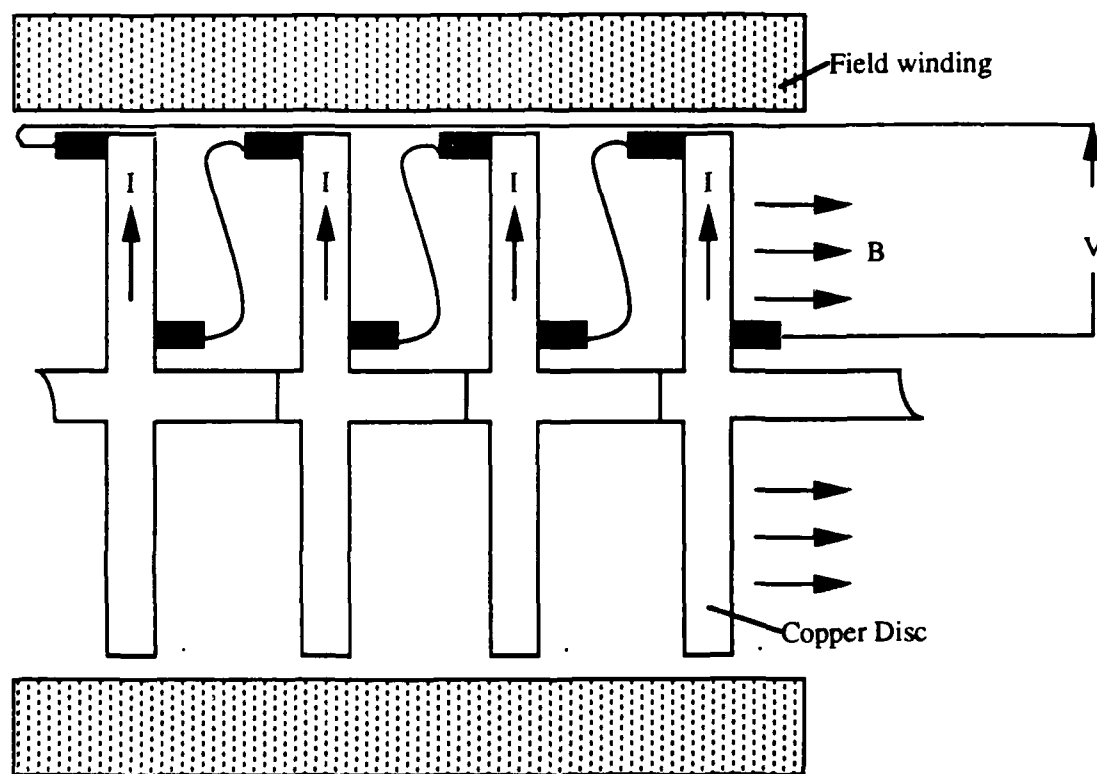
Figure 3.3.1.4   Homopolar motor with 4 discs in series

4 DISC HOMOPOLAR MOTOR
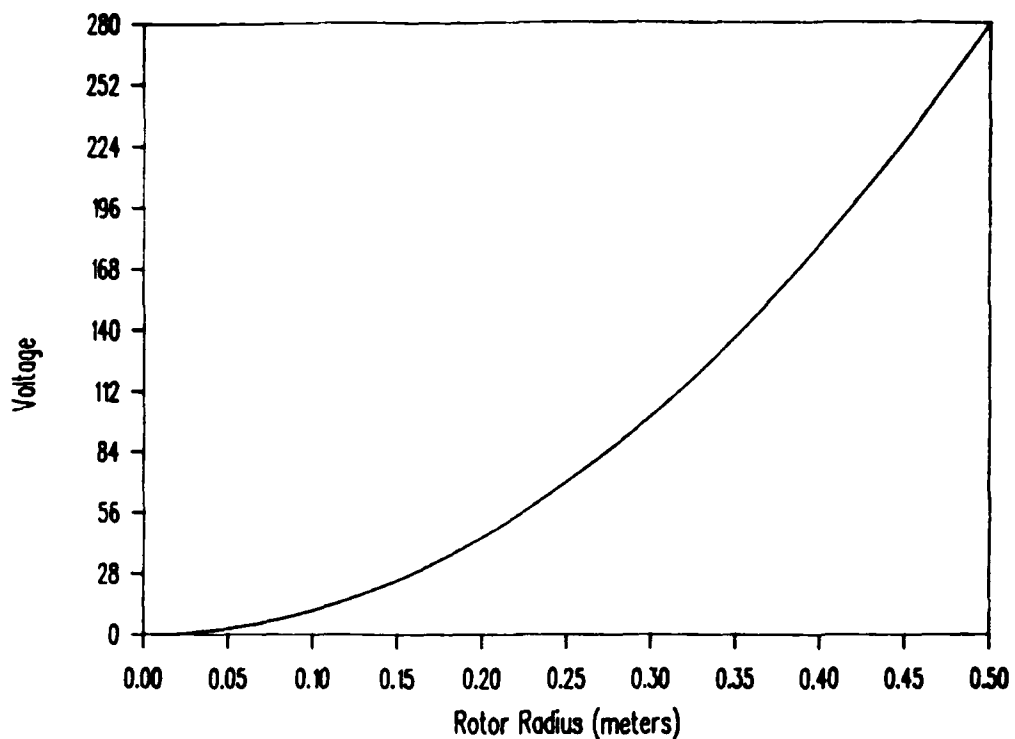
Figure 3.3.1.5a Volts vs Rotor Radius
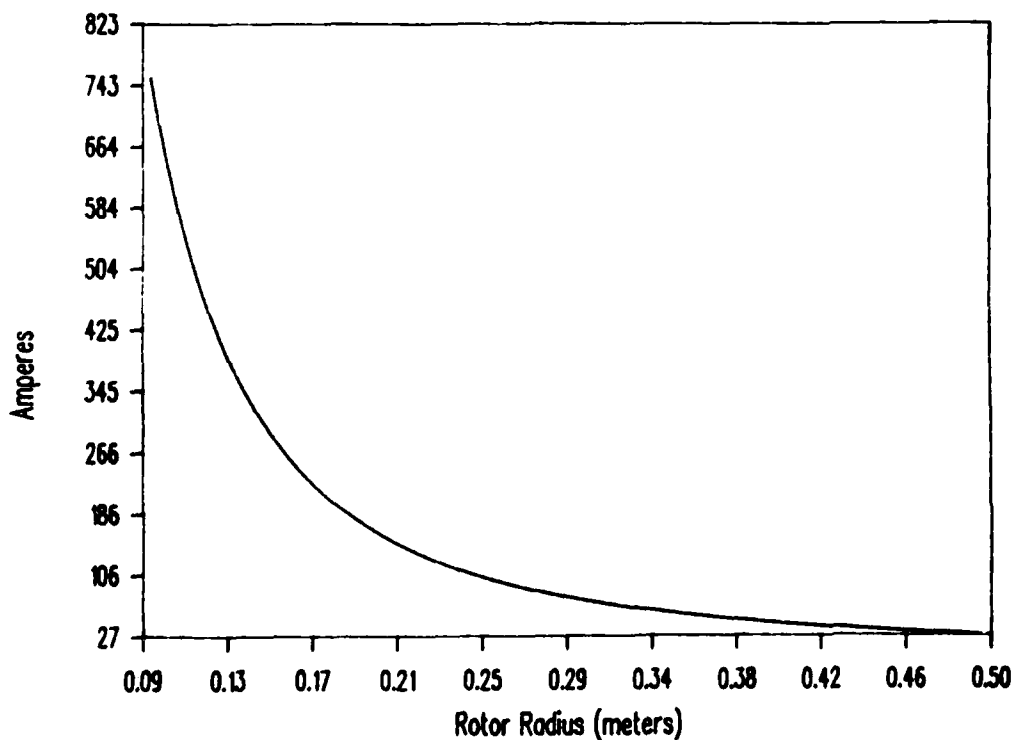
Figure 3.3.1.5b Amps vs. Rotor Radius

$$I = 6.666/r_2{}^2$$

and the voltage equation for four discs becomes

$$V = 1120 \ r_2{}^2.$$

The current and voltage for the four disc versions are plotted versus rotor radius in figure 3.3.1.5 a and 3.3.1.5 b. A 0.5 meter (19.7 inch) diameter armature operates at 70 Volts and 107 Amperes. A 0.1 meter (3.9 inch) diameter armature operates at 2.8 Volts and 2675 Amperes. The application and power source would determine the voltage and current desired.

A typical 10 horsepower, 1800 RPM industrial DC motor has an armature diameter of .13 meters (5.25 inches) and an active length of .14 meters (5.5 inches). A four disc homopolar motor with a rotor diameter of .13 meters or 5.25 inches would require 5.0 volts and 1500 Amperes. 5 Volt operation is typical of this size and larger homopolar motors.

The superconducting field winding for this motor would be wound in layers on a round bobbin. This type of winding has the least amount of stress on the fragile ceramic fibers.

For applications where low voltage and high current are available, the homopolar approach would be the best approach. For applications where only high voltage and low current are available, the homopolar design gets too large to be practical. We will continue work next quarter to look at the homopolar designs which will work well with the HTSC wire that will be available in the near future.

3.3.2   DC Heteropolar Machines

In the previous quarterly report, we started the analysis of a DC heteropolar machine. The power to size ratio of the armature is improved by increasing the flux density in the air gap form 0.75 Tesla to 3.0 Tesla (four

times the flux density). This allows the armature diameter to be reduced to one half diameter and half of the armature windings to be eliminated.

For initial consideration, we have referenced a conventional ten horsepower 1800 RPM DC brush type motor. The standard motor has the following basic characteristics.

Rotor Diameter = .133m (5.25 inches)

Active Length = .140m (5.5 inches)

Outside Diameter = .260m (10.25 inches)

Rated Voltage and Current:

Armature: 240 Volts and 38 Amperes

Field: 150 Volts and 2.1 Amperes

For the superconducting field version of this motor, we reduce the armature to one half the conventional diameter and replace the iron with a light weight non-magnetic material.

The field coil design and analysis was done using a finite element model. A plot of the flux lines for 1/4 of a machine is shown in figure 3.3.2.1. The field coil of 160,000 Amperes turns per pole produces a radial flux density of over three Tesla on the surface of the armature. The armature surface flux density in the radial direction is plotted versus angle in figure 3.3.2.2.

With a field current of 2.1 Amperes, 76190 turns of conductor are required to produce 160,000 ampere turns. This high concentration of flux to produce the three Tesla field in the gap also has a lot of leakage flux. On figure 3.3.2.1, the outer diameter of the conventional motor is drawn. The density of the leakage flux at this diameter is as high as 0.4 Tesla. If controlling leakage flux is important for a given application, a steel shell

0.4 TESLA
FIELD AT
.260m DIAMETER

.260m (10.25 INCH)
DIAMETER OF CONVENTIONAL
MOTOR
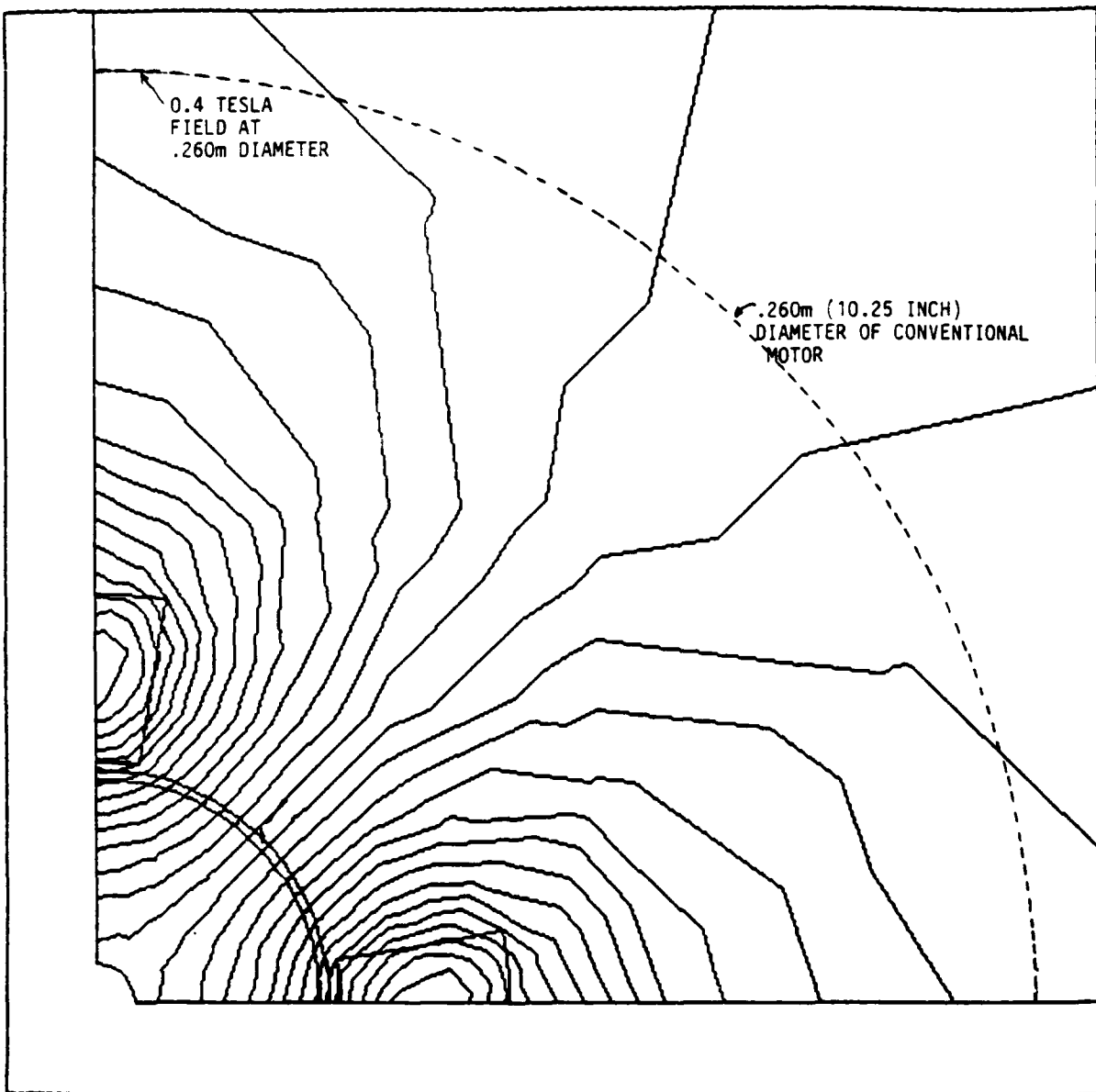
FIGURE 3.3.2.1.   FLUX PLOT OF SUPERCONDUCTING
FIELD FOR 1/4 DC HETEROPOLAR MOTOR
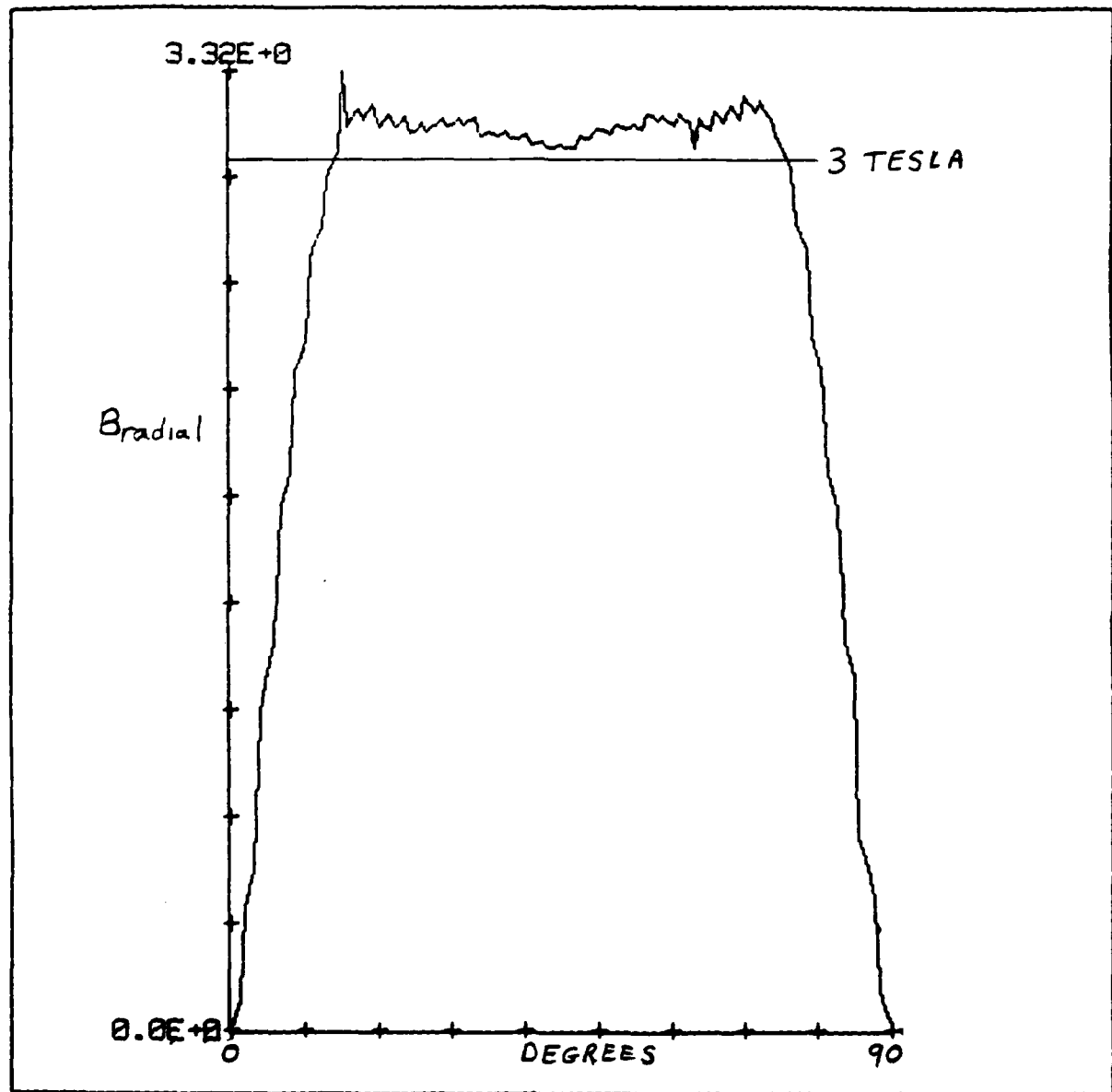
FIGURE 3.3.2.2.   RADIAL FLUX DENSITY ON THE
SURFACE OF THE ARMATURE

can be used to reduce the leakage. Once leakage is taken into account, the size of this motor will be about the same size as the conventional motor.

The advantage will come in the weight reduction that comes with eliminating the steel.

Getting rid of the steel does not come for free. The permeability of the steel is several thousand times greater then air. With no steel, very high Ampere turns are required to drive the flux through an all air path. The high number of turns requires very small conductors.

The conductor will be made up of multiple strands of superconducting ceramic fibers encased in copper to form a ribbon. With about 2.5 times as much copper as superconducting fibers, and packing factor of 70 percent of the wound coil, the superconductive material takes up about 20 percent of the total coil cross section. The field coil displayed in figure 3.3.2.1 requires a coil current density of 90,000 ampere/cm^2. This requires a current density of 450,000 Amperes/cm^2 in the superconducting ceramic fibers. This is even higher than our goal of 100,000 Amperes/cm^2. The lower current density will require a larger motor.

The conventional motor runs with a current density of 500 to 600 Amperes/cm^2 in copper at room temperature. In order to eliminate the iron from the motor, we need to increase the current density to 450,000 Amperes/cm^2. This is an increase of 800 to 900 times the conventional copper current density. By eliminating the steel, we have increased the flux path reluctance by almost one thousand times. The net result is no improvement in power per unit volume, but there is still a weight savings.

In order to make this type of superconducting field winding really useful in this size motor, current densities in the 1,000,000 Amperes/cm^2 range will be necessary.

The next step for this motor is to look at other sizes, to see what sizes are practical applications of DC heteropolar fields wound with superconducting ceramic fiber wire.

3.3.3   Reluctance Motor

The torque in a reluctance motor is produced when the flux changes with rotor position. The rotor likes to sit in the maximum flux position. Torque must be applied to move the rotor from this position, and the motor will produce a torque to get back to the maximum flux position. The maximum torque position is where the rate of change of flux with respect to angular position is maximum. A really good reluctance motor has a large change in flux from the maximum flux position (direct axis - figure 3.3.3.1) to the minimum flux position (quadrature axis - figure 3.3.3.2).

The Meissner effect does not allow magnetic fields to penetrate superconducting materials. Since a reluctance motor peak torque is increased by reducing the quadrature axis flux, superconducting material used as a flux block on the rotor will give us more torque. Figure 3.3.3.3 shows the direct axis flux with superconducting material between rotor poles and figure 3.3.3.4 shows the quadrature axis flux with superconducting material blocking the flux.

The peak torque position where the rate of change of flux versus angle is at a maximum, is shown in figure 3.3.3.5 for the conventional rotor and figure 3.3.3.6 shows the same position with superconducting material as a flux block.
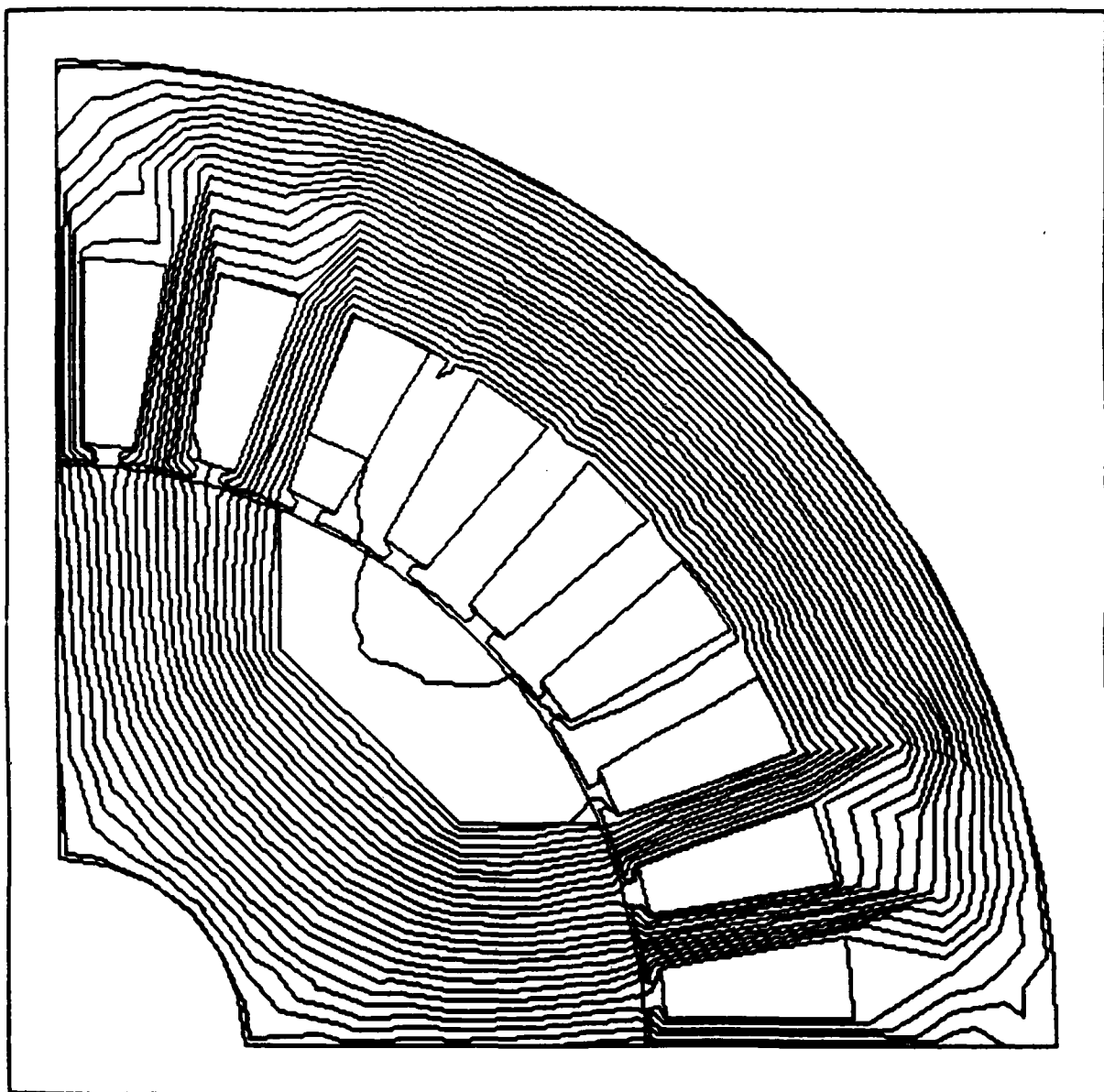
FIGURE 3.3.3.1.   DIRECT AXIS FLUX WITH CONVENTIONAL ROTOR
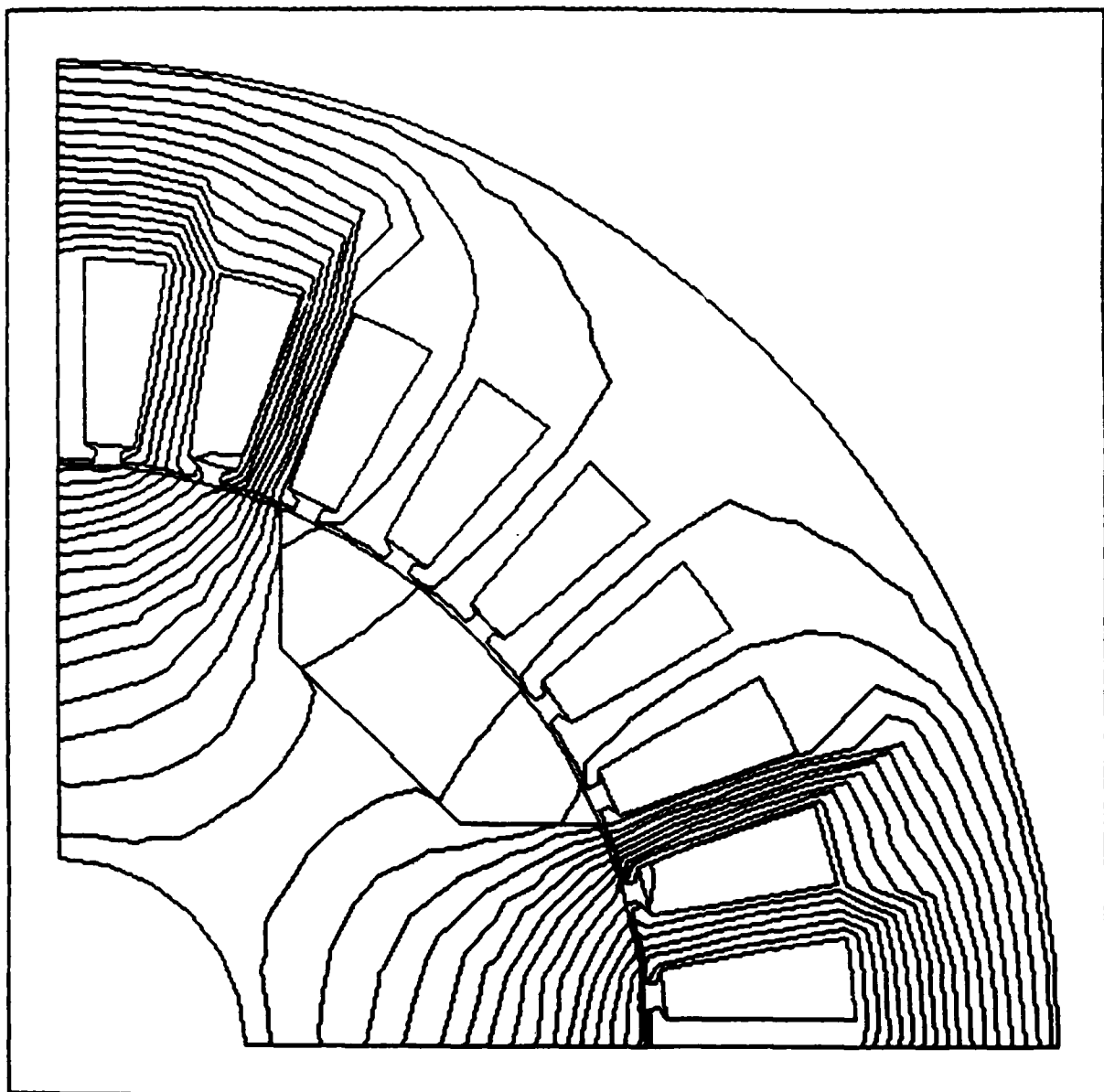
FIGURE 3.3.3.2. QUADRATURE AXIS FLUX WITH CONVENTIONAL ROTOR
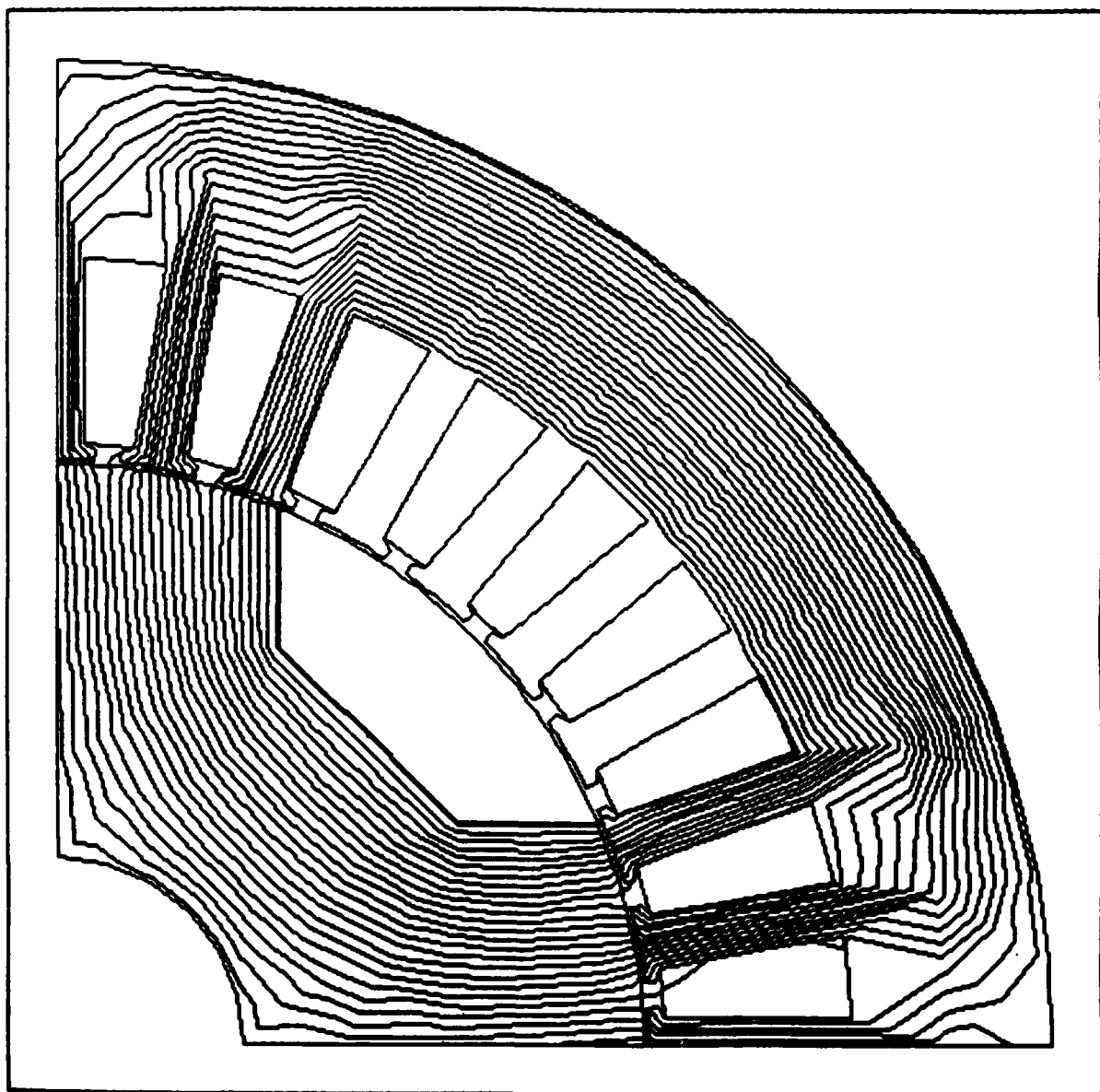
FIGURE 3.3.3.3.   DIRECT AXIS FLUX WITH SUPERCONDUCTING MATERIAL ON ROTOR
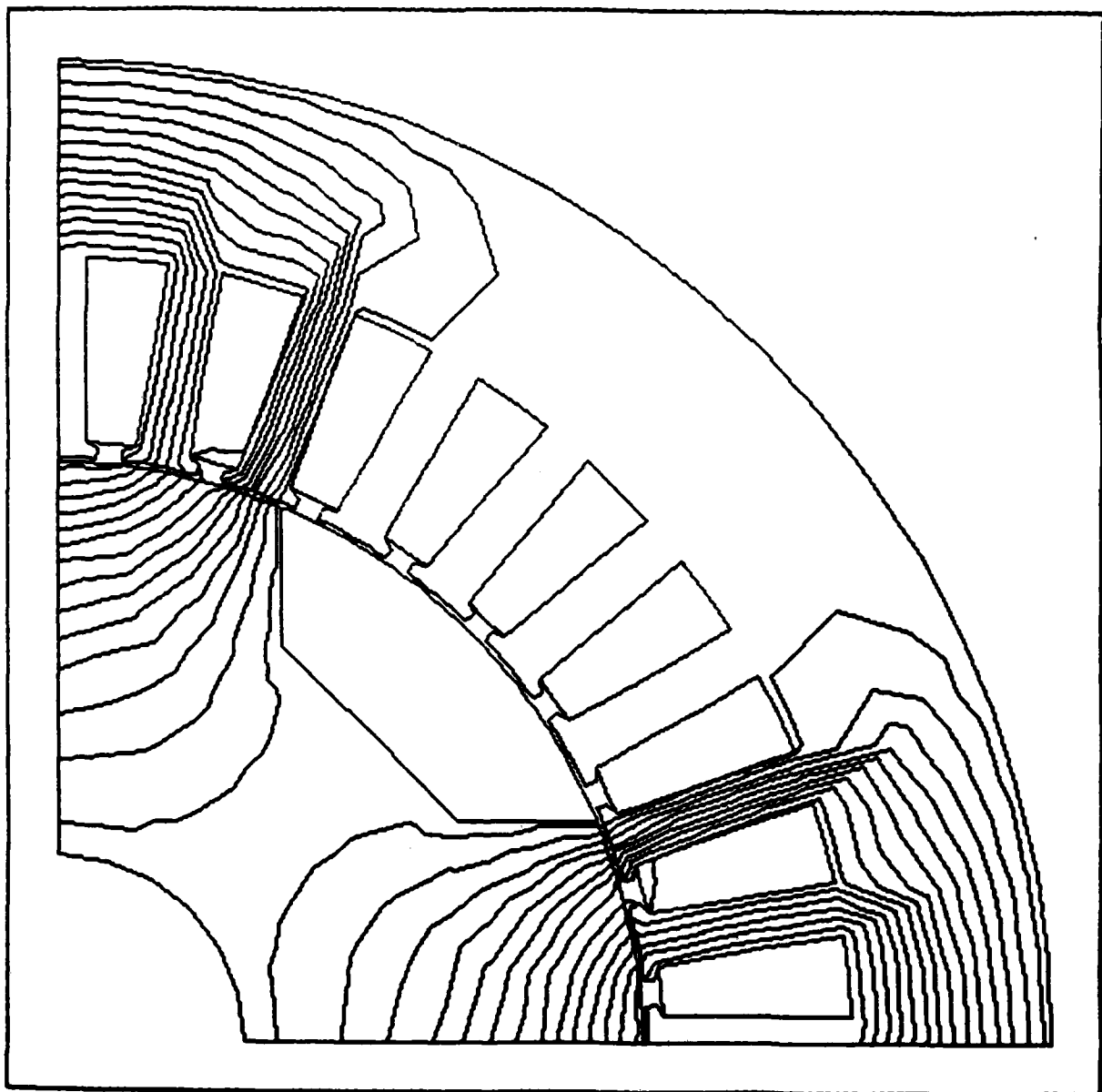
FIGURE 3.3.3.4. QUADRATURE AXIS FLUX WITH SUPERCONDUCTING MATERIAL ON ROTOR
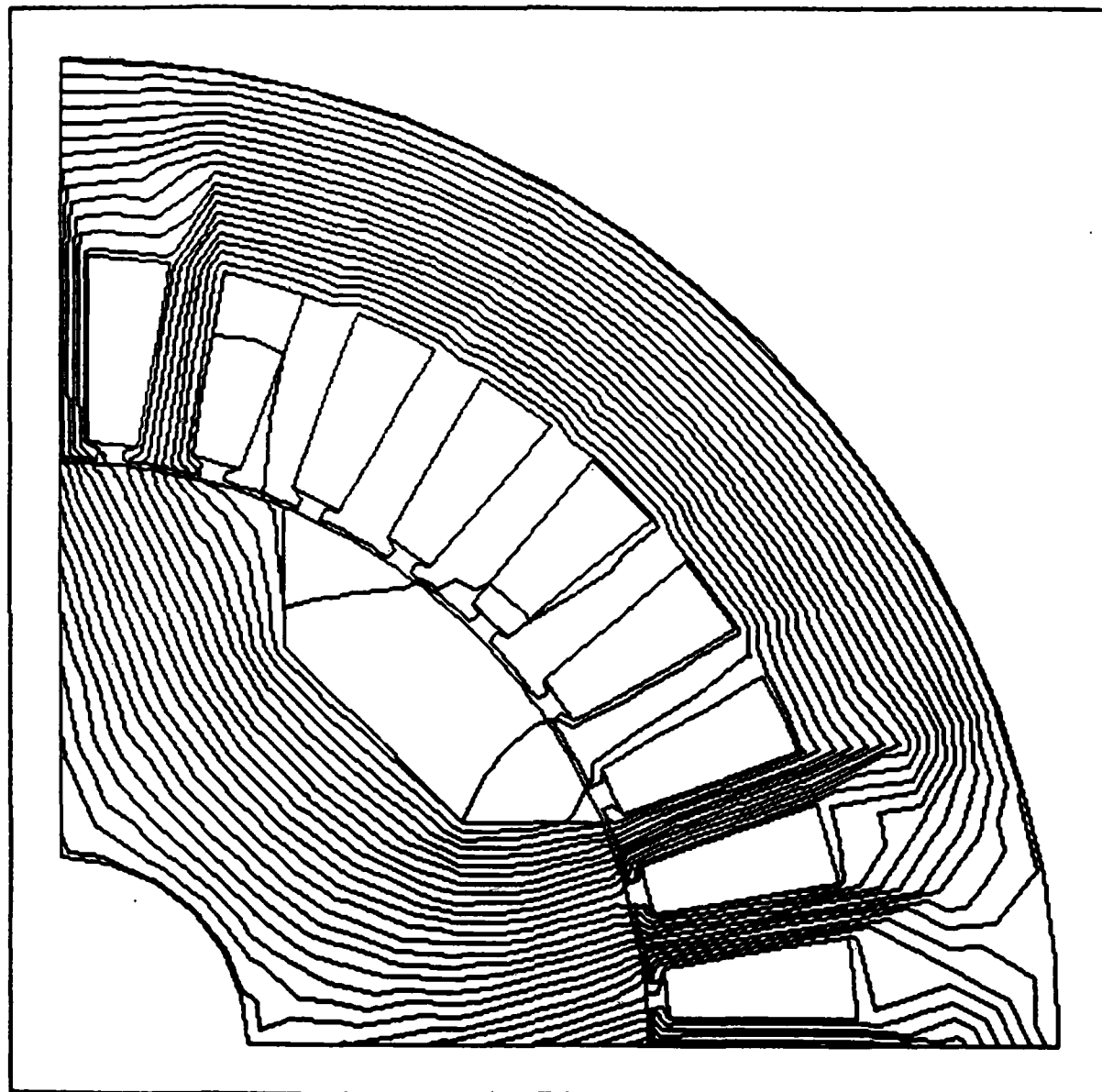
FIGURE 3.3.3.5. PEAK TORQUE POSITION WITH CONVENTIONAL ROTOR
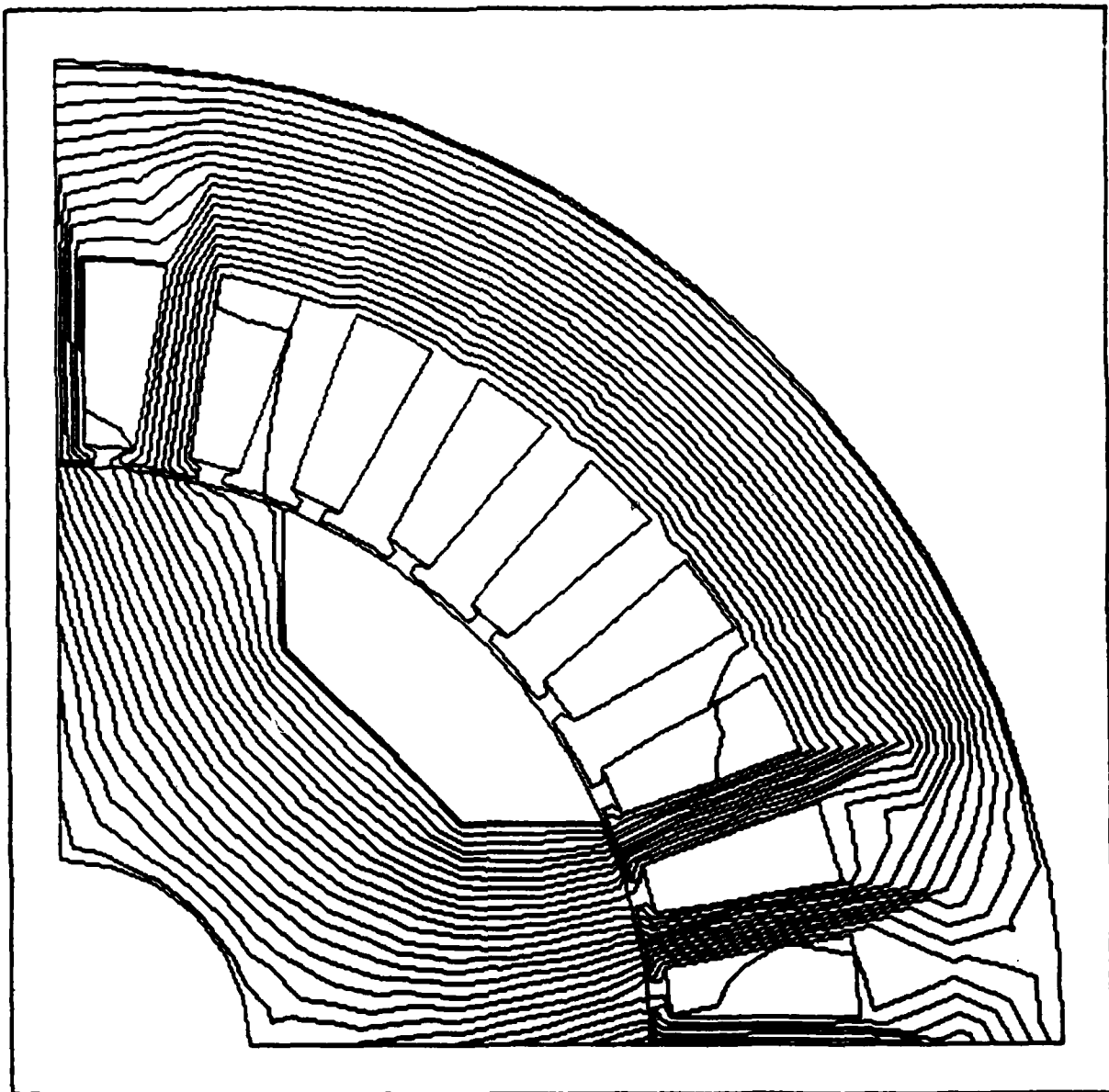
FIGURE 3.3.3.6.   PEAK TORQUE POSITION WITH SUPERCONDUCTING MATERIAL ON ROTOR

In terms of flux, turns and current, a first order approximation of the peak torque is:

$$T_p = 1/2 \; N \cdot I \cdot (\phi d - \phi q)$$

Where T_p = peak torque

N = effective stator turns

I = stator current

ϕd = direct axis flux

ϕq = quadrature axis flux

Finite element modeling gives us the flux produced by the stator winding per meter of axial length.

Direct axis flux with SC flux block rotor = 1.904×10^{-2} wb/m

Quadrature axis flux with SC flux block rotor = 1.089×10^{-2} wb/m

Direct axis flux with conventional rotor = 1.986×10^{-2} wb/m

Quadrature axis flux with conventional rotor = 1.243×10^{-2} wb/m

From the torque equation, we can see that the maximum torque motor has very low quadrature flux. Even with the superconducting flux block, the quadrature axis flux is greater than 50 percent of the direct axis flux. $\phi d - \phi q$ is 8.15×10^{-3} wb/m length for the superconducting case and 7.43×10^{-3} wb/m length in the conventional rotor. This is a 9.7 percent improvement in torque.

A gain of less than ten percent on a motor that is inherently a low efficiency motor to start with is not a very good use of superconducting technology. We will not pursue this motor concept any further, but will focus on other motor concepts.

3.3.4   Induction Motor with Superconducting Stator Windings

Our fourth application, being the easiest, to build and test is a good candidate for our first proof of principle motor. There are two main advantages for taking a conventional cryogenic induction motor and replacing the standard windings with superconducting wire. The first advantage is that the motor should show improvement over the conventional motor as long as the superconducting wire can carry a current density greater than copper. We can build a motor before our goal of 100,000 Amperes/cm^2 is reached. The second main advantage to this motor is that we already make rotors and stators for conventional cryogenic induction motors designed to run in liquid nitrogen at U.S. Electrical Motors.

U.S. Electrical Motors (USEM) is a division of Emerson Motor Company that makes medium and large sized induction motors. One of USEM's products is a line of motors marketed under the genetic heading of "Cryogenics". These motors are designed to operate submerged in a liquified gas with the gas flowing over, around, and through the winding. The extreme cold and thermal transfer properties of these liquified gases are used to minimize temperature rise in both the stator and rotor; thus allowing a design which approaches the theoretical maximum H.P. limits for a given frame size and stack length.

The term "cryogenic" normally is used to designate an operating temperature of -160 centigrade or colder. In practice, USEM uses the term to refer to any motor, totally submerged in any liquid gas, which uses that gas as a primary cooling medium. We have designed and manufactured motors for fluids as warm as JP-4 jet fuel at +27°C and as cold as liquid neon at -246°C.

While the basic electrical design concepts are the same on cryogenic motors as on air motors, some specific items are unique. One of the major differences is the special care given to the insulation for cryogenic

applications. With thermal cycling between room temperature and cryogenic temperatures, there is a great deal of expansion and contraction. The windings are protected from abrasion and also given extra strength to maintain integrity over a long life.

As mentioned earlier, copper at room temperature can carry about 500 Amperes/cm^2 under normal conditions. At 77°K, the same copper can carry up to 1500 Amperes/cm^2 without a problem. This means that at least 1500 Amperes/cm^2 is needed in the superconducting ceramic fibers to be an improvement over copper. Our goal of 100,000 Amperes/cm^2 in the ceramic fibers gives us an effective conductor current density of 28,600 Amperes/cm^2. This is 19 times better than conventional copper windings.

Our initial studies are on a motor with the following characteristics:

> 3 horsepower
>
> 1788 RPM
>
> 480 Volts
>
> 4.6 Amperes Full Load Current
>
> 38 Amperes Locked Rotor Current
>
> .161m (6.32 inch) Stator Diameter
>
> .095m (3.75 inch) Rotor Diameter
>
> .083m (3.25 inch) Active Length

Further analysis and detailed designs will be done in the next quarter.

3.3.5   Application Summary

The homopolar motor is a good candidate for a proof of principle motor for applications where high current and low voltage are available. The

absence of AC fields makes it easier to analyze than the other applications. The round bobbin wound field is the easiest winding to do with fragile wire limited to large bending radii.

The DC heteropolar is best used for applications with high voltage and low current. When superconductive current densities exceeding 500,000 Amperes/cm^2 are available, the superconducting version of this motor will be an advantage. We will investigate other motor sizes where practical current densities can produce useful superconducting motors.

The reluctance motor can be improved by using the Meissner effect of superconducting material to block flux from penetrating certain parts of the rotor. Although an interesting study, the ten percent gain is not enough to justify the expense on a motor that is considered "inexpensive", and where efficiency is not high to begin with.

A good candidate for a proof of principle motor is an induction motor wound with superconductive wire where the entire motor operates submerged in liquid nitrogen. The motor can use superconducting wire before we reach the current density goal of 100,000 Amperes/cm^2.

3.4   AC LOSSES IN HTSC AT UNIVERSITY OF WISCONSIN

Mohamed A. Hilal has been studying the critical twist length and the eddy current losses for round conductors. His results are reported. He has developed a model for hysteresis losses and some results have been obtained and reported.

3.4.1   HTSC Eddy Current Losses in Twisted Filamentary Composite

All newly discovered high temperature superconductors exhibit anisotropy in critical current density capability due to their two dimensional

crystalline structure. Such characteristics seem to be an intrinsic property and HTSC will have high critical current density capability in two directions but lower current density in the third normal direction. This will impact the nature of the induced eddy currents as well as their magnitude.

CRITICAL TWIST PITCH

First we consider as an example the conductor design using low temperature superconductor. It is necessary in this case to use it in a multifilamentary form to reduce flux jumps to satisfy the requirements of intrinsic stability. In the presence of time varying field, the filaments will be strongly coupled which can result in excessive ac losses. The filaments are twisted to decrease coupling and reduce eddy current losses. Low ac losses using low temperature superconductor is achieved by twisting the filaments so that the critical current density is not exceeded anywhere along the twist pitch. The critical twist pitch, the twist pitch at which the filament is carrying a critical current density at the center, is given by

$$L_c = (\pi^3 \, \rho_e \, dJ_c/\dot{B})^{1/2} \tag{1}$$

where ρ_e is the effective resistivity, d is the filament (or strand) diameter and $\dot{B}$ the field rate of change.

It will also be required to have HTSC multifilamentary conductors with twisted filaments to interrupt filament decoupling and reduce eddy current losses especially in ac applications. This will also be required to have intrinsically stable conductors.

To determine the critical twist pitch for oxide superconductors, we assume that the critical current density in the longitudinal direction, J_{cl}, is greater than the critical current density in the transverse direction, J_{ct}.

Due to the anisotropy of critical current density, three critical twist pitches are defined which correspond to the following conditions:

1- The transverse critical twist pitch, L_t.

The current in the transverse direction of the superconductor is equal to the transverse critical current at a point along the twist pitch but the longitudinal current anywhere along the filament is less than the critical current.

2- The longitudinal critical twist pitch, L_c.

If L_c is exceeded, the superconductor current is equal to the critical current at a point along the twist pitch whereas the transverse current density in the matrix is below J_{ct}.

3- The anisotropy critical twist pitch, L_{ct}.

As the twist pitch L_{ct} is reached, the superconductor current is equal to the critical current at a point along the twist pitch and the transverse current density exceeds J_{ct} along part of the twist pitch.

The critical twist pitch is a function of, the magnetic field time rate of change, $\dot{B}$, the transverse matrix effective resistivity, ρ_e, and the conductor geometry. The conductor geometry shown in figure 3.4.1.1 is assumed to derive the different critical expressions of the different twist pitches. L_c is obtained by assuming that the current anywhere along the filament is below the critical current and no voltage gradient exists along the filament. Assume that the conductor is exposed to an external uniform field, $\dot{B}_{ext}$ and the conductor is long so that no longitudinal net current is induced in the matrix due to $\dot{B}_{ext}$. Whereas the longitudinal voltage gradient will be zero, a circumferencial voltage gradient will be induced. The voltage difference at
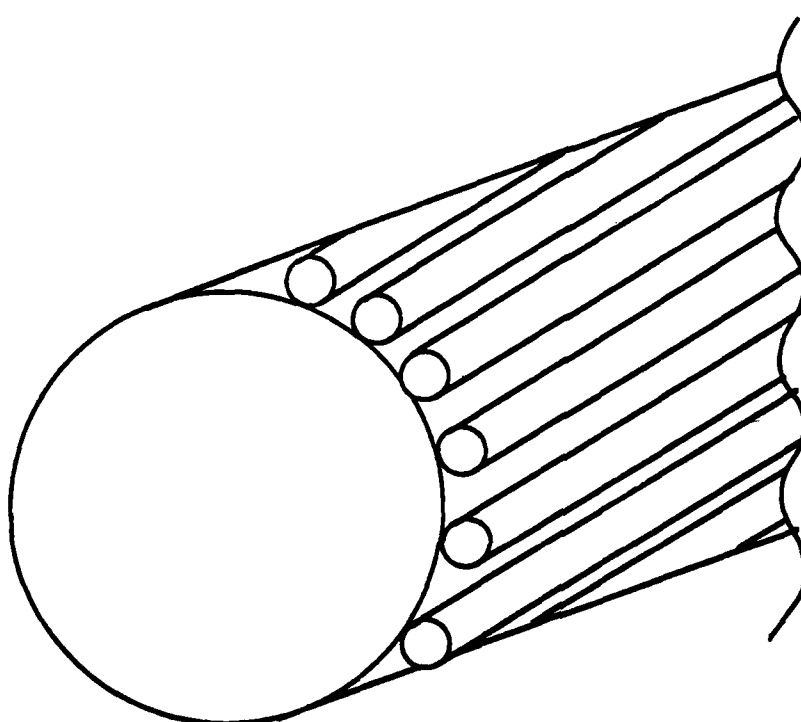
FIGURE 3.4.1.1. A SCHEMATIC OF ROUND CONDUCTOR
HAVING SUPERCONDUCTING STRANDS
ON THE SURFACE
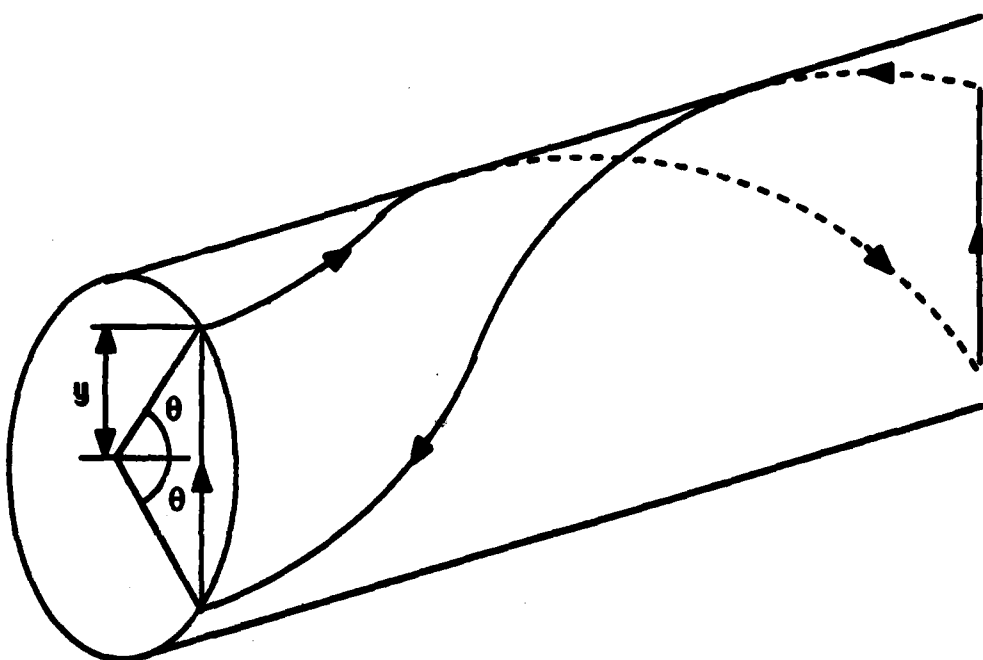
FIGURE 3.4.1.2. CONTOUR PATH USED TO DETERMINE THE ELECTRIC FIELD DISTRIBUTION

any two points separated by an angle 2θ, can be obtained by following two filaments along the path shown in figure 3.4.1.2. This gives

$$\Delta V = (2\,\dot{B}_i\,yL\,/\,2\pi) \tag{2}$$

where $\dot{B}_i = \dot{B}_{ext} - \dot{B}_{self}$, L is the twist pitch and $\dot{B}_{self}$ is the self field. The electric field within the matrix is thus uniform and is given by

$$E = (\dot{B}_i\,L\,/\,2\pi) \tag{3}$$

It is interesting to note that the self magnetic field produced within the conductor is uniform and the net magnetic, $\dot{B}_i$, is thus uniform.

The current density in the matrix is given by

$$J_y = (\dot{B}_i\,L\,/\,2\pi\,\rho_e) \tag{4}$$

The transverse current density in the superconductor is given by

$$J_t = J_y\,\sin\theta = (\dot{B}_i\,L\,/\,2\pi\,\rho_e)\,\sin\theta \tag{5}$$

The transverse critical twist pitch is obtained by requiring that $J_t = J_{ct}$ at $r = 0$ and is given by

$$L_t = (2\pi\rho\,J_{ct}\,/\,\dot{B}_i) \tag{6}$$

The longitudinal twist pitch is determined by calculating the filament (or strand) current along a twist pitch which is given by

$$I\,' = (\dot{B}_i L\,/\,2\pi\,\rho_e)\ _0\!\int^\theta \sin\theta\,d\theta \tag{7}$$

where $I\,'$ is the current per unit circumferencial length. Given that $I = I_c$, we have

$$L_c = (\pi^3\,\rho_e\,dJ_c/\dot{B})^{1/2} \tag{8}$$

which is the same as equation 1. Assuming $\dot{B}_{self}$ is small compared to $\dot{B}_{ext}$, combining equations 6 and 8 gives

$$L_t/L_c = [4\rho\,/\,\pi\dot{B}dJ_c]^{1/2}\,J_{ct} \tag{9}$$

For ac motor applications the critical transverse pitch assuming the values given in Table 1 are 0.11 mm using copper and are 2 cm using 70 Cu – 30 Ni

Table 3.4.1.1

	Copper	70 Cu – 30 Ni
ρ_e, Ω, m	$\sim 2 \times 10^{-9}$	36×10^{-8}
B, Tesla	3	3
frequency, $\sec^{-1}$	60	60
J_c, A/cm^2	10^5	10^5
d, m	10^{-5}	10^{-5}
J_{ct}, A/cm^2	10^3	10^3
L_c, m	7.4×10^{-4}	9.93×10^{-3}
L_{ct}, m	1.1×10^{-4}	2×10^{-2}

alloy. L_c using copper is 0.74 mm and 0.993 cm using the 70/30 copper nickel alloy. It can be seen that t is necessary to use high resistivity matrix to increase both the transverse and the longitudinal critical twist pitch.

The longitudinal and the transverse critical twist pitch are plotted versus applied field for 60 Hz ac field in Figure 3.4.1.3 for J_{ct}/J_c equal 0.01.

Equation (7) is used to determine L_{ct} by assuming that the current density for angles greater than θ_m is equal to J_{ct}. This gives

$$I' = (\dot{B}/\rho_e) (L/2\pi)^2 [1 - \cos \theta_m] + (L/2\pi) J_{ct} \cos \theta_m \tag{10}$$

The angle θ_m is given by

$$\sin \theta_m = (J_{ct} / \dot{B}/\rho_t [L/2\pi]) = 2/\pi^2 (L_c/d) (J_{ct}/J_c) (L_c/L_{ct}) \tag{11}$$

Combining equations 10, 11 and 8 and given that $I' = \pi/4 \, d \, J_c$ gives

$$(L_{ct}/L_c)^2 [1 - \cos \theta_m] + 1/2\pi^2 (L/L_c)(L_c/d)(J_{ct}/J_c) \cos \theta_m = 1 \tag{12}$$

The ratio L_{ct}/L_c is obtained solving equation 12. The L_{ct}/L_c is plotted versus the dimensionless group $G[G = (L_c/d)(J_{ct}/J_c)]$ in Figure 3.4.1.4. The θ_m, the angle at which the transverse critical current is exceeded, is plotted versus G in Figure 3.4.1.5.

EDDY CURRENT LOSSES

First we calculate eddy current losses assuming that the current density in the transverse direction does not exceed the transverse critical density of the superconductor. In this case the losses are due to the I^2R dissipation in the matrix and is given by

$$P = (2/\pi a^2) \, _0\int^{\pi/2} E_y J_y \, 2y dx \tag{13}$$

where P_o is the eddy current loss per unit volume.

The above integration gives
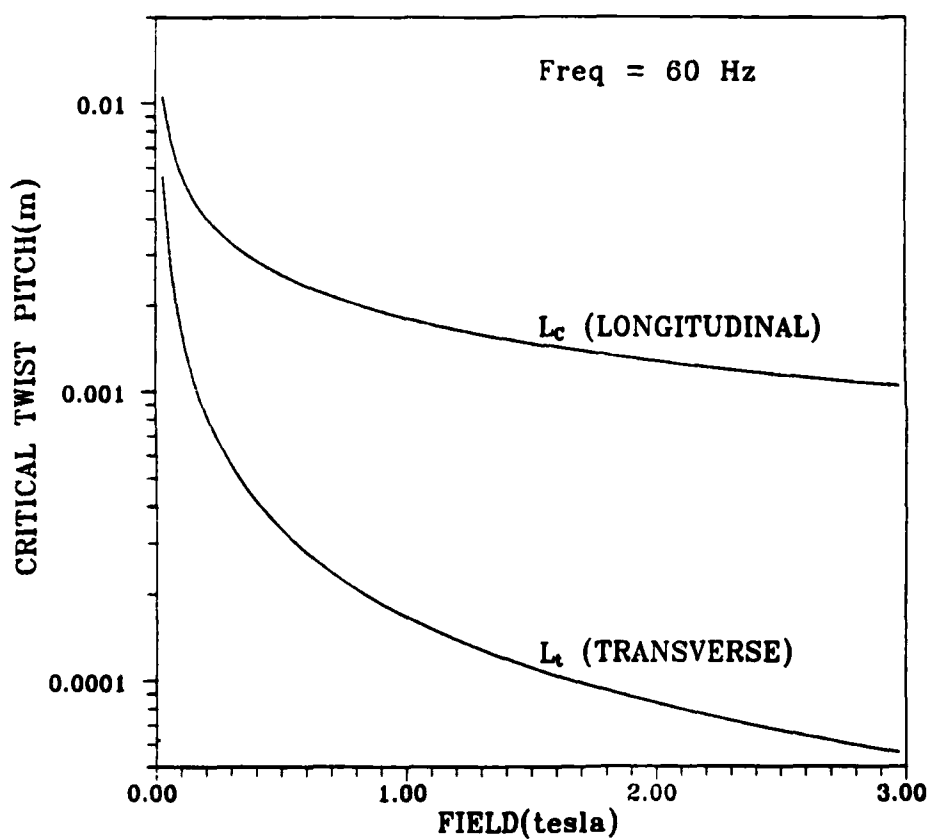
FIGURE 3.4.1.3. DEPENDENCE OF L_c AND L_t ON 60 HZ AC FIELD
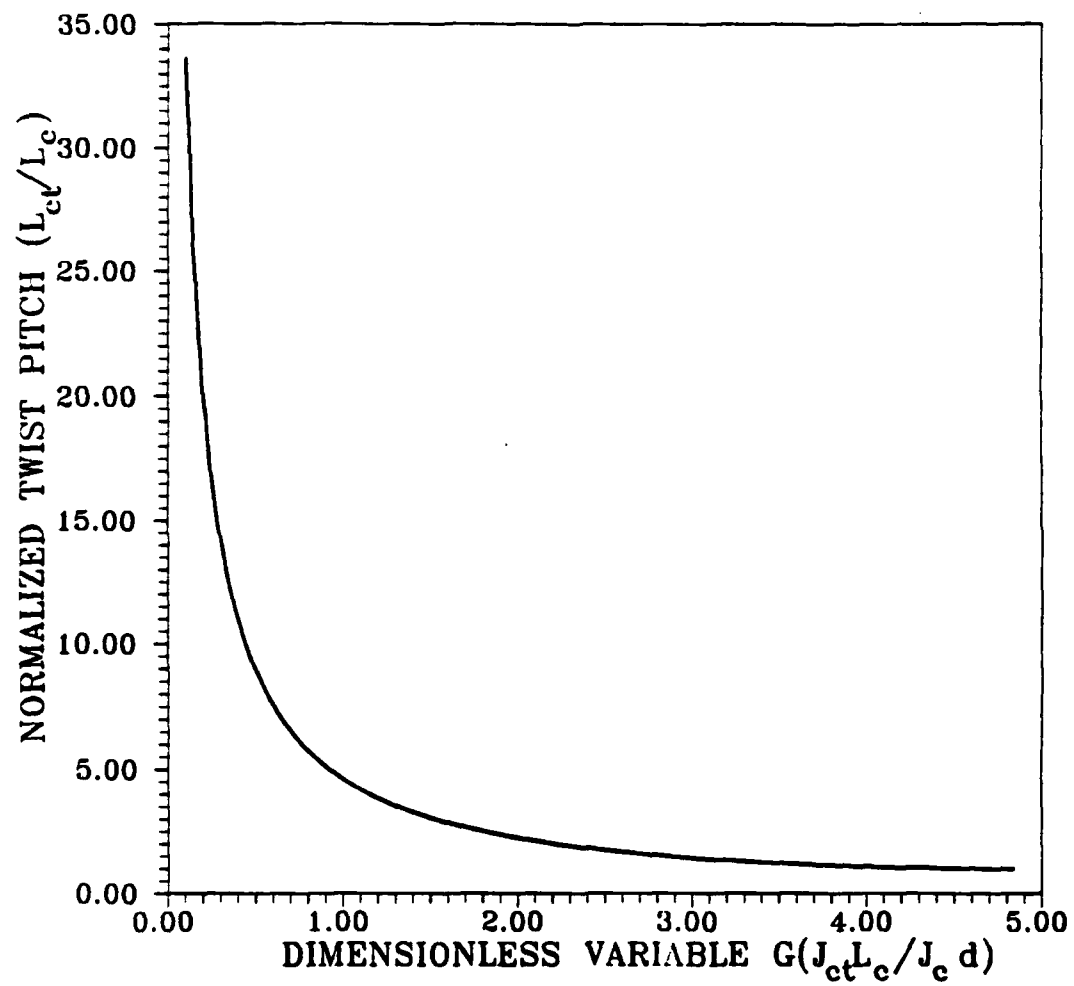
FIGURE 3.4.1.4. L_{ct}/L_c STRONGLY DEPENDENS ON
J_{ct}/J_c AND L_c/d RATIOS
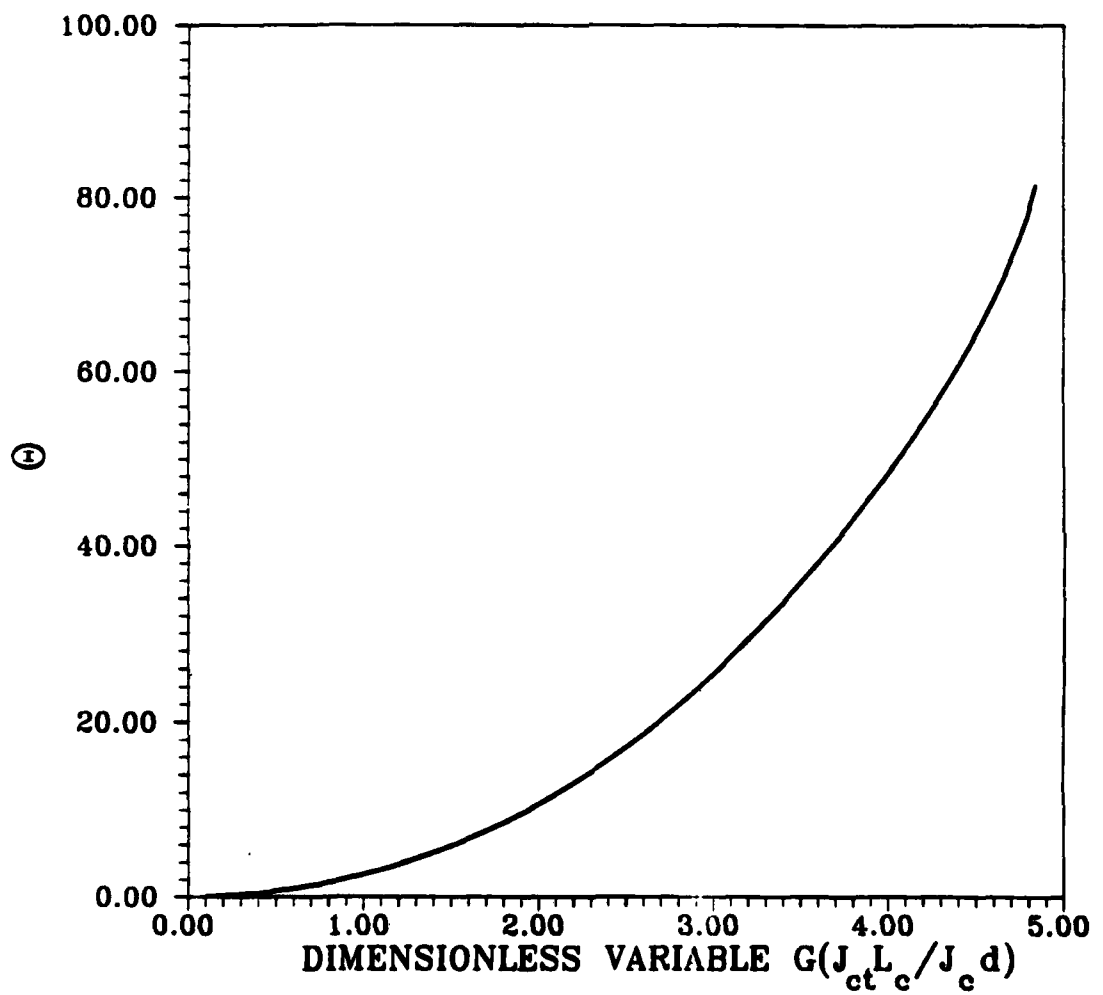
FIGURE 3.4.1.5. θ INCREASES AS G INCREASE

$$P_o = (2\dot{B}_i^2 / \mu_o) \; \tau_o \tag{14}$$

where the time constant τ_o is given by

$$\tau_o = (\mu_o/2\rho) \; (L_c/2\pi)^2 \tag{15}$$

when the critical current density in the transverse direction is exceeded losses are generated both in the superconductor and in the matrix. The total power losses are given by

$$P = (2/\pi a^2) \; [_0\!\int^\Theta J_y \; E_y \; 2y \; dy + _0\!\int^{\pi/2} J_{ct} \; E_y \; 2y \; dy] \tag{16}$$

The above integration gives

$$P = (2\dot{B}_i^2 / \mu_o) \; \tau \tag{17}$$

where the time constant τ is given by

$$\tau/\tau_o = P/P_o = 1/\pi \; (L_{ct}/L_c)^2 \; [2\Theta - \sin 2\Theta + \sin \Theta \; (\pi - 2\Theta + \sin 2\Theta)] \tag{18}$$

The losses in the stabilizer per unit volume of the conductor, P_{st}, is given by

$$P_{st} = (2\dot{B}_i^2 / \mu_o) \; \tau_{st} \tag{19}$$

where

$$\tau_{st}/\tau_o = P_{st}/P_o = 1/\pi \; (L_{ct}/L_c)^2 [2\Theta - \sin 2\Theta + \gamma_{st} \sin^2\Theta \; (\pi - 2\Theta + \sin 2\Theta)] \tag{20}$$

where γ_{st} is the ratio of the stabilizer volume to the total volume. Losses in the superconductor are given by

$$P_{sc} = (2\dot{B}_i^2 / \mu_o) \; \tau_{sc} \tag{21}$$

where

$$\tau_{sc}/\tau_o = P_{sc}/P_o = (\gamma_{sc}/\pi)(L_{ct}/L_c)^2 \; [\sin \Theta \; (\pi - 2\Theta + \sin 2\Theta)(1 - \sin \Theta)] \tag{22}$$

and γ_{sc} is the ratio of the superconductor to the stabilizer volume. Note that (L_{ct}/L_c) is a function of Θ and larger values of (L_{ct}/L_c) correspond to large values of Θ. The normalized total losses (P/P_o), stabilizer losses

(P_{st}/P_o) and superconductor losses (P_{sc}/P_o) are plotted versus (L_{ct}/L_c) in Figure 3.4.1.6. It can be seen that a large fraction of the losses can be generated in the superconductor.

Next Quarter Work

This will include the following tasks:

1- The different critical lengths will be studied for ribbon type conductors.

2- The eddy current losses for a typical motor windings will be calculated.

3- The effect of transport current both on the critical twist pitch and on losses will be studied.

The critical twist pitch for ribbon type conductors will be studied. The losses in a ribbon wound superconducting motor will be calculated.

3.4.2   Hysteresis Losses in High Temperature Superconductors

Introduction

The critical state model is extensively used to characterize the magnetization behavior of low temperature superconductors. We use the critical state model here to determine the magnetization characteristics of HTSC.

HTSC Magnetization Model

Whereas the magnetization and transport critical current density of low temperature superconductors, LTSC, are basically the same, they can differ by orders of magnitude for high temperature superconductors. The transport critical current density J_c of HTSC is found to be significantly less than the
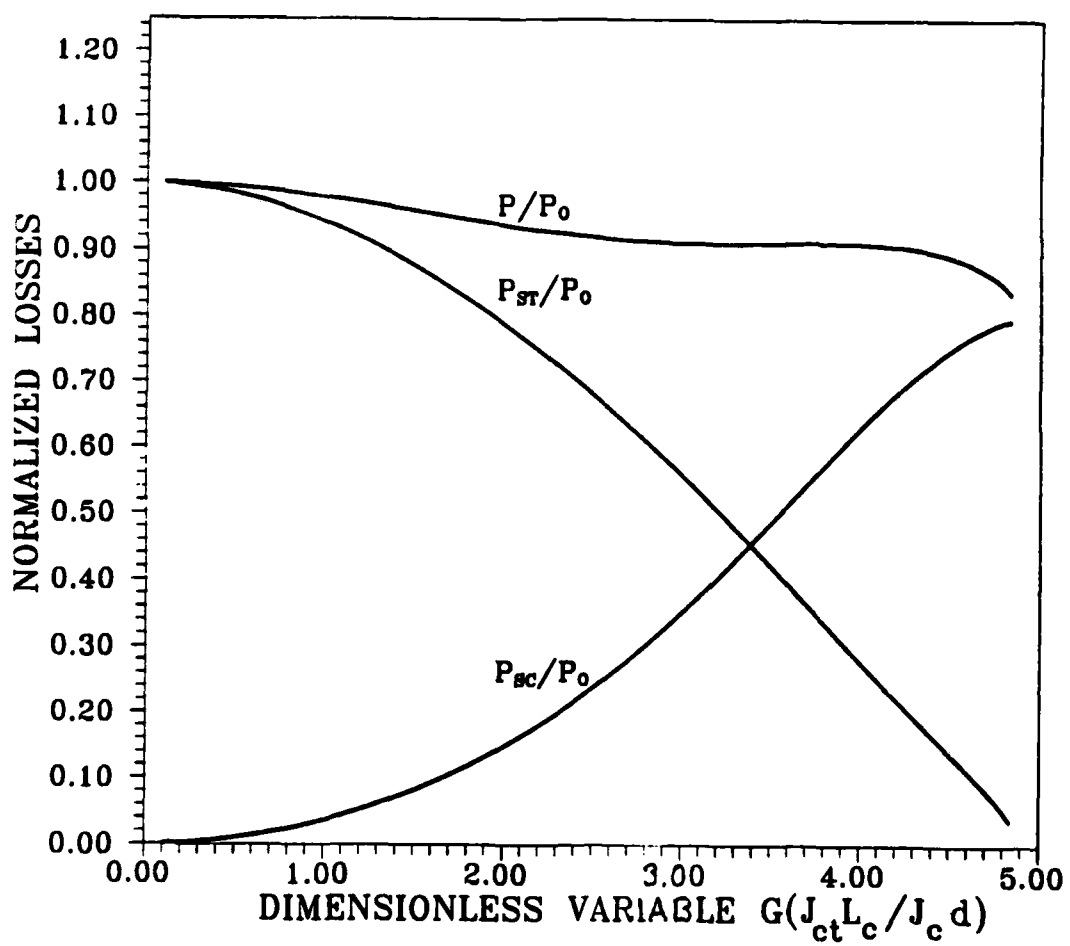
FIGURE 3.4.1.6. NORMALIZED TOTAL, STABLIZER AND
SUPERCONDUCTOR LOSSES VERSUS G

magnetization critical current density, J_M, due to the presence of weak links in between grains.

Due to the difference between J_M and J_c the model developed to describe LTSC magnetization cannot be used for high temperature superconductors. Figure 3.4.2.1 shows the current loops developed when HTSC is exposed to magnetic field. The figure shows minor current loops within the individual grains and major current loops due to the transport current flowing across the grains. The HTSC magnetization is determined as a function of the two critical current densities J_c and J_M.

We consider the case of HTSC slab exposed to magnetic field density B. We assume that the field is slowly increasing. As the field penetrates the slab, the following distinct regions can exist.

a. Full Grain Penetration

Figure 3.4.2.2 shows a part of the slab where the individual grains are fully penetrated. The magnetic field and the current density distribution across the individual grains are shown in Figure 3.4.2.2. Assume that the grain size is Δ. The relation between the transport critical current density and the magnetization critical current density in this region is given by

$$J_c \Delta = ([\Delta/2] + \delta) J_M - ([\Delta/2] - \delta) J_M = 2 \delta J_M \tag{1}$$

where δ is defined as the displacement of the point within the grain at which current density reverses. Equal magnetic field on both sides of the grain will result in zero transport current and zero δ.

Rearranging equation 1 gives

$$\delta/\Delta = 0.5 \lambda \tag{2}$$
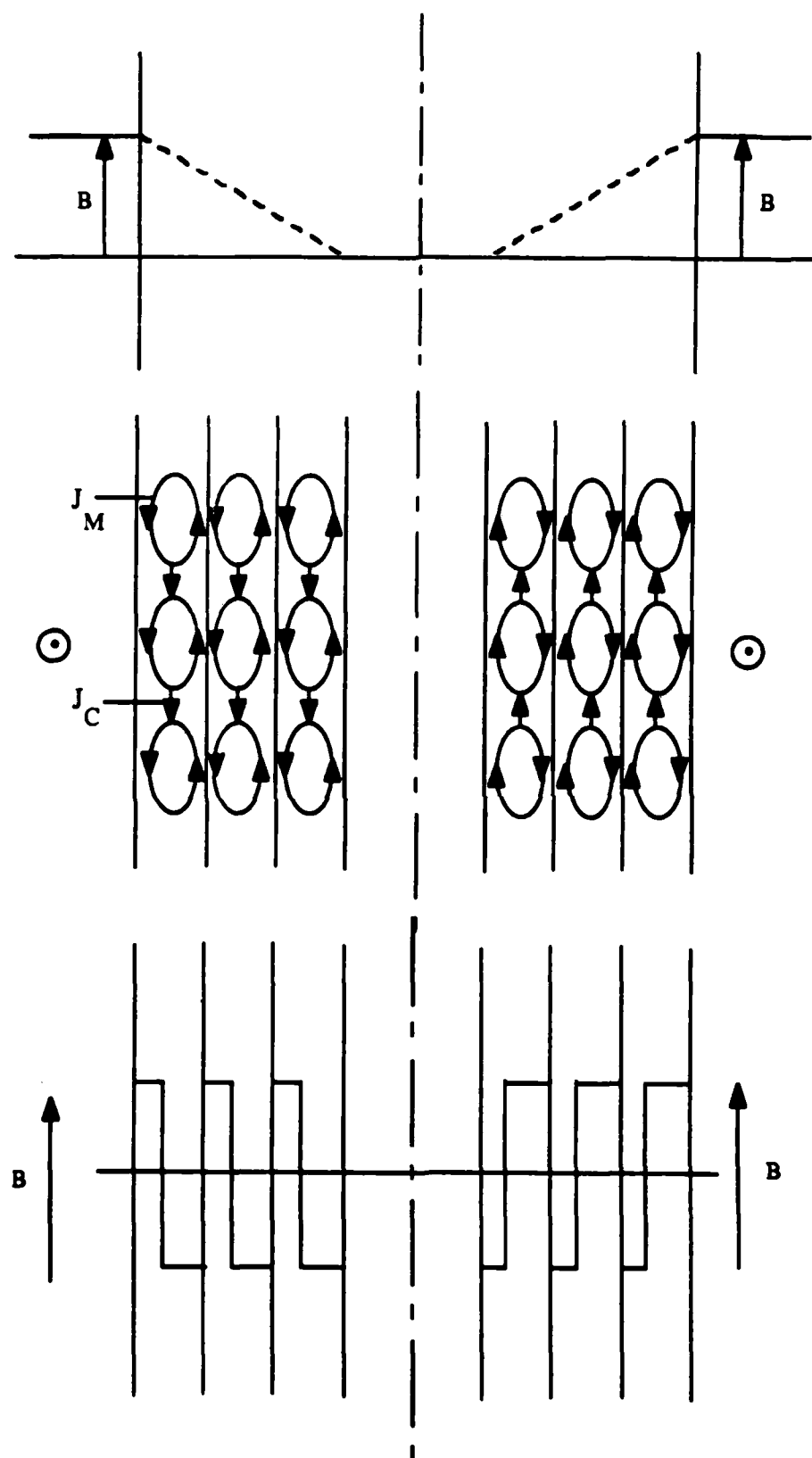
FIGURE 3.4.2.1. MINOR AND MAJOR CURRENT LOOPS IN HTSC
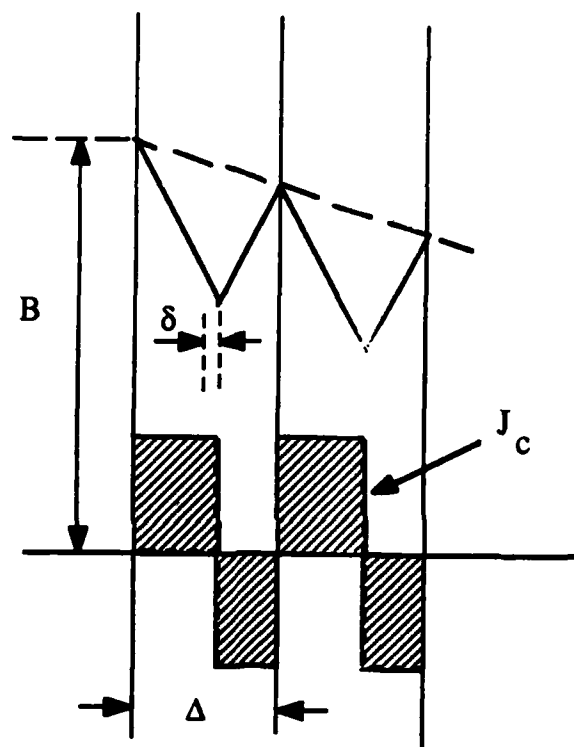
FIGURE 3.4.2.2. GRAINS ARE FULLY PENETRATED AND
FIELD PENETRATION

where λ is defined as

$$\lambda = J_c / J_M \tag{3}$$

Note that full penetration of the grain by the field means further field penetration of the adjacent grains.

b. Partial Grain Penetration but Full Field Penetration

Figure 3.4.2.3 shows that the grain is partially penetrated by the field. The magnetic field, however, penetrates the sample inducing magnetization current in a number of grains and this region is defined as full field penetration. In this case we have

$$\delta_i / \Delta = 0.5 \lambda \tag{4}$$

where

$$\delta_i = 0.5 (x_i - x_{i-1}) \tag{5}$$

and x_i and x_{i-1} are defined as shown in Figure 3.4.2.3.

c. Partial Grain Penetration and Partial Field Penetration

This region represents the last grain penetrated by the field. It thus consists of one grain in each half of the slab. The relation between J_c and J_M is given by

$$x_M J_M = x_c J_c \tag{6}$$

where x_c and x_M are defined as shown in Figure 3.4.2.4.

HTSC MAGNETIZATION ANALYSIS

The slab is divided to a large number of thin slabs representing the sample grains. The three regions described above are separately considered in this analysis.

a. Full Grain Penetration
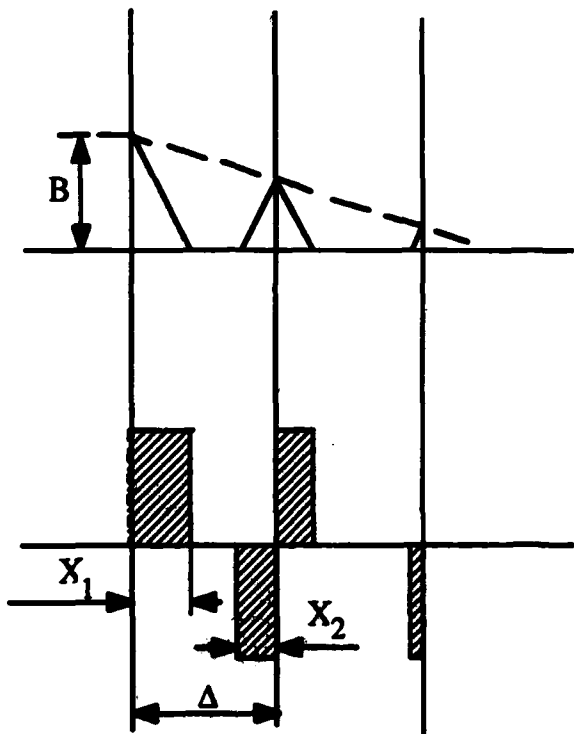
FIGURE 3.4.2.3. GRAINS ARE PARTIALLY PENETRATED,
BUT FULL FIELD PENETRATION
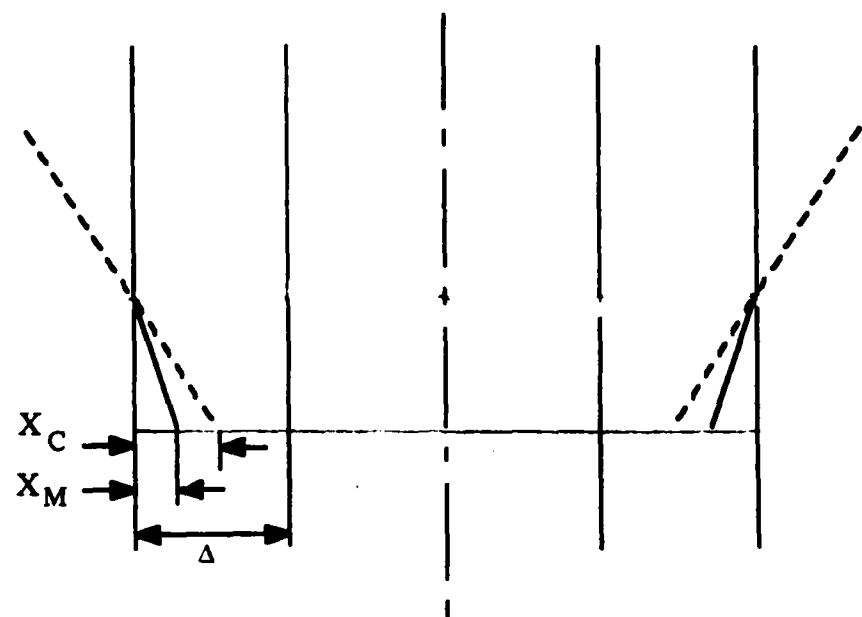
FIGURE 3.4.2.4. REGION OF PARTIAL GRAIN PENETRATION
AND PARTIAL FIELD PENETRATION

The slab is divided to N slabs as shown in Figure 3.4.2.5. The slabs are designated B_o, B_1, ... B_i, ... B_N. The field at the grain interfaces is designated 0, 1, 2, ... i, ... to N. The field on the right hand side of the slab is designated B_{i-1} and is designated B_i on the right hand side. B_i is given by

$$B_i = B_o - i \ \mu_o \ J_c \ (B_i) \tag{7}$$

where B_o is the applied magnetic flux density and B_i is the average magnetic flux density within the grain. Note that J_c is assumed constant within the grain. The flux within the ith slab is given by

$$\Delta X_i = 1/2 \ ([\Delta/2] + \delta) \ [2 \ B_{i-1} - \mu_o \ J_M \ ([\Delta/2] + \delta)]$$
$$+ \ 1/2 \ ([\Delta/2] - \delta) \ [2 \ B_i - \mu_o \ J_M \ ([\Delta/2] + \delta)] \tag{8}$$

Given that $B_i = B_{i-1} - \mu_o \ J_c \Delta$, rearranging equation 8 gives

$$\Delta X_i = B_{i-1} \ \Delta \ -0.5 \ [\mu_o \ J_M \ (1 - 2\lambda) \ \delta\Delta \ -\mu_o \ J_M \ \Delta^2/2 \ -\mu_o \ J_M \ \lambda\Delta^2] \tag{9}$$

The total flux within the full grain penetration region for the special case of having J_c and J_M independent of field is given by

$$\sum_n \Delta X_i = n \ \Delta \ B_o - \mu_o \ J_M \ \Delta^2 \ [\lambda \ (n+1) + 0.5 \ \lambda \ (1 - 2\lambda) + 1/2 + \lambda] \tag{10}$$

b. Partial Grain Penetration but Full Field Penetration

The field at the interfaces of the ith slab, see Figure 3.4.2.3, are given by

$$B_{i-1} = \mu_o \ J_M \ X_{i-1} \tag{11}$$

and

$$B_i = \mu_o \ J_M \ X_i$$

The flux penetrating the ith region is given by
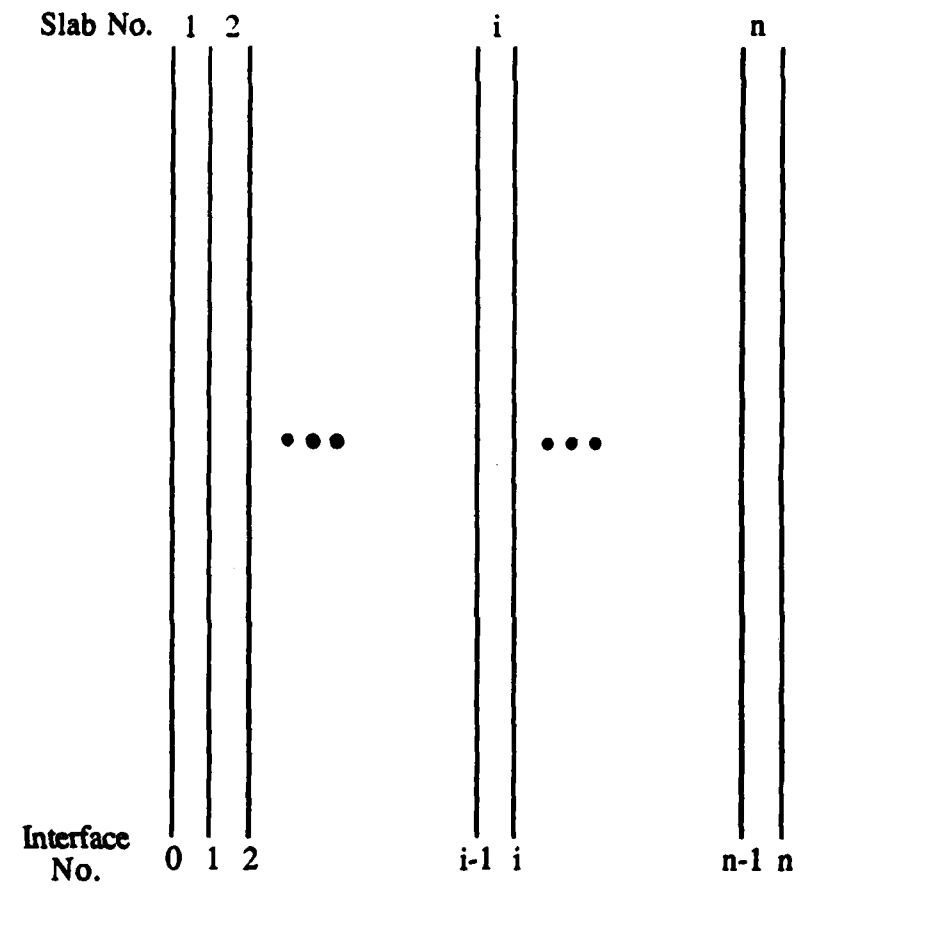
FIGURE 3.4.2.5.   NUMBERING SEQUINCE OF THE GRAIN SLABS

$$\Delta X_i = 1/2 \ (B_{i-1} \ x_{i-1} + B_i \ x_i) = (0.5/\mu_o \ J_M) \ (B_{i-1}^2 + B_i^2) \tag{12}$$

Given that

$$B_i = B_{i-1} - \mu_o \ J_c \ \Delta \tag{13}$$

we have

$$\Delta X_i = (0.5/\mu_o \ J_M) \ [2 \ B_i^2 + 2 \ \mu_o \ J_c \ B_i \ \Delta + \mu_o \ J_c^2 \ \Delta^2] \tag{14}$$

We define B_{PG} as the field above which the grains are fully penetrated. To determine B_{PG} we have

$$(B_{PG} + \mu_o \ J_c \ \Delta/\mu_o \ J_M) + (B_{PG}/\mu_o \ J_M) = \Delta \tag{15}$$

which gives

$$B_{PG} = 0.5 \ \mu_o \ (J_M - J_c) \tag{16}$$

The total flux in the partial grain region is obtained by combining equations 14, 16 and $B_i = B_{PG} - i \ \mu_o \ J_c \ \Delta$. This gives after some lengthy manipulation

$$\Sigma \ \Delta X_i = m \ \Delta \ \lambda/\eta \ B_{PG} \ [1 - \eta m + \eta^2 \ (1/3 \ m^2 + 1/6)] \tag{17}$$

where m is the number of the grain slabs in the partial field penetration region and η is defined by

$$\eta = (\mu_o \ J_c \ \Delta/B_{PG}) = (\mu_o \ \lambda \ J_M \ \Delta/B_{PG}) \tag{18}$$

c. Partial Grain and Partial Field Penetration

In this case the field is zero on one side of the slab and is given by

$$B \le \mu_o \ J_c \ \Delta \tag{19}$$

on the other side of the slab. The flux penetrating this region is given by

$$\Delta X = 1/2 \ \mu_o \ J_c \ x_c^2 = 1/2 \ \mu_o \ J_M \ x_M^2$$

where x_c and x_M are defined by equation 6.

HTSC MAGNETIZATION HYSTERESIS

The above equations are used to calculate magnetization loops assuming different J_c, J_M grain size and sample size. The loops are obtained for the case of constant J_c and constant J_M and thus can be used to predict the magnetization peaks which take place at low field.

Figure 3.4.2.6 magnetization loops for different size samples. J_M is assumed to be equal to 10^2 A/cm^2. Figures 3.4.2.7, 3.4.2.8 and 3.4.2.9 are the same as Figure 3.4.2.6 but J_c is equal to 10^3, 10^4 and 8 x 10^4 A/cm^2 respectively. As can be seen from these figures the magnetization loop area is small for small J_c. Also the grain size has more impact on the magnetization loop area percentage wire at lower values of J_c.

Figures 3.4.2.10, 3.4.2.11, 3.4.2.12 and 3.4.2.13 show the magnetization loop for 10^{-4} m slabs having different grain size. Again at lower J_c grain size has more impact on the magnetization loop area. At J_c = 8 x 10^4 all loops coincide.

Figure 3.4.2.14 shows the magnetization loop for 10^{-4} m sample size and 10^{-5} m grain size for different values of J_c. It can be definitely seen that the magnetization loop is influenced both by J_c and J_M.

The magnetization curve shown doesn't show the magnetization peak usually observed at low field. This is expected since J_c and J_M are assumed independent of field.

NEXT QUARTER WORK

The field dependence of J_c and J_M will be considered in modifying the model. The hysteresis losses will be calculated using the above model to determine its dependence on J_c, J_M, applied field, grain size and sample size.
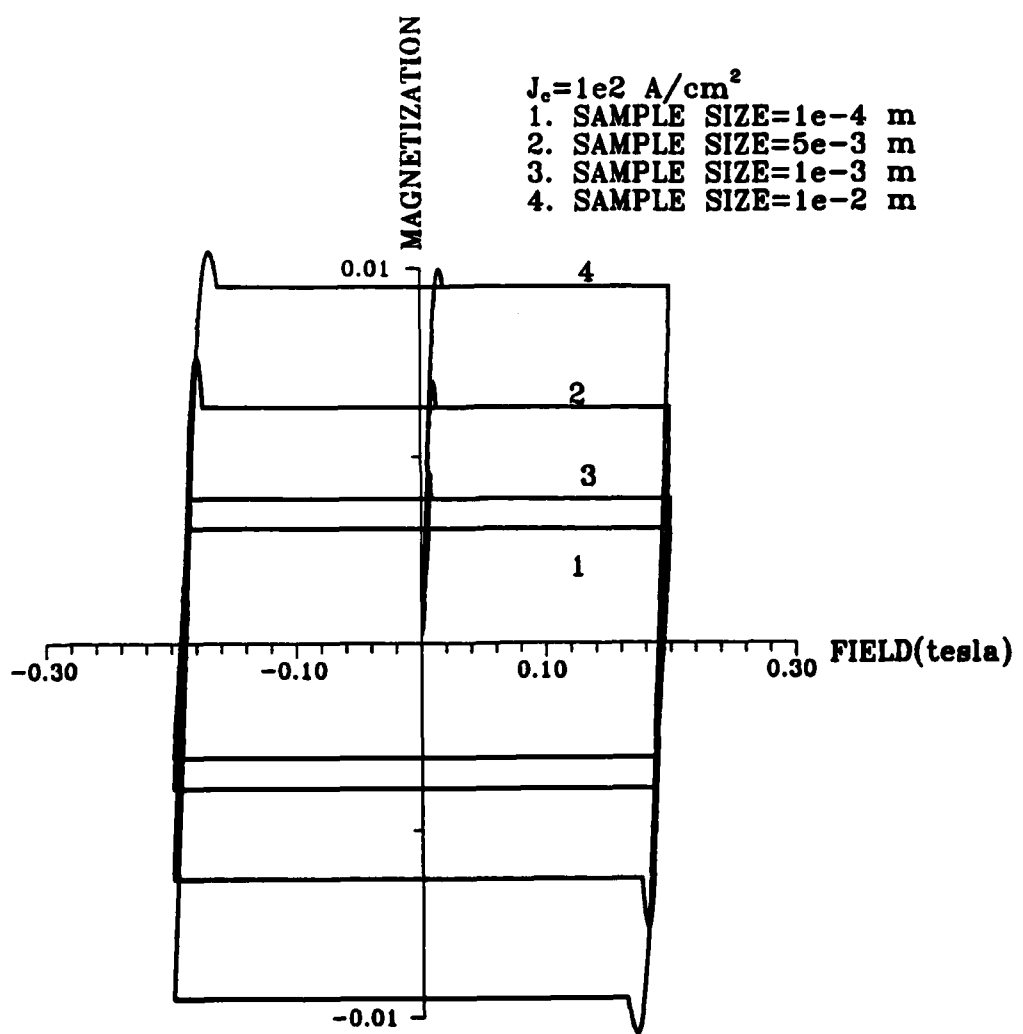
FIGURE 3.4.2.6
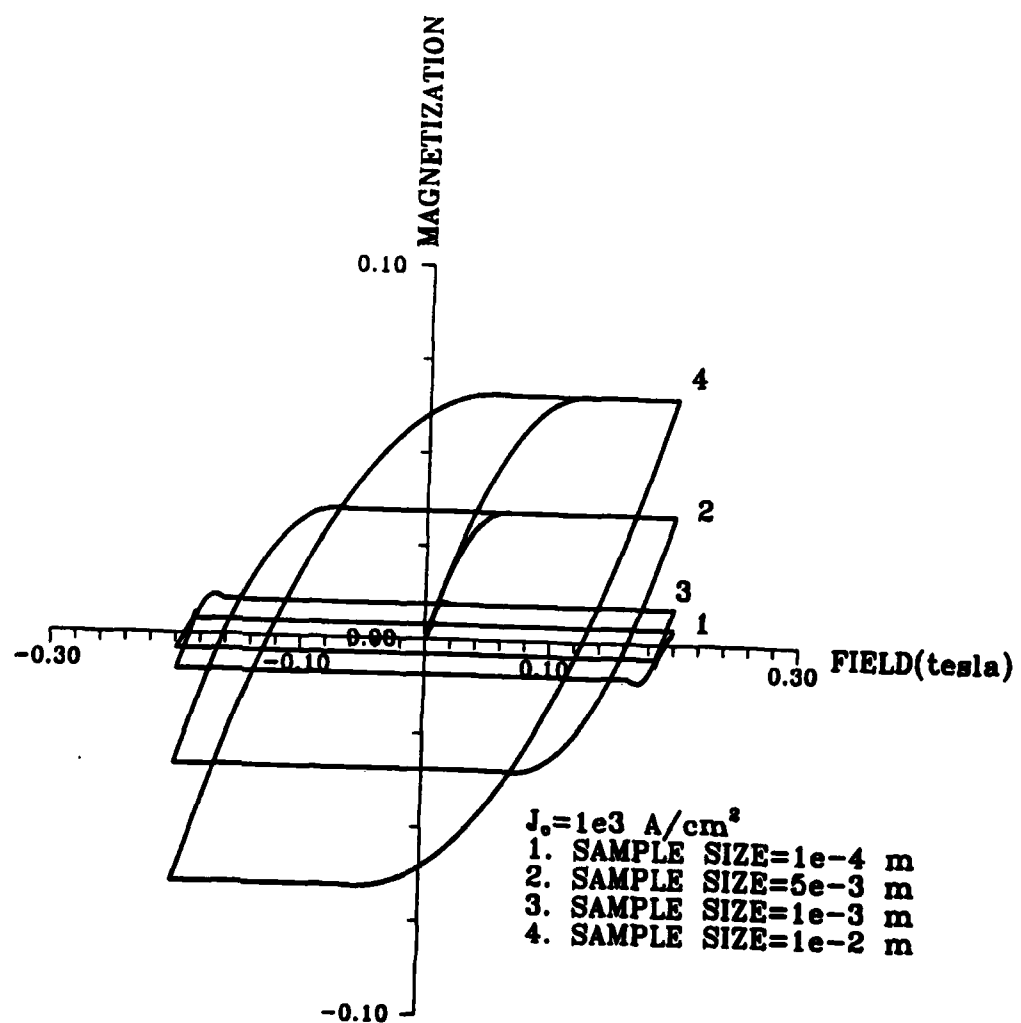
FIGURE 3.4.2.7
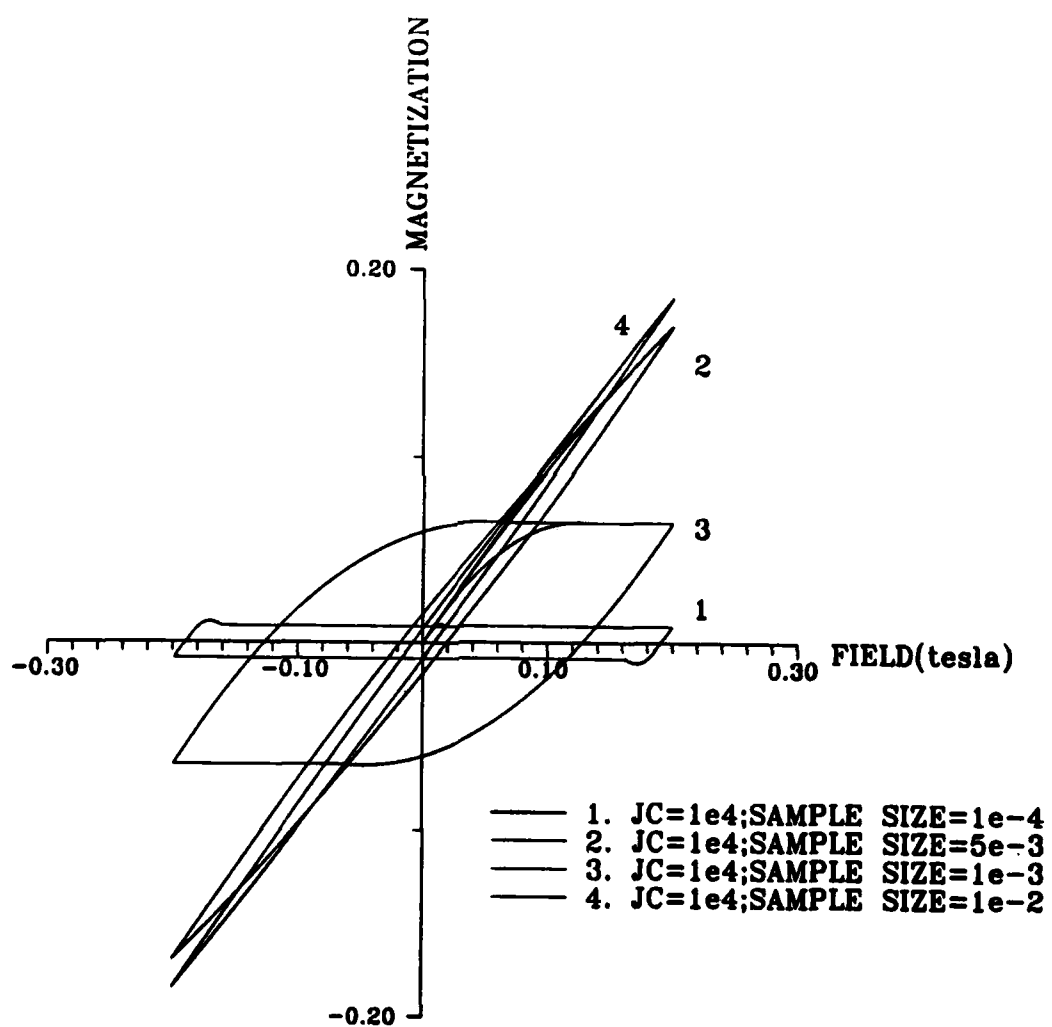
FIGURE 3.4.2.8
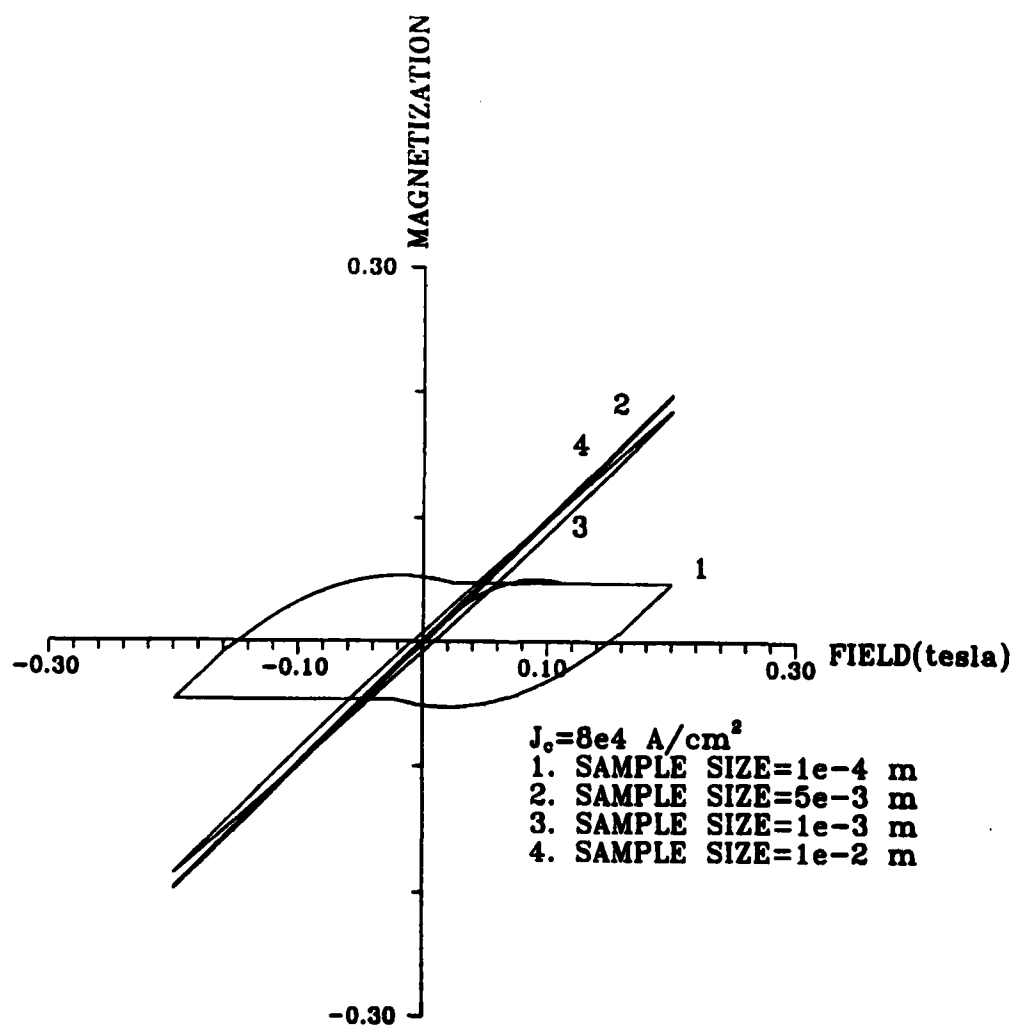
FIGURE 3.4.2.9
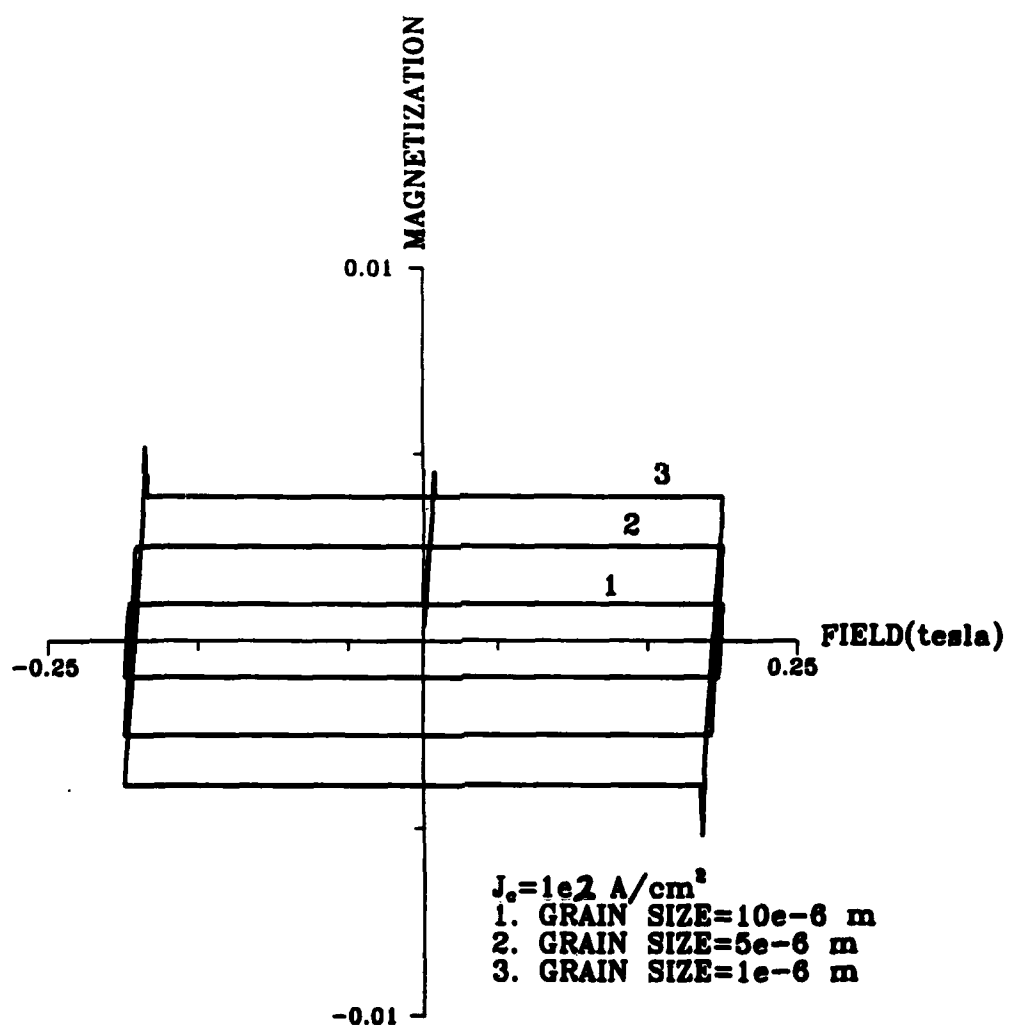
FIGURE 3.4.2.10
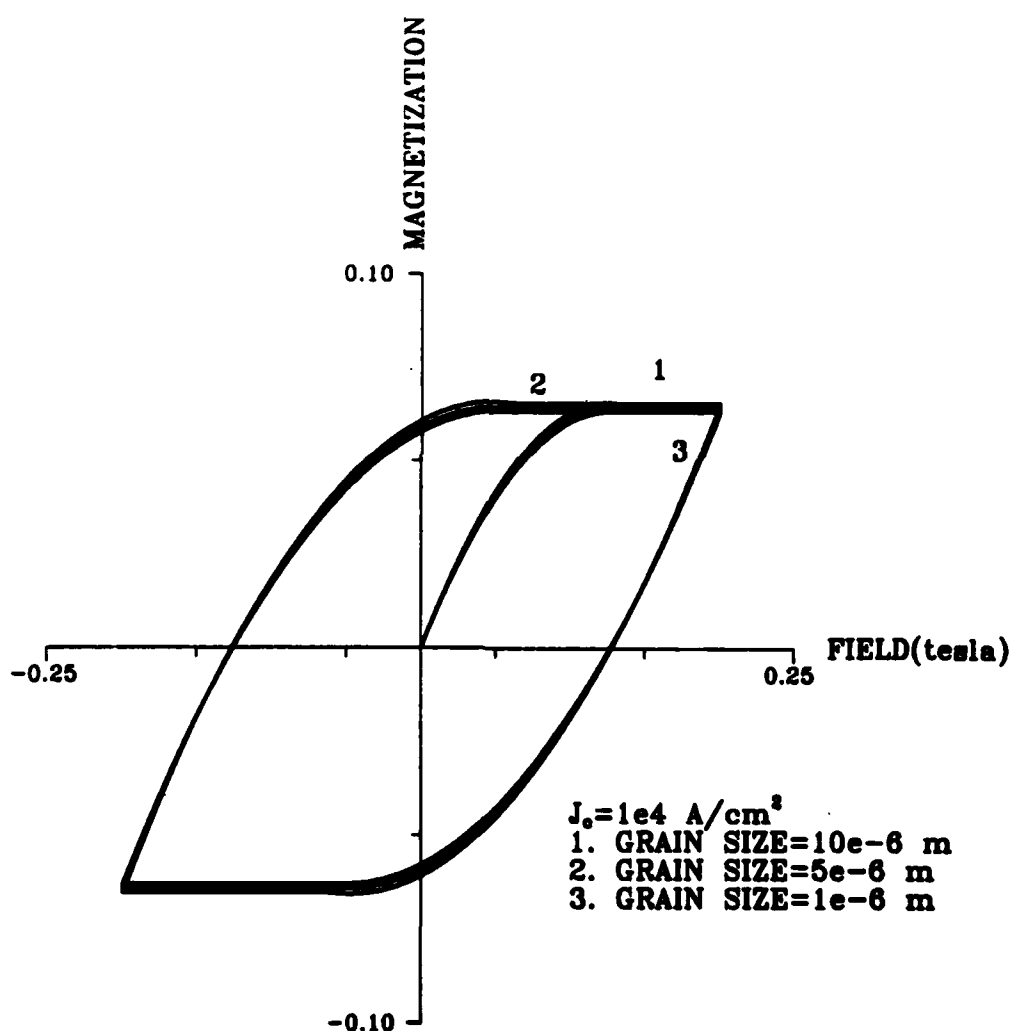
FIGURE 3.4.2.11
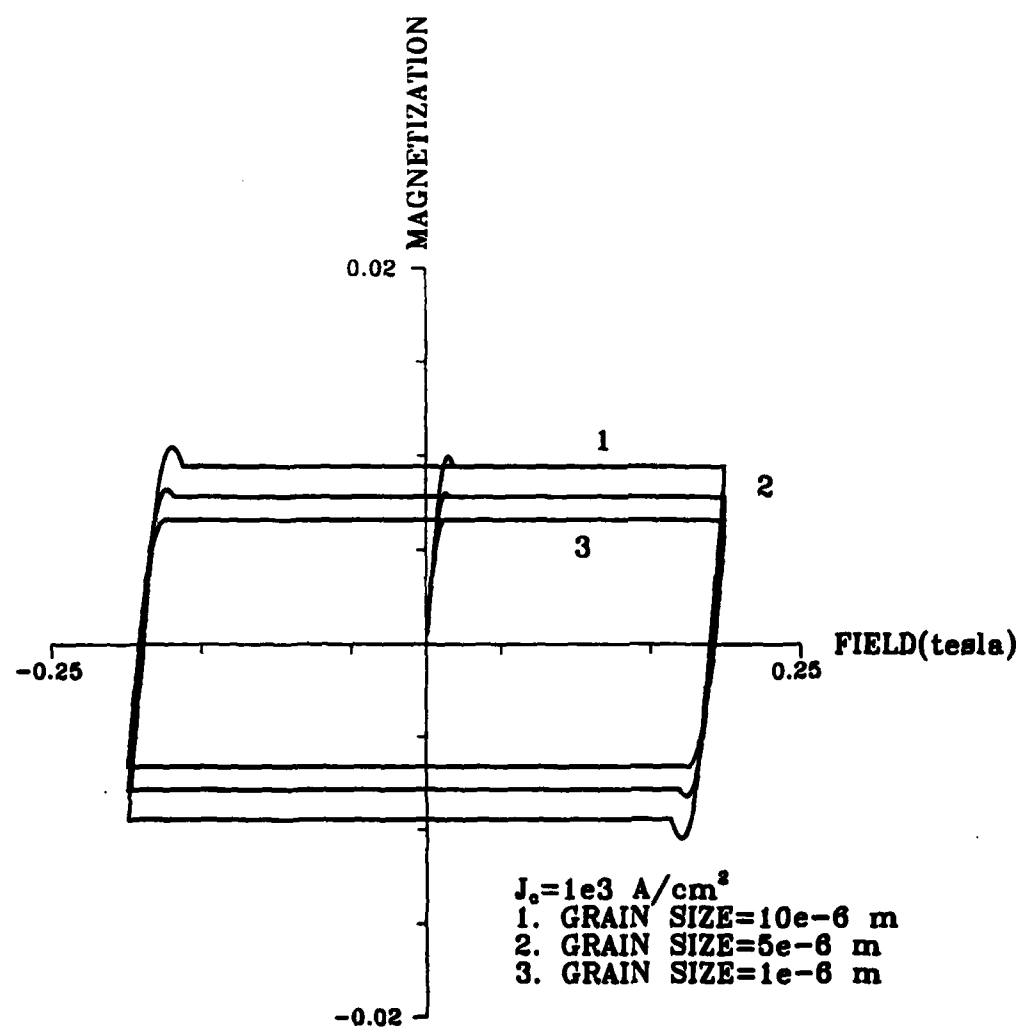
FIGURE 3.4.2.12
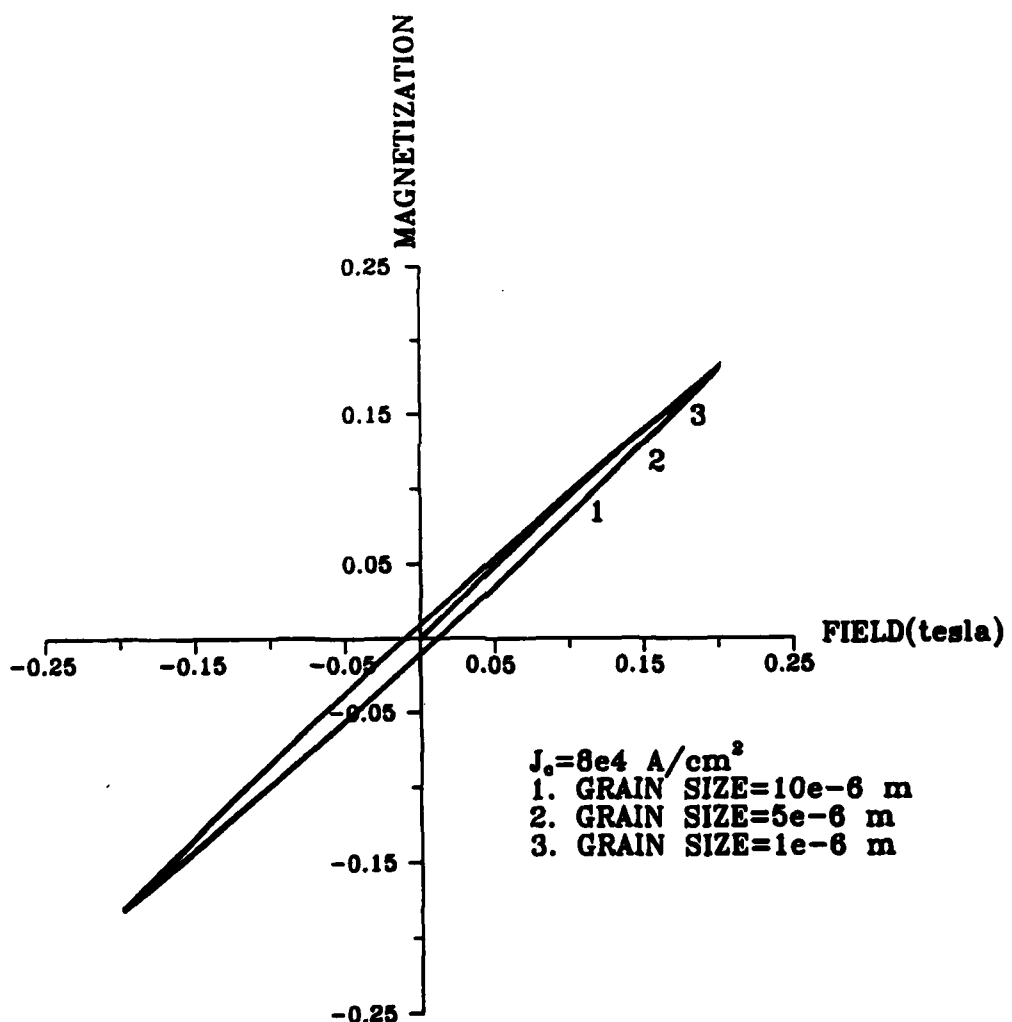
FIGURE 3.4.2.13
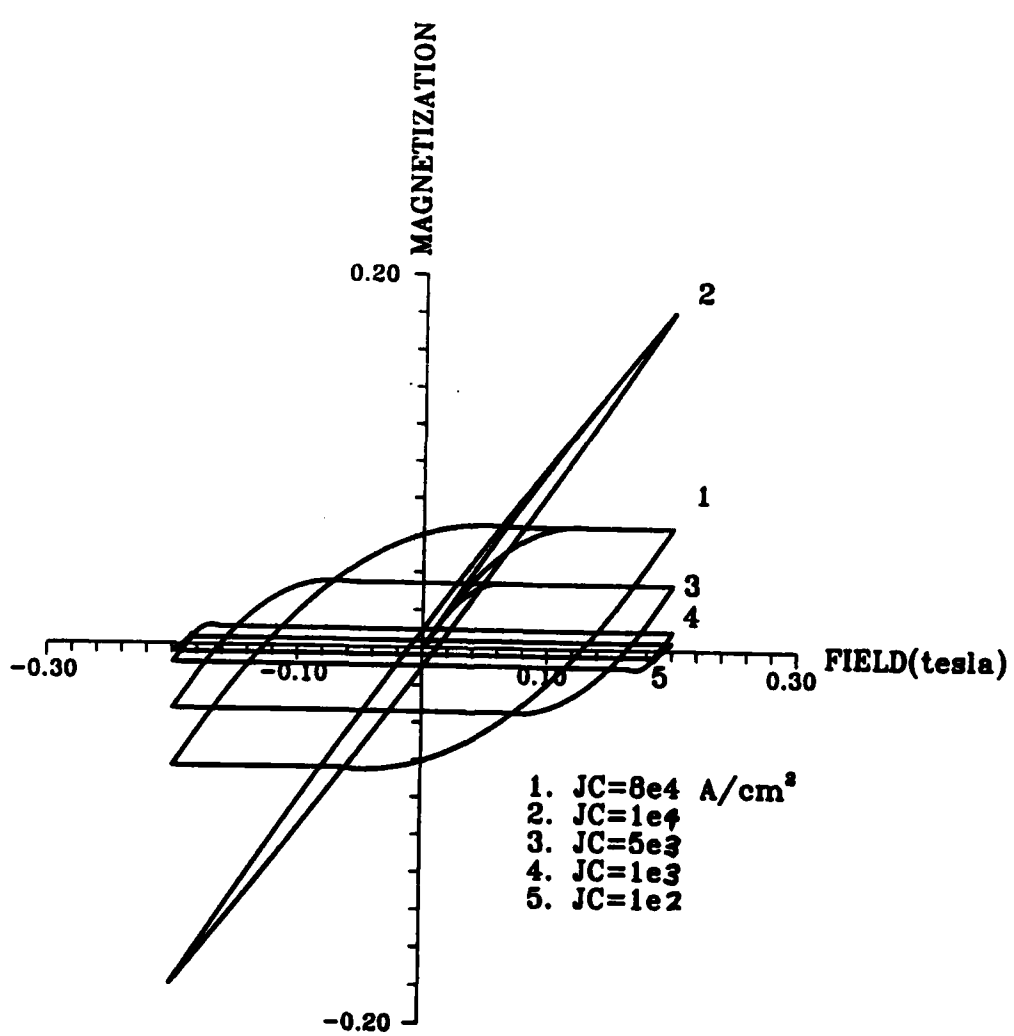
FIGURE 3.4.2.14

The above analysis will also be extended to study HTSC wires intrinsic stability.

3.5   SUMMARY

During this quarter, the major activity has been in application studies. We have been evaluating the suitability of homopolar, DC heteropolar, reluctance and induction motors for superconducting technology.

Consultants have been continuing work on the properties of wire with emphasis on AC losses in the wire. Literature research on superconductor motors and past patent activity continued.

During the next quarter, we will complete our literature research and past patent activity study. The study of HTSC wire properties will continue and the application of superconducting wire to various motor designs will continue. The proof of principle motor design will be finalized and steps to build the motor will start. This includes the investigation of bearing systems for use in liquid nitrogen.

SECTION 4

GENERAL DISCUSSION AND SUMMARY

The wire development is entering a stage where the individual
processes are being moved from discrete operations to continuous operations.
While every process step is still under development, the options being
considered at each step are being narrowed. The present grade of jet milled
Y-123 powder has been adopted as the standard raw material. By the middle of
the next quarter, we will adopt a standard green fiber, most likely based
either on polypropylene or high density polyethylene. The fiber will be
adopted in an interim standard diameter of 100-125 microns to serve as
feedstock for downstream development, so that silver coating, cofiring,
annealing, and cladding operations can work with a consistent material.
Diameter reduction activities will continue at AIResCo, and we anticipate
changing our "standard fiber" to a finer diameter grade when it is available
in reproducible quantity. Green fiber will continue to be primarily supplied
as spools of monofilament. Next quarter, to support the ribbon wire
development, we will begin to produce experimental quantities of braided belts
of green fiber. We also expect to standardize the Ag/Pd alloy composition.
This, along with the constant 1.6 micron Y-123 powder, will permit standard
cofiring conditions to be defined. Oxygen intercalation, which we originally
intended to accomplish by a continuous anneal in-line with the sintering and
cladding, will probably be conducted as a separate step in the short term.
The amount of silver cladding will be adusted so that the separate anneal can
be conducted on spools of long lengths. Finally, we will pursue both the Ag-

clad monofil wire and the copper-clad ribbon wire, with the monofil being the first wire we expect to produce in continuous spools.

The issue of critical current density is of central importance. Although the self-field critical current density of the Y-123 filaments are steadily improving, it seems unlikely that even grain oriented Y-123 will become practical for magnet wire due to its weak link nature. Preliminary data on the variation of the weak link critical current of Y-123 filaments has raised the issue of gage length effects which would greatly reduce the current density of continuous lengths of wire. Through collaborative research with Sandia National Laboratories, we will explore novel heat treatments for Y-123 aimed at achieving microstructures similar to "melt textured growth". With Sandia we also will begin adapting the fiber process for thallium cuprate superconductors. Both of these activities are aimed at producing strong linked HTSC fibers. This work will be included in future quarterly reports.

The HTSC demonstration motor activity at Emerson Electric is proceeding on schedule. A choice for the proof-of-principle machine will be made early in the next quarter, based upon the characteristics of the machine itself, and upon the suitability of near term HTSC wire properties. A variety of machines have been considered based on long-term wire property goals. A DC homopolar motor was identified as the best approach where low voltage and high current are available. The current and voltage characteristics were calculated as a fuction of rotor radius for a four disc version producing 10 horsepower, assuming a 3 tesla field produced with an HTSC winding carrying $10^5 A/cm^2$. Heteropolar DC machines were also considered, with field coil design and analysis one for a 1800 RPM DC brush motor with a superconducting field. An iron-free version of this size motor would only be practical if

current densities greater than 10^6 A/cm^2 were available. A reluctance motor with an SC flux block rotor was considered, but did not prove advantageous. An induction motor with superconducting stator windings appears to be an attractive option, especially since cryogenic versions of this motor are available. The induction motor will be studied in more detail. At this time it appears that either the homopolar or the induction motor will be chosen as the proof of principle motor.

AC losses are a critical issue for HTSC motor design, since the ability of the system to tolerate time varying magnetic fields will largely determine the type of machine which will be practical. Hilal at the University of Wisconsin has begun to define the AC loss issues for HTSC materials for both eddy current and hysteresis loss. Eddy current losses in twisted filamentary composites of HTSC are treated first by defining the critical twist pitch for the case of textured HTSC wire with anisotropic critical current density. Critical twist pitch was predicted for longitudinal and transverse cases, in terms of the values of the critical current densities, matrix resistivity, and time derivative of magnetic flux. Hysteresis losses in HTSC wire were studied using a new model for magnetization involving both the transport critical current density and the magnetization critical current density. Magnetization loops were calculated for a variety of conditions, with transport critical currents between 100 and 80,000 A/cm^2. The grain size and wire diameter play an important role in the hysteresis loss. These considerations will be used to guide our design of the HTSC wire, such as the transposition patterns in braided belts of fiber, and the resistivity of the cladding alloy.